ABRUPT SEASONAL SHIFTS IN ITCZ RAINFALL OVER EASTERN AFRICA: REGIONAL MODEL SIMULATIONS, STATISTICAL INDEX DEVELOPMENT AND CONNECTIONS WITH SOMALI JET DYNAMICS

A Dissertation

Presented to the Faculty of the Graduate School

of Cornell University

In Partial Fulfillment of the Requirements for the Degree of

Doctor of Philosophy

by

Emily Elizabeth Riddle

January 2011

ABRUPT SEASONAL SHIFTS IN ITCZ RAINFALL OVER EASTERN AFRICA: REGIONAL MODEL SIMULATIONS, STATISTICAL INDEX DEVELOPMENT AND CONNECTIONS WITH SOMALI JET DYNAMICS

EMILY ELIZABETH RIDDLE, Ph. D.

Cornell University 2011

Rainfall over eastern Africa, as in most of the tropics, moves north in the boreal summer and south in the austral summer, following the progression of the sun. Between late January and late July, the latitude of rainfall moves from southern Africa northward into the Ethiopian highlands, covering approximately 30 degrees of latitude. Variability in this progression affects the timing of rainfall for drought-prone countries along the eastern coast of Africa, from Tanzania to Ethiopia. The work in this dissertation furthers current scientific understanding of seasonal and intraseasonal rainfall variability in these regions. The three substantive chapters of this dissertation (Chapters 2-4) are each intended to stand alone as a publishable paper. The first paper (Chapter 2) documents, for the first time, the presence of abrupt shifts ("jumps") in the latitude of rainfall over eastern Africa during April and May. Regional climate model simulations demonstrate that these rainfall "jumps" are coincident with transitions between stages in the development of the Somali Jet. The second paper (Chapter 3) applies multivariate statistical methods to reduce the complex rainfall cycle into simple time-varying indices. The indices are used to characterize the timing of rainfall jumps, and solidify the association, at the daily timescale, between the seasonal rainfall progression and the Somali Jet development. The third paper (Chapter 4) focuses specifically on an intermediate stage in the Somali Jet development, which I

call the “nascent” Somali Jet, found to associated with southern Ethiopian rainfall in April and May. The work fills a gap in the literature, which has previously focused primarily on the fully-formed jet. The analysis finds that the timing of the nascent jet formation may be linked to the passage of southern hemisphere weather systems. Results from all three papers are summarized in Chapter 5, and directions for future research are proposed.

BIOGRAPHICAL SKETCH

Emily Elizabeth Riddle was born January 26, 1977 in Springfield, Massachusetts. She grew up in Amherst, Massachusetts and graduated from Amherst Regional High School in 1995. After a year as an exchange student in Kiihtelysvaara, Finland, she attended Carleton College in Northfield, Minnesota where she graduated with a B. A. in physics in 2000. She became interested in atmospheric science during two summers at an REU program at Langmuir Lab for Atmospheric Research on top of Mount Baldy in central New Mexico. During these summers she was involved in lightning triggering experiments, launching rockets into electrified clouds. She returned to New Mexico to work at Los Alamos National Lab after graduating from Carleton.

Emily attended the University of Massachusetts between 2002 and 2005, during which time she helped her Masters advisor, Dr. Paul Voss, develop a novel altitude control system for balloons which track pollution plumes. She received her M. S. in Geosciences from UMass in September, 2005. Upon completing her Ph. D. from Cornell, Emily will be working at NOAA's Center for Climate Prediction in Camp Springs, Maryland. Emily is happiest when tromping around outdoors with her soon-to-be husband, Andrew. She loves backpacking, canoeing, kayaking, biking, running, swimming, climbing trees and scampering around on rocks.

ACKNOWLEDGMENTS

I would like to thank the many, many people who have helped me throughout my years at Cornell. As with any Ph. D., this accomplishment could not have been achieved without the advice and support of a large group of mentors, teachers, family and friends. While I do not have the space to thank everyone here, I would like to specifically acknowledge those who have contributed particularly generously of their time and support.

To begin, I would like to thank my current graduate advisor Dr. Daniel Wilks. Dan possesses many skills that make him an outstanding advisor. He has nurtured my scientific independence, while providing excellent and efficient feedback whenever it is needed. His knowledge of statistics is mind-boggling, and he has repeatedly demonstrated the remarkable ability to make sense of and correctly articulate my rather incoherent ramblings about a thought or idea. I am indebted to his patience, intelligence and willingness to take me on as a student in the middle of my graduate studies.

I would also like to thank Dr. Kerry Cook for her considerable time and energy advising me during the first years of my graduate work. The subject area for the body of work presented in this dissertation was developed based on Dr. Cook's National Science Foundation grant # ATM-0415481. Before moving to the University of Texas, Prof. Cook supported me through my introduction to the field of climate dynamics and modeling, provided funding and computing resources, and worked with me on two journal articles. I would also like to extend my gratitude to Dr. Edward Vizy who gave many hours of his time teaching me to run WRF and MM5.

I have been blessed with a wonderfully helpful and supportive dissertation committee. I would like to thank my committee members Dr. Todd Walter, Dr.

Zellman Warhaft, Dr. Natalie Mahowald, as well as my former committee member, Dr. Steve Colucci. All have provided invaluable feedback on my papers, as well as mentorship and advice. I would particularly like to thank Natalie Mahowald for her excellent comments on my final two papers, and for her tremendous efficiency and enthusiasm in general. As I move on in my life and career, she will continue to be role model of a highly successful Scientist-Mom extraordinaire.

I thank all of my teachers and professors who have taught me so well over the years. There are too many to acknowledge here, but I would like mention a few in particular. Charlie Camp, my physics teacher at Amherst High School sparked my interest in physics and in outdoor adventures. The Carleton College physics department, particularly Bill Titus, Cindy Blaha, Rich Noer, Kevin Pettit and Joel Weisberg, gave me my solid physics background in an amazingly nurturing environment. Finally, my M. S. advisor at UMass, Paul Voss, has been one of my strongest advocates and mentors. Of the many things that Paul has taught me, I probably most value his help improving my scientific writing, as painful as his comments sometimes were. His high standards for clarity and style were instrumental in transitioning my writing from the classroom to the professional sphere.

I would like to thank the NASA Earth Systems Science Fellowship program, the American Association for University Women, the National Science Foundation, and the Cornell Graduate School for providing the funding to support my graduate studies. I have appreciated the personal support of Janet Crampton, who contributed towards my AAUW fellowship and who I have gotten to know while living in Maryland.

Finally, I would like to thank all of my friends and family who have supported me through the past five years. Thank you to Anita, Lola and Sue, among others, for keeping my weekly goals smart, specific and achievable! Thanks to the current and

former members of the Cook research group, particularly Dr. Samson Hagos, Dr. Christina Patricola, and soon-to-be Dr. Bing Pu whose friendship, support and research advice, have always been greatly treasured.

Thank you to my wonderful parents, Chris and DeAnne, my brother Matt, and my mother-in-law Mady who have always been there to pull me through my low points and cheer on my high ones. And of course, thank you most deeply to Andrew for being by my side through all of those ups and downs. As much as I am proud of my own achievement, this degree feels like an accomplishment that we share. I cannot wait to celebrate with you as this segment draws to a close, and we start a new adventure in September.

TABLE OF CONTENTS

LIST OF FIGURES

LIST OF TABLES

CHAPTER 1

INTRODUCTION

1.1 Preface

Since early civilizations, humans have had a vital interest in understanding and predicting weather and climate patterns, making atmospheric science one of the oldest fields of scientific inquiry. Today, understanding the atmosphere and its changing patterns remains of fundamental importance to people's lives. At short time scales, we commonly use weather predictions to inform our daily planning and decision making. At intermediate time scales, seasonal forecasts aid in agricultural planning and disaster preparation. At much long timescales, many hope that scientific predictions of anthropogenic climate change will help world leaders make environmental policy decisions that will protect future generations.

While the lives of people in the developed world are impacted by weather and climate patterns, the developing world is even more vulnerable to atmospheric variations. Many developing countries depend heavily on local rain-fed agriculture to support their populations, and have fewer resources to adapt when unexpected weather and climate anomalies occur. At the same time, funding for atmospheric research tends to focus mostly on developed countries, resulting in a relative lag in our understanding of atmospheric processes over parts of the developing world.

This dissertation focuses on seasonal rainfall patterns over eastern Africa, a primarily agricultural region, with yearly crop yields strongly tied to quantity and timing of rainfall. For the purposes of this study, eastern Africa includes both "East Africa" (Kenya, Tanzania and Uganda) and the "Horn of Africa" (Somalia, Djibouti, Eritrea, and Ethiopia).

Climatologically, eastern Africa is a very interesting and complex region, with desert, shrub-land, and dense forests all coexisting within relatively short distances. The seasonality of rainfall also changes over distances on the order of ten kilometers [*Nicholson*, 1996]. Local climates and atmospheric circulation patterns are affected by an array of factors including local surface features (high mountains, rift valleys, low-lands and lakes) as well as the regional setting near the Indian Ocean, and at the western boundary of the region affected by Indian monsoon flow reversals.

1.2 Eastern African Rainfall Trends and Vulnerabilities

Studies suggest that eastern Africa has experienced a steady drying trend throughout the 20th and 21st centuries. Records of lake levels [*Nicholson and Yin*, 2001] and glaciers [*Mölg et al.,* 2009] imply that the climate over eastern Africa was significantly wetter at the turn of the 19th century compared with today. Since 1980, *Funk et al.* [2008] have discerned in a 15% decrease in rainfall at rain gauge stations over eastern and southern Africa. This decrease in rainfall, along with a rapidly increasing population, has lead to a doubling in the number of undernourished people in eastern and southern Africa since 1980 [*Funk et al.,* 2008].

Studies disagree about whether this drying trend will continue. Global Climate Model (GCM) simulations performed for the IPCC's fourth assessment report (the IPCC AR4 models) link anthropogenic warming in the western Indian Ocean and weakening of zonal circulation in the tropics to a wetter climate over eastern Africa [e.g., *Vecchi and Soden*, 2007; *Christensen*, 2007]. In contrast, *Funk et al.* [2008] argue that these local results are not robust in the low-resolution GCMs, nor are they consistent with the statistical relationships observed in the current climate system. They instead suggest that rainfall over eastern Africa will continue to decrease as the southwestern Indian Ocean warms, preferentially shifting rainfall over the ocean rather

than over the continent, a robust large-scale feature of the GCM simulations. They warn that continued drying of eastern and southern Africa could lead to a 50% increase in the number of undernourished people in the region by 2030 if steps are not taken.

These uncertainties and vulnerabilities stress the need for a better understanding of the eastern African climate system. The work in this dissertation focuses on one important aspect of that system: variability in the seasonal rainfall cycle. The goal of this work is ultimately to lay groundwork which could help improve rainfall forecasts at timescales of several days to several months. While not addressing long-term climate change directly, improved rainfall forecasts at these shorter timescales could be one way to help mitigate the negative effects of changing rainfall conditions to allow for better agricultural planning and crisis preparation.

1.3 Seasonal Cycles: the ITCZ and the monsoons

While most seasonal rainfall forecasts focus on rainfall totals, farmers and pastoralists are also very interested in the timing at which the rainfall occurs. For example, pastoralists in northern Kenya and southern Ethiopia have identified the spring onset date as the single most desirable piece of forecast information [*Luseno et al.,* 2003]. Rainy season onset and withdrawal dates across eastern Africa are tied to the seasonal progression of rainfall. Therefore, we devote this section to providing some background on the factors controlling seasonal rainfall cycles in the tropics in general, and over eastern Africa, in particular.

Over much of the tropics, the seasonal rainfall cycle is ultimately controlled by the north-south movement of the sun. In the global average, a relatively simple connection exists between tropical rainfall and the solar insolation cycle. As the sun moves north between the boreal winter and summer solstices, it heats up the surface of

the earth at progressively more northern latitudes. This input of energy at the surface is generally associated with large-scale rising motion in the atmosphere and low-level atmospheric convergence. This region of convergence and uplift, referred to as the Inter-tropical Convergence Zone (ITCZ), is the rising branch of the well known Hadley cell of the atmosphere's general circulation. In general, the ITCZ is also associated with a band of precipitating convective storms which move north and south with the seasons.

Solar heating at the surface also drives tropical monsoon circulations, another important source of seasonal rainfall variability in the tropics. Monsoon circulations result from contrasts in solar heating between ocean and land surfaces. With a higher heat capacity, the ocean warms and cools very slowly in response to changes in solar insolation, while land surfaces respond more quickly. Therefore, land surfaces tend to be warmer than the ocean in the summer months and cooler in the winter. This contrast can leads to a strong onshore flow and heavy precipitation during the summer, and offshore flow and dry conditions during the winter. Monsoon regions with reversing onshore/offshore winds and heavy summer rainfall include the South Asia (India), East Asia, Australia, West Africa and to a lesser degree North and South America [*Webster et al.*, 1998].

Over eastern Africa, the seasonal cycle of eastern African precipitation is primarily controlled by the north/south migration of the ITCZ, modulated by local variations at the surface (e.g., topography, lakes, vegetation) and by interactions with the Indian and West African monsoons to the east and west.

To the east, the reversal of the Indian monsoon flow dominates seasonal changes in circulation over the Indian Ocean and along the coast of eastern Africa. During the boreal summer, inflow towards the Indian monsoon crosses the equator from the southern into northern hemisphere. This low-level airstream curves in a

clockwise arc due to the effect of the earth's rotation, and is forced by the east African topography into a strong low-level jet, the Somali Jet, along the eastern coast of Africa. A portion of this jet, the Turkana Jet, makes its way into the African continental interior through a gap in the mountains between Ethiopia and Kenya, while the remainder crosses the Arabian Sea and provides moisture for the Indian monsoon rains. During the boreal winter, the flow reverses, though the northerly monsoon flow in the winter is broader and weaker, with no strong jet present.

To the west, the westerly Congo airstream generally brings moist air eastward across the African continent. When this airstreams penetrates far enough to the east, it has been connected with increases in rainfall over eastern Africa.

1.4 Methodology Overview

This dissertation examines the seasonal cycle of eastern African rainfall from multiple perspectives. Precipitation datasets are used throughout this work to characterize rainfall variability. Because surface rainfall records over Africa are relatively sparse, rainfall data are mostly taken from satellite measurements. Satellite sensors can estimate rainfall in a variety of ways. Infrared sensors measure the temperature of cloud tops, which directly corresponds to the cloud heights. Particularly in the tropics, cumulus cloud heights are likewise correlated to the intensity of rainfall. Infrared sensors have excellent spatial and temporal coverage, but give only approximate estimates of rainfall.

Significantly more accurate rainfall estimates can be determined from passive microwave sensors and from the Tropical Rainfall Measuring Mission (TRMM) Precipitation Radar (PR). Microwave sensors detect microwave radiation emitted directly from raindrops and can detect raindrops throughout the depth of a cloud. The TRMM Precipitation Radar works similarly to ground based radar, sending a beam of

radio waves towards the cloud and detecting the backscatter. Because of the TRMM PR location orbiting at 250 miles above the surface, it requires higher power and operates at a higher frequency than ground-based radar [*Huffman et al*, 2007]. The accuracy of the passive microwave and TRMM PR are much better than the infrared sensors, however the coverage of these instruments is sparser. The rainfall datasets used in this dissertation incorporate various combinations of these satellite measurement techniques as well as ground-based rain gauge rainfall estimates.

To examine wind and pressure fields, global atmospheric "reanalyses" are used. The reanalyses, provided by the United States and European meteorological agencies, are best-guess reconstructions of past atmospheric conditions. They optimally combine atmospheric observations (from balloons, surface measurements, and satellites) with our knowledge of the physical equations governing the state of the atmosphere. Variables needed to reconstruct full momentum, energy, moisture, and mass budgets are provided on latitude/longitude and vertical grids every three hours over the last several decades.

Because the reanalyses are run at relatively low resolution (~1.25 degrees), regional climate models are used in this work to dynamically "downscale" the reanalysis data to a finer grid (30 km). The regional models numerically integrate conservation equations for mass, momentum, energy and moisture, using parameterizations to represent processes that occur on scales that are not resolved by the 30 km model resolution. Parameterizations are needed to represent radiative heat transfer, cloud and ice droplet formation, precipitation, turbulence, convection, land surface processes, and near surface fluxes of energy, momentum and moisture. Conditions at the lateral model boundaries are taken from the reanalyses, while surface topography, vegetation and sea surface temperatures are taken from other high resolution datasets. The resulting regional model simulations provide a consistent

picture of the atmospheric evolution which incorporate higher resolution surface features than are available in the reanalyses.

All of these atmospheric descriptions (model, reanalysis and observations) involve very large datasets that describe the full complexity of how the atmosphere evolves in space and time. The sheer quantity of information encoded in these datasets and model simulations can make it difficult to pinpoint important patterns and dependencies. Therefore, in chapter 3 we use two multivariate statistical methods (a principal component analysis, and a cluster analysis) to calculate manageable indices from the full rainfall datasets. The indices encode the most important aspects of the seasonal rainfall cycle are used to characterize interannual variability in the rainfall cycle, and to examine correlations with reanalysis circulation fields.

1.5 The Dissertation Chapters

The three substantive chapters in this dissertation are Chapters 2, 3 and 4, each of which is intended to stand alone as a publishable paper with new scientific contributions. In Chapter 2, we identify, for the first time, abrupt northward shifts ("jumps") in the latitude of rainfall that occur over eastern Africa during April and May. We propose a hypothesis connecting these abrupt shifts to the development of the Somali Jet. In Chapter 3, we develop two new statistical indices to describe the seasonal cycle of eastern African rainfall. The indices are used to characterize variability in the latitude "jumps" identified in Chapter 2, and to provide stronger link between the timing of the rainfall progression and the Somali Jet formation. In Chapter 4, we focus more closely on the Somali Jet development, describing for the first time in detail the characteristics of a "nascent" Somali Jet which is present along the East African coast in April and May. The final chapter, Chapter 5, provides a summary of the dissertation results and proposes directions for future work.

REFERENCES

Christensen, J. H., Hewitson, B., Busuioc, A., Chen, A., Gao, X., Held, R., Jones, R., Kolli, R. K., Kwon, W. K., Laprise, R., Magana Rueda, V., Mearns, L., Menendez, C. G., Räisänen, J., Rinke, A., Sarr, A., Whetton, P., Arritt, R., Benestad, R., Beniston, M., Bromwich, D., Caya, D., Comiso, J., de Elia, R., Dethloff, K. et al.(2007). Regional climate projections, Climate Change, 2007: The Physical Science Basis. Contribution of Working group I to the Fourth Assessment Report of the Intergovernmental Panel on Climate Change, University Press, Cambridge, Chapter 11,, 847-940.

Funk, C. F., M. D., Dettinger, J. C. Michaelsen, J. P. Verdin, M. E. Brown, M. Barlow, and A. Hoell (2008), Warming of the Indian Ocean threatens eastern and southern African food security but could be mitigated by agricultural development. *Proc. Natl. Acad. Sci.*, 105, 11081-11086.

Huffman, G. J., R. F. Adler, D. T. Bolvin, G. Gu, E. J. Nelkin, K. P. Bowman, Y. Hong, E. F. Stocker, and D. B. Wolff (2007), The TRMM multi-satellite precipitation analysis (TMPA): Quasi-global, multiyear, combined-sensor precipitation estimates at fine scales, J. Hydrometeorol., 8(1), 38– 55.

Luseno, W. K., J. G. McPeak, C. B. Barrett, P. D. Little, and G. Gebru (2003), Assessing the value of climate forecast information for pastoralists: Evidence from southern Ethiopia and northern Kenya, *World Development, 31,* 1477-1494.

Mölg, T., N. J. Cullen, D. R. Hardy, M. Winkler, and G. Kaser (2009), Quantifying Climate Change in the Tropical Midtroposphere over East Africa from glacier shrinkage o Kilimanjaro, *J. Clim*., 22, 4162-4181.

Nicholson, S. E. 1996. A review of climate dynamics and climate variability in Eastern Africa. *The Limnology, Climatology and Paleoclimatology of the East African Lakes,* T. C. Johnson and E. O. Odada, Eds., Gordon and Breach, 25–56.

Nicholson, S. E., and X. Yin (2001), Rainfall conditions in equatorial East Africa during the nineteenth century as inferred from the record of Lake Victoria. Climatic Change, 48, 387–398.

Vecchi, G. A., and B. J. Soden (2007), Global warming and the weakening of the tropical circulation, *J. Clim*., 20, 4316-4340.

Webster, P. J., V. O. Magaña, T. N. Palmer, J. Shukla, R. A. Tomas, M. Yanai, and T. Yasunari (1998), Monsoons: Processes, predictability, and the prospects for prediction, *J. Geophys. Res.*, 103(C7), 14,451–14,510, doi:10.1029/97JC02719.

CHAPTER 2

ABRUPT RAINFALL TRANSITIONS OVER THE GREATER HORN OF AFRICA: OBSERVATIONS AND REGIONAL MODEL SIMULATIONS

2.1 Introduction

The seasonal cycle of rainfall in the tropics is ultimately driven by seasonal changes in solar radiation. While the solar cycle varies smoothly with latitude, rainfall cycles can often respond with sudden jumps, particularly over the continents where varying surface properties (e.g., topography, soil moisture, land/sea contrasts) can create important circulations and non-linear feedbacks in the climate system. Abrupt jumps in the latitude of rainfall occur annually during the onset of the West African and East Asian monsoons [*Sultan and Janicot*, 2000; *Hagos and Cook,* 2007; *Xue et al.*, 2004]. Here we show that similar sudden transitions occur during the evolution of the East African monsoon.

Understanding abrupt transitions in rainfall is crucial to generating useful seasonal and sub-seasonal forecasts. While most prediction studies focus on the total seasonal rainfall amount [e.g., *Thiaw et al*., 1999], the timing of that rainfall is equally important to agriculture and water resource management. For example, pastoralists in northern Kenya and southern Ethiopia have identified the spring onset date as the single most desirable piece of forecast information [*Luseno et al*., 2003]. The timing of the seasonal transitions can also be an important control on drought, since a late onset or early termination can initiate or exacerbate drought conditions [e.g., *Segele and Lamb*, 2005]. As an example, anomalously short spring rainy seasons in recent years (2000-2004) have led to recent food shortages in southern Ethiopia [*Verdin et al.*, 2005].

The purpose of this study is to understand abrupt seasonal and sub-seasonal transitions that occur during the spring and summer over the Greater Horn of Africa (GHA), focusing particularly on the onset of the rainy seasons over Ethiopia, Eritrea and Djibouti. Observations and regional climate model simulations are used to investigate the timing of the jumps and examine the associated atmospheric circulation patterns.

2.2 Background

Rainfall over the Greater Horn of Africa (GHA) demonstrates strong seasonality. In the southern GHA (e.g., Kenya, Uganda, Northern Tanzania, Somalia) the rainy seasons come during the boreal spring (MAM) and fall (ON). These seasons are referred to as the "long" and "short" rains, respectively. Further north, in Ethiopia, Djibouti and Eritrea, the primary rainy seasons are in the spring (*belg*) and summer (*kiremt*) with a dry period (*bega*) in the winter [e.g., *Beltrando and Camberlin*, 1993].

Atmospheric circulation patterns also demonstrate a strong seasonal cycle over the GHA, guided by changes in insolation and SSTs. A prominent feature is the development of the low-level Somali jet [e.g., *Findlater,* 1969] in the boreal summer. The East African topography plays a crucial role in confining this jet to the coast of Somalia [*Slingo et al.,* 2005; *Rodwell and Hoskins*, 1995]. This flow pattern is reversed during the winter monsoon season.

Much of literature concerning rainfall over the GHA has focused on establishing predictive relationships between seasonal rainfall totals and remote indicators. In the northern GHA (Ethiopia, Djibouti and Eritrea), the majority of these studies examine the predictability of summer (JJAS) rainfall. Rainfall in this region is negatively correlated with El Niño [e.g., *Beltrando and Camberlin*, 1993; *Camberlin*, 1995; *Gissila et al.,* 2004; *Segele and Lamb,* 2005; *Korecha and Barnston,* 2007]

which is also generally associated with basin-wide heating of the Indian Ocean. Studies disagree on the importance of independent modes of SST variability in the Indian Ocean, such as the dipole mode [*Gissila et al*., 2004; *Korecha and Barnston*, 2007]. *Beltrando and Camberlin* [1993] find that influence of the Pacific and the Indian Oceans is strongest during June and September, while, in July and August, rainfall intensity is additionally influenced by local convection and the West African monsoon [*Flohn*, 1987].

Other studies find very strong correlations between Ethiopian summer rainfall and the strength of the Indian monsoon, independent of a mutual dependence on ENSO [e.g., *Bhatt*, 1989; *Camberlin*, 1997]. *Vizy and Cook* [2003] discuss the mechanisms of this connection using regional climate model simulations.

In contrast to the Ethiopian summer rains, the short rains during October and November over the southern GHA (Kenya, Uganda, Tanzania) are positively correlated with El Niño events [e.g., *Ogallo*, 1988; *Hastenrath et al.*, 1993; *Indeje et al*., 2000; *Mutai and Ward*, 2000], and also with the Indian Ocean dipole mode [e.g., *Behera et al.*, 2005; *Clark et al*., 2003; *Bowden and Semazzi*, 2007], showing strong dependence on Indian Ocean surface temperatures [e.g., *Goddard and Graham*, 1999; *Black*, 2005]. Severe flooding off the coast of East Africa in October and November is sometimes associated with strong dipole events [*Black et al*., 2003]. Recent modeling studies have explored some of these teleconnections [*Sun et al*., 1999; *Anyah and Semazzi*, 2006, 2007; *Conway et al*., 2007].

The spring (MAM) rainy season, which occurs in both the northern and southern GHA, is the least studied and the most complex. In general MAM rainfall does not exhibit very strong relationships with external modes of variability such as El Nino or the Indian Ocean dipole mode [e.g., *Ogallo*, 1988; *Hastenrath et al*., 1993]. This is partly because rainfall anomalies in boreal spring are less coherent spatially

and temporally than during the summer or fall. Several authors have demonstrated that early and late stages of the MAM rainy season exhibit different rainfall variability patterns [e.g., *Camberlin and Philippon*, 2002; *Zorita and Tilya*, 2002], suggesting that correlations may be more meaningful at smaller temporal or spatial scales.

Several studies have nonetheless made progress toward establishing some of the features controlling the evolution of the spring rainy season. Spring rainfall events in northern Ethiopia and Eritrea may be connected to excursions of the mid-latitude ridge-trough systems [e.g., *Camberlin and Philippon*, 2002]. Rainfall in eastern Ethiopia is negatively correlated with tropical cyclone activity in the southwestern Indian Ocean [*Shanko and Camberlin*, 1998]. Other studies have noted that strong MAM rainfall over the southern GHA is associated with a westerly anomaly in the lower to mid-tropospheric winds across equatorial Africa during March [e.g., *Camberlin and Wairoto*, 1997; *Okoola*, 1999; Camberlin *and Philippon*, 2002; *Zorita and Tilya*, 2002; *Camberlin and Okoola*, 2003].

Camberlin and Okoola [2003] examined the timing of the onset and cessation of the long rains over the southern GHA (Kenya, Uganda and Northern Tanzania). They found the onset date to vary by almost two months, and be an important determinant of the cumulative rainfall for the season. In a more recent study, *Pohl and Camberlin* [2006a, 2006b], suggest that the MJO is an important source of intraseasonal variability modulating the MAM rainfall over the southern GHA.

2.3 Methods

A combination of observed, analyzed and model data is used to characterize the seasonal precipitation cycle over the GHA and examine the associated atmospheric dynamics. Precipitation datasets serve to establish a climatology of the seasonal precipitation cycle over the GHA, and to validate the model-generated precipitation

rates. Reanalyzed data are used for validation of the three-dimensional model fields. Regional climate model simulations provide a high resolution, self-consistent representation of the regional momentum, energy and moisture budgets. The regional climate model, run at 30 km resolution, is better able to capture the complex topography and land surface features over East Africa than existing three-dimensional datasets (e.g., the NCEP reanalysis). The primary results of this study are duplicated in the observations, the reanalysis, and model and thus do not depend solely on the accuracy of any one approach.

2.3.1 Observations and Reanalysis

Three observational precipitation datasets are used, based on varying combinations of satellite-derived precipitation and rain gauge measurements. The Climate Research Unit (CRU CL 2.0) precipitation climatology [*New et al*., 2002] is 30 years long (1961-1990) and is derived exclusively from an extensive network of rain gauge measurements. The data are gridded at 10-minute (0.17° x 0.17°) resolution, though the actual resolution of the underlying data over the GHA is considerably lower. These data provide a long term precipitation record, but do not extend over the oceans and are available only on a monthly timescale.

In contrast, the Tropical Rainfall Measure Mission (TRMM) 3B42 V6 product is derived using a combination of satellites (TRMM and other), calibrated using monthly-averaged rain gauge data. It is available every three hours from 1998-2006 at a resolution of a 0.25° x 0.25° [*Huffman et al.*, 2007]. Another satellite-based product, the NCEP Climate Prediction Center's African Rainfall Estimate (CPC RFE2.0), is used by the Famine Early Warming System (FEWS) over Africa [*Herman et al*., 1997. This dataset (FEWS from here forward) is available daily from 2001-2006 at 0.1° x 0.1° resolution.

Both the TRMM and FEWS datasets offer high spatial and temporal resolution. However both are relatively short, being only 9 and 5 years long, respectively, so one cannot construct a true climatology. Nonetheless, we use short-term climatologies created from these datasets for comparison with the model simulation. This can be justified by looking at longer term datasets (e.g., CRU TS 2.1 [*Mitchell and Jones*, 2005]) which show that the most prominent synoptic-scale patterns in the seasonal cycle over the GHA have not changed significantly in recent decades.

The NCEP/DOE AMIP-II Reanalysis [*Kanamitsu et al*., 2002], based on the NCAR/NCEP reanalysis, is available from 1979 to present and is used to validate the model geopotential height and wind fields. It is also used to supply initial and boundary conditions to the model. Compared with the regional model simulations, however, the reanalysis has a much coarser resolution both in the horizontal (2.5° x 2.5°) and the vertical dimensions, and so it cannot resolve the finer-scale circulations associated with, for example, the East African topography.

2.3.2 The Regional Climate Model

The regional climate model simulations enhance existing three-dimensional datasets (e.g., NCEP-2 reanalysis) by linking the atmospheric circulation with a realistic precipitation cycle. Previous studies [e.g., *Anyah and Semazzi*, 2006] have suggested that high-resolution simulations that resolve the complex topography of East Africa are necessary in this region to accurately capture the precipitation cycle.

The regional climate model used for this study is the PSU/NCAR Mesoscale Model (MM5 [*Grell et al*., 1994]). MM5 is a limited area, non-hydrostatic model with 23 terrain-following sigma levels with a range of physical parameterization options. All simulations in this study use the Kain-Fritsch convective scheme [*Kain*, 2004], the

Rapid Radiative Transfer Model (RRTM) longwave radiation scheme [*Mlawer et al.*, 1997], the Blackadar planetary boundary layer scheme [e.g., *Blackadar*, 1979], and the Dudhia simple ice explicit moisture scheme [*Dudhia*, 1989]. These particular physics options have been found in previous studies to successfully represent the hydrological cycle over Africa [e.g., *Vizy and Cook,* 2002*,* 2003; *Patricola and Cook,* 2007].

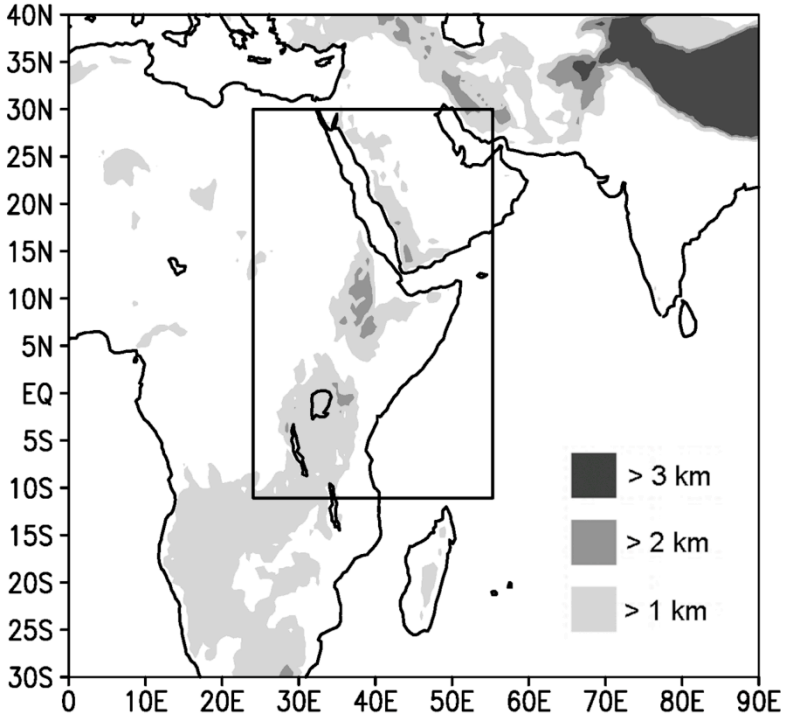

Figure 2.1: Regional map showing the model domain (box) and topography (shading) on a 30 km grid.

The domain for the simulations is chosen to include most of eastern Africa and the Arabian Peninsula (Figure 2.1). The model resolution is set to 30 kilometers to resolve the primary topographic features of the region (shaded in Figure 2.1). The domain is centered on the Ethiopian Plateau. To the south is the Turkana Channel, which separates the Ethiopian Plateau from the high topography of Kenya and Tanzania, including Mt. Kilimanjaro. This break in the topography is thought to be an

important conduit for moisture reaching the continental interior via moisture transport by the Turkana jet [*Kinuthia and Asnani*, 1982; *Indeje et al*., 2001].

Land surface conditions (e.g., soil moisture and surface albedo) for MM5 are specified using 24 categories of land surface types from the United States Geological Survey (USGS) dataset (Figure 2.2). These surface conditions are fixed throughout the integrations. Sea surface temperatures (SSTs) are based on *Shea et al.* [1992], and land surface temperatures (including lake surfaces) are initialized based on the NCEP-2 reanalysis. Initial and lateral boundary conditions are also taken from the NCEP-2 reanalysis.

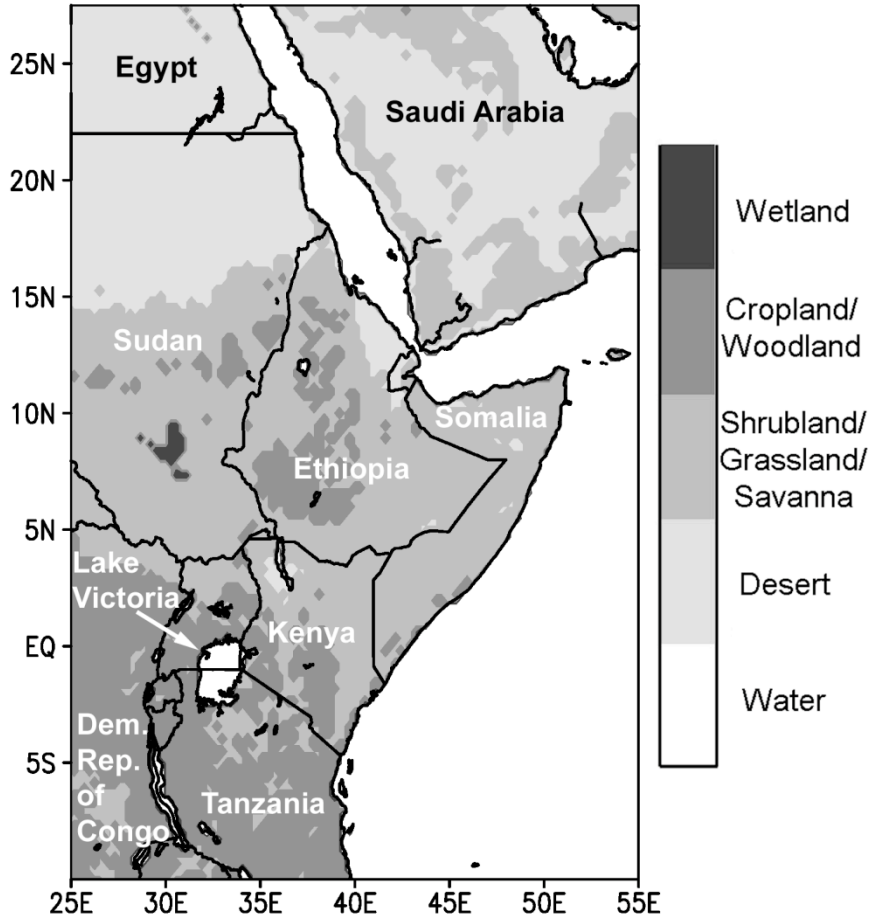

Figure 2.2: USGS land surface types used to determine surface conditions throughout the model simulations.

Three MM5 integrations are discussed. The first two are 7-month (March-September) simulations of the evolution of the rainy seasons in 2002 and 2003. The first fifteen days of the simulations are discarded as the model is spinning up. SSTs and lateral boundary conditions are updated every six hours to match the 2002 and 2003 analyzed conditions. Model output is recorded and stored every three hours.

The third integration is a 9-month (March-November) climate simulation. In this simulation, the boundary and surface conditions are taken from the monthly climatological mean values of the NCEP-2 reanalysis averaged over 1979 to 2004, interpolated linearly to 12-hour intervals. This isolates seasonal forcing of the climate within the domain by removing the effects of interannual variability and transient perturbations entering the domain. While this climate-mode simulation is theoretically different from an observational climatology, previous studies [e.g., *Vizy and Cook*, 2002] have shown that in the tropics this method can accurately reproduce observed climatological fields.

2.4 Observations and Simulations of the GHA Rainy Seasons

To be valuable for this study, the MM5 simulations must capture the primary rainfall and circulation patterns associated with the spring and summer rainy seasons of the GHA. This section will identify particular strengths and weaknesses of the model in capturing these features.

2.4.1 Rainy Season Precipitation

Figures 2.3a, b, and c display observed precipitation for the spring rainy season (MAM) from the TRMM, FEWS and CRU "climatologies" respectively (described in section 2.3.1). All three datasets have been interpolated to the same 1° x 1° grid for the comparison. Spring rainfall rates are largest over the southern half of the domain,

with local maxima over the eastern Congo, Lake Victoria, coastal Tanzania, and southwestern Ethiopia. The three datasets agree fairly well, despite being derived from different measurements (satellite vs. ground-based) and averaged over different time periods.

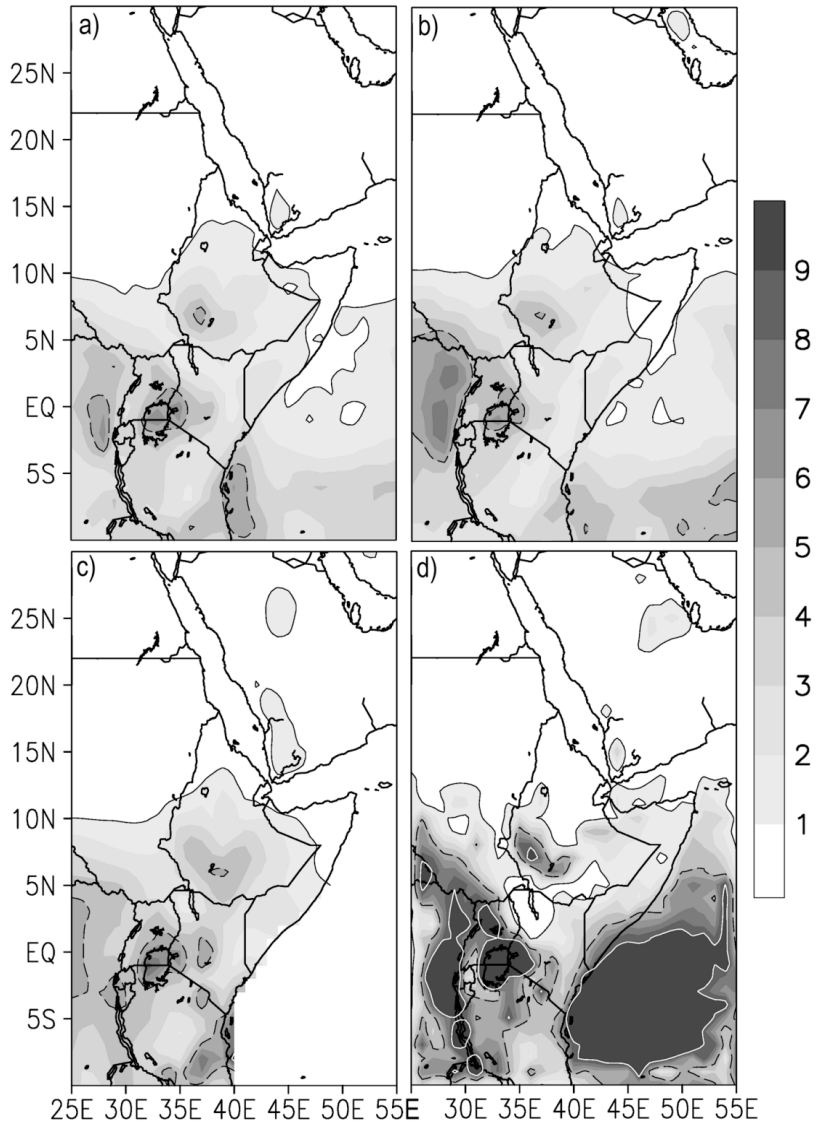

Figure 2.3: MM5 and observed precipitation (mm/day) during the spring (MAM) rainy season based on a) TRMM, b) FEWS, c) CRU datasets and d) MM5 simulated precipitation. CRU data is not available over the ocean. Selected contour lines are shown at 1 mm/day (black solid), 5 mm/day (black dashed) and 9 mm/day (white).

Springtime precipitation from the MM5 climate-mode simulation is shown in Figure 2.3d. As in the observations (Figures 2.3a-c), nearly all of the precipitation is in the lower half of the domain. While modeled precipitation rates are greater than the observed, the model captures the observed precipitation maxima over the Congo (perhaps with interference from the lateral boundaries), Lake Victoria, and southern Ethiopia following the southern topographic boundary. Excessive rainfall over Lake Victoria is often seen in regional climate simulations [e.g., *Anyah and Semazzi*, 2004, 2007] due to lake-induced local convection.

One concern in this simulation is that model precipitation over the Indian Ocean and along the coast of Tanzania is too strong. The excess precipitation over this region is caused by a series of spurious "storms" which form near the eastern domain boundary south of the equator and propagate into the domain before dissipating when hitting the coastline. These depressions extend up to 500 hPa and are most prominent in March and April during which time they deposit a large amount of rainfall over the Western Indian Ocean. We suggest that these disturbances are being created near the eastern edge of the domain due to inconsistencies at the lateral boundary. While these storms are worrisome, they do not appear to interfere with the results that will be presented in section 2.5.

Observed precipitation for the summer rainy season (JJAS) is shown in Figures 2.4a, b, and c. Again, the three observational data sets agree well, although precipitation rates in the CRU data are significantly greater than those in the satellite-based observations. The observed precipitation has shifted north of the equator, and a primary precipitation maximum is located over the western Ethiopian highlands. Additional rainfall extends to the west over southern Sudan, and the Congo basin maximum has moved about 7° farther north.

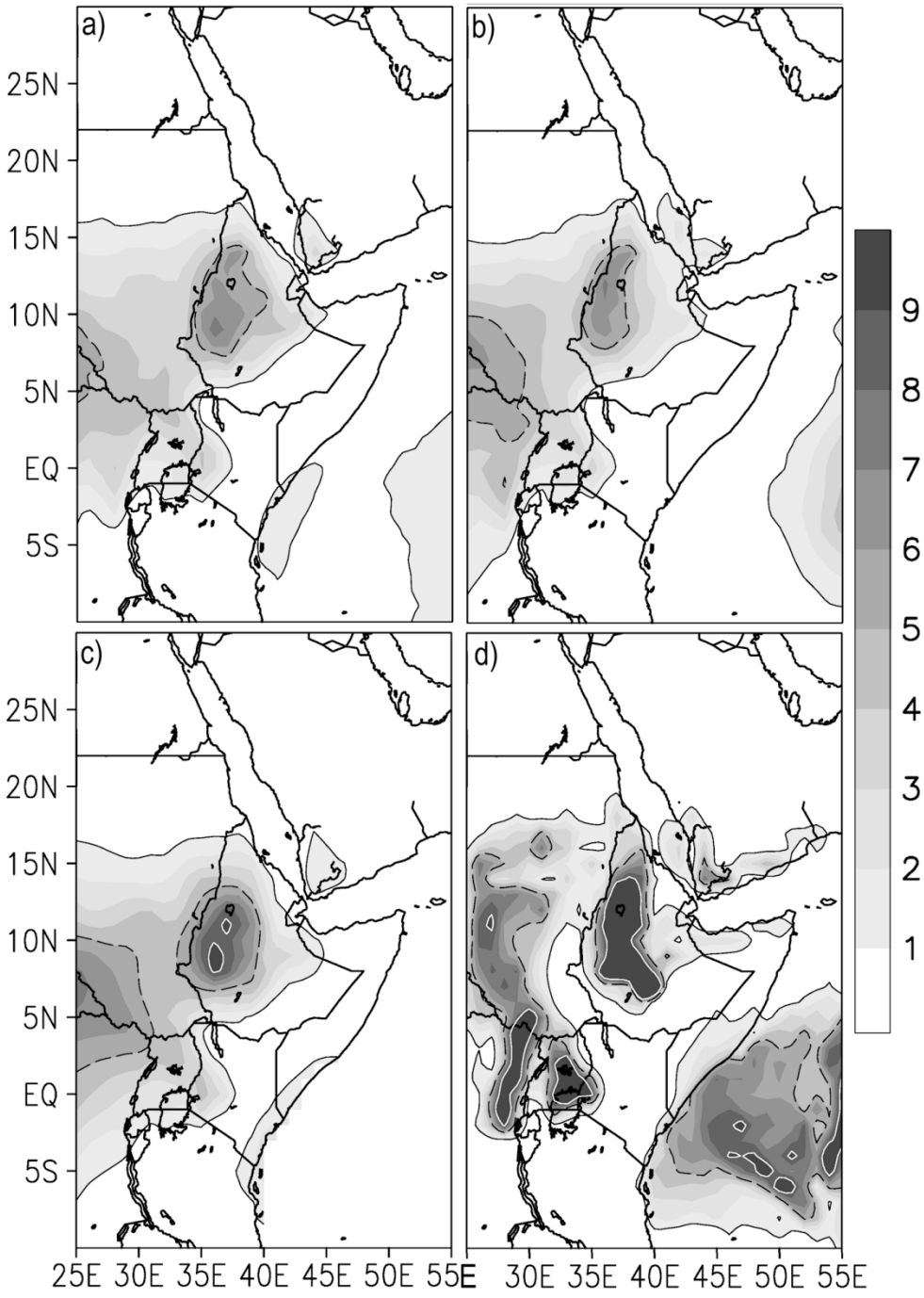

Figure 2.4: MM5 and observed precipitation (mm/day) during the summer (JJAS) rainy season based on (a) TRMM, (b) FEWS, (c) CRU datasets and (d) MM5 simulated precipitation. CRU data is not available over the ocean. Selected contour lines are shown at 1 mm/day (black solid), 5 mm/day (black dashed) and 9 mm/day (white).

The MM5 climate-mode simulation (Figure 2.4d) captures the important features of the summer season precipitation over the GHA. The large-scale shift of the rainfall to the north is well represented in the model, and the primary rainfall maximum is located over the western Ethiopian highlands. The zonal structure of the precipitation across Ethiopia and Sudan is also reasonable. However, there is too much rainfall north of Lake Victoria and in the eastern Congo basin. The anomalous rainfall over the western Indian Ocean is still present, though weaker than in the spring.

In both spring and summer the model precipitation is consistent with the observations, especially compared with the GCM simulations [e.g., *Anyah and Semazzi*, 2006] which are on coarser resolution and fail to resolve the topography accurately. Overall, the validation is stronger over Ethiopia, Eritrea and Djibouti than in the extended domain. However, at sub-degree spatial scales (not shown), the model precipitation field shows unrealistic spatial fluctuations over distances of 30-90 kilometers, which are associated with local topographic and surface variations. This suggests that at these smaller scales, the model precipitation is too sensitive to local surface features. This sensitivity carries over to the larger scales as well, producing too much rainfall over lakes (e.g., Lake Victoria) and topographic features. Despite these deficiencies, the model is able to sufficiently capture the seasonal rainfall cycle as will be further demonstrated along with the results in section 2.5.

2.4.2 Rainy Season Circulation Patterns

The mean low-level circulation patterns associated with the spring rainy season (MAM) are shown at 850 hPa for the NCEP-2 reanalysis (Figure 2.5a) and at 825 hPa for the MM5 climate mode simulation (Figure 2.5b). Similarly, circulation patterns for the summer rainy season (JJAS) are shown in Figures 2.5c and 2.5d. (The model

and reanalysis are shown at slightly different pressure levels, however these levels are near enough to exhibit very similar features.) The MM5 simulation results are interpolated to the NCEP 2.5 degree horizontal grid for these comparisons. Topography (plotted at 30 km resolution) is shaded black.

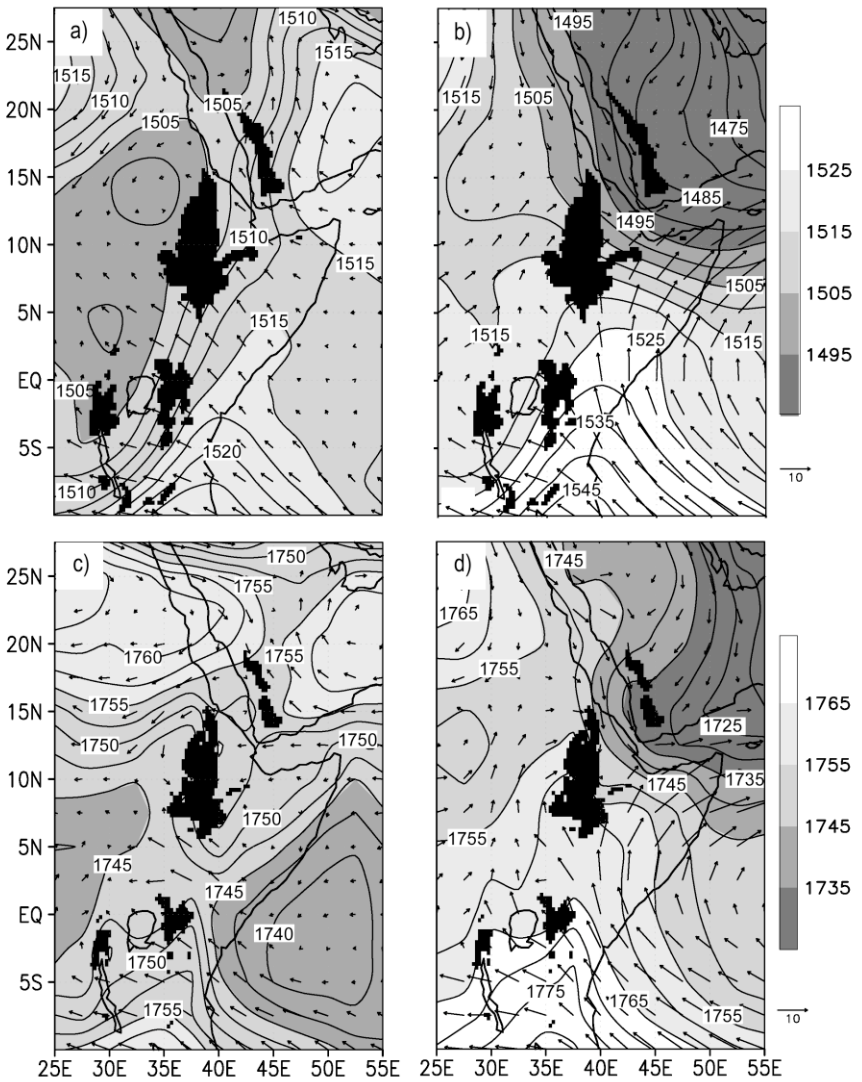

Figure 2.5: Geopotential height and wind from (a) the NCEP-2 reanalysis spring climatology (MAM), (b) the NCEP-2 reanalysis summer climatology (JJAS) (c) the springtime MM5 climate mode simulation (MAM), and (d) the summer MM5 climate mode simulation (JJAS). The NCEP-2 geopotential heights and winds (a and b) are shown at 850 mb, while MM5 heights and winds (c and d) are shown at 825 mb. The MM5 output is interpolated to the NCEP 2.5 degree grid. Black shading indicates topography extending above the plotted pressure surfaces.

For the spring season (Figures 2.5a and 2.5b), MM5 and NCEP reanalysis show similar circulation features. A region of high geopotential heights extends into the domain from the south. In the south, the flow is predominantly easterly or southeasterly, and more geostrophic in the east than in the west. Across the central part of the domain the wind tends to be easterly, including the flow impinging on the Ethiopian highlands and in the Turkana channel (i.e., the Turkana jet). In the north, the flow is essentially geostrophic and dominated by anti-cyclonic circulation around highs over the Sahara and the Arabian Peninsula. These regions are more distinct from each other in the reanalysis, inducing stronger zonal gradients than in the MM5 simulation. A closed depression over the western Indian Ocean is present only in the model output in association with the spurious storms moving over this region (described in section 2.3).

The summertime height field is dominated by a deep Indian monsoon trough extending across the Arabian Peninsula, and, weakly, into the Sudan (Figures. 2.5c and 2.5d). In addition, the high to the south is significantly stronger than in the spring. The most prominent and stable feature of the summertime circulation is the low-level Somali jet, which carries moisture across the equator and eventually feeds the Indian monsoon. Over the Ethiopian highlands, the flow is primarily westerly, in contrast to the easterly flow of the spring season (Figure 2.5a and b). Despite this change in wind direction, the Turkana jet remains southeasterly. Note the inflow of low level winds from the south (Indian Ocean), southwest (Congo basin) and north (Mediterranean) over Ethiopia.

The NCEP and MM5 circulation and geopotential height fields show remarkably good agreement in the summertime, with all of the major features reproduced by the model. Particularly in the summertime, this agreement may be

partially due to the dominance of the lateral forcing derived from the NCEP reanalysis data.

These comparisons suggest that the model is able to capture many important features associated with the spring and summer rainy seasons. The model validates particularly well over Ethiopia, a primary focus area of this study. Further validation will be provided along with results in the following sections.

2.5 Results

2.5.1 The Seasonal Rainfall Cycle

Agricultural calendars in the central GHA are closely tied to the timing of local rainfall, therefore it is useful to classify regions with respect to the similarity of their seasonal cycles. One way to do this is to classify regions by the month in which they receive their peak rainfall. This is done in Figure 2.6, in which the spring or summer month of peak precipitation is plotted for the observations and model over the focus region (Ethiopia, Eritrea and Djibouti). In the observations (Figures 2.6a-c), note the sharp divide between southeastern Ethiopia, which mostly receives maximum rainfall in April, and the northern and western parts of Ethiopia and Eritrea, which receive maximum rainfall in July and August. The MM5 simulation captures this divide as well, though the spatial transition region is somewhat less distinct. These results are contradictory to a simplified model of the ITCZ following the solar cycle; such a model would show a series of increasingly narrow horizontal latitude bands for April, May, June and July as the ITCZ migrated northward.

To investigate this further, we examine the seasonal cycle at each 1° x 1° grid point, starting with the CRU dataset. Based on the similarity of the CRU seasonal cycles, four regions are identified as shown in Figure 2.7. The resulting regional classification scheme is then applied to the remaining two observational datasets

(TRMM and FEWS) and the model output. Figure 2.8 shows each of these seasonal cycles sorted by region.

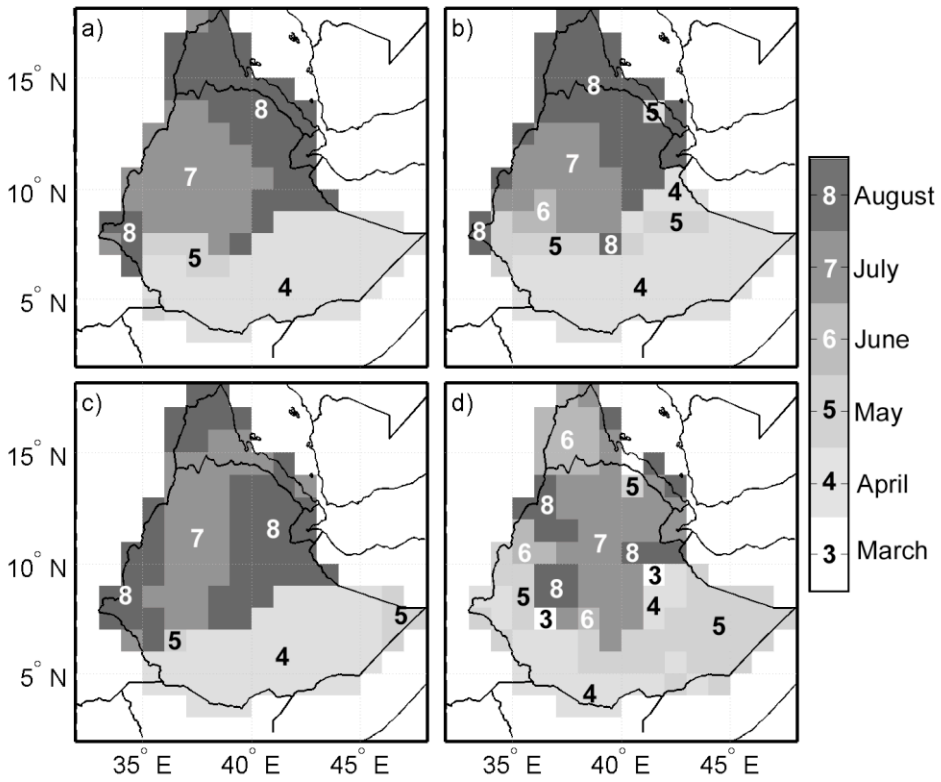

Figure 2.6: Month of peak spring rainfall during March through August over 1x1 degree pixels in Ethiopia and Eritrea as recorded by (a) TRMM, (b) FEWS, (c) CRU and (d) the MM5 climate-mode simulation.

Each region has a unique cycle of rainfall. The northwestern highlands (Figure 2.8a), which receive the heaviest overall rainfall, experience only one large peak during the months of July and August. The northeast (Figure 2.8b) experiences a peak in April, with a second peak in August, after a very dry month in June. In a small region in the southwest (Figure 2.8c), elevated precipitation levels are observed throughout the entire rainy season (March – October). Finally, the low-lying southern and eastern parts of Ethiopia (Figure 2.8d) experience two peaks in precipitation, with the larger peak in April, a second, smaller peak in October and a dry period in

between. These regions are similar to rainfall "clusters" identified over Ethiopia by *Gissila et al*. [2004].

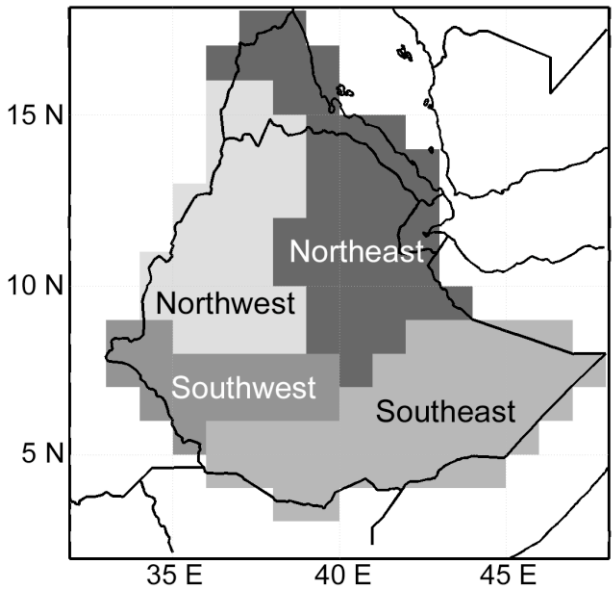

Figure 2.7: Regions with similar annual precipitation cycles according the CRU precipitation climatology.

The three observational datasets agree well not only on the mean seasonal cycle in each of these regions, but also on the degree of variability of the cycle within the regions. For the MM5 climate simulation, however, the variability is too large and the classification scheme, which is based on the CRU dataset, is not entirely appropriate. This is particularly true for the small, transitional southwestern region and the northwestern highlands where the topography is highly variable. However, the model does capture the mean seasonal cycle in each of the four regions, and reproduces the seasonal peaks correctly in the mean. This suggests that, while the model cannot capture local variability accurately, it can capture the primary features of the annual precipitation cycle at a regional scale (~1000 km).

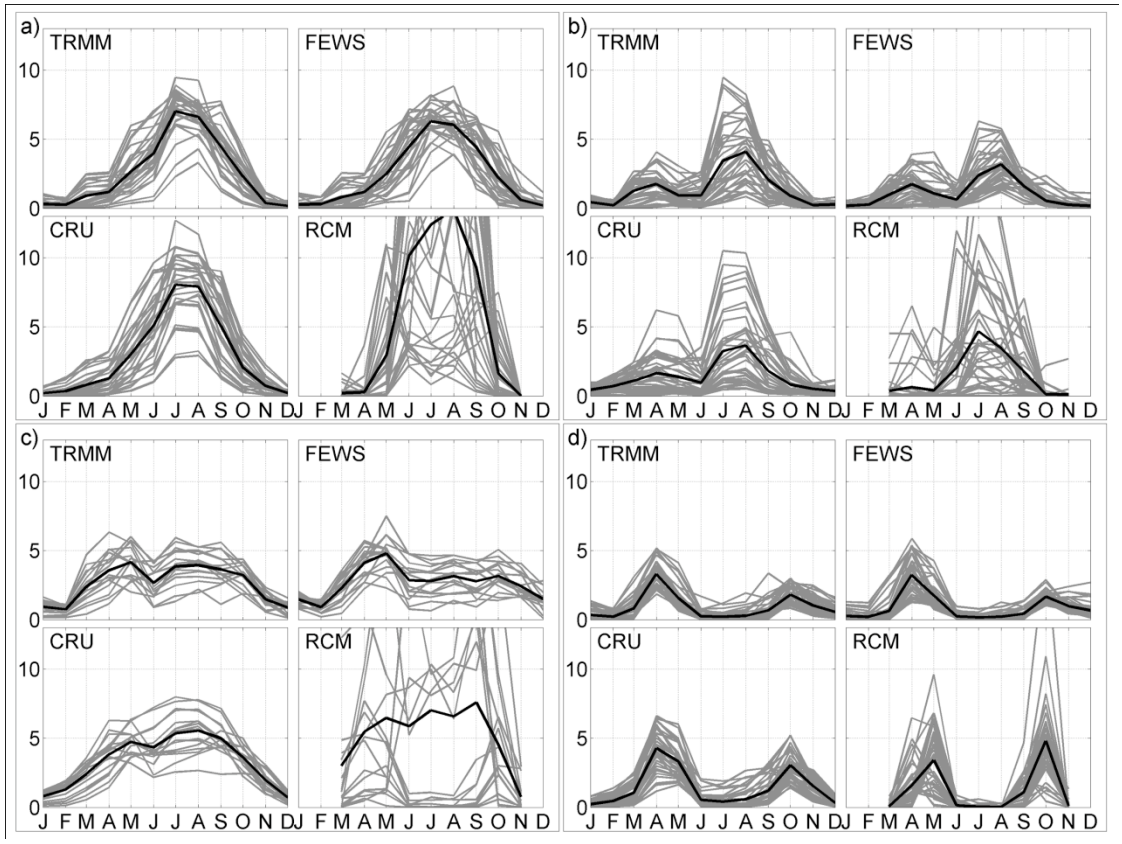

Figure 2.8: Annual rainfall cycles at 1° x 1° grid-points over the (a) northwest, (b) northeast, (c) southwest and (d) southeast study regions (Figure 2.7), as recorded by TRMM, FEWS, CRU and the MM5 climate-mode simulation. Regional averages are indicated with solid black lines.

Together, Figures 2.6-2.8 demonstrate that the cycle of precipitation in this region is complicated, with large variations from east to west as well as north to south. For example, from late May to June rainfall declines over northeastern Ethiopia, while at the same latitude the summer rainy season intensifies over the northwestern highlands. Thus, there is a westward shift in rainfall in addition to a northward shift. Again, these patterns are not consistent with a smoothly varying, zonally symmetric model of precipitation in this region.

2.5.2 The Monsoon Jump over the GHA

To further resolve intraseasonal shifts in GHA rainfall, daily time resolution is needed. Figure 2.9 shows the annual cycle of TRMM rainfall averaged between 33 and 43 degrees east longitude for 1998 through 2006, plus the 9-year climatology. This figure ignores zonal asymmetries, but is instructive in understanding abrupt seasonal transitions.

All of the nine years demonstrate some common features. In January through mid-March, the primary rainfall band is located near 10°S. In many years and the climatology, a weaker rainfall band appears south of 10°N during late February or early March. This weak rainfall band is associated with an early phase of the Ethiopian spring rainy season (*belg*), primarily over the southwestern focus region (Figures 2.7 and 2.8).

An abrupt transition occurs every year between late March and the end of May. During the transition, the rainfall maximum jumps approximately 20° of latitude, from 10° S to 10° N – a monsoon jump. This jump is larger than over West Africa, where a monsoon jump of approximately 5° latitude is observed [*Sultan and Janicot*, 2000, 2003a, 2003b; *Hagos and Cook*, 2007]. This East African monsoon jump is a persistent climatological feature. It is clearly seen in the climatology though, as expected, the abruptness of the transition is somewhat smoothed by averaging. Similar features can be observed in the FEWS dataset (not shown).

Looking more closely at the timing of the jump (April and May), one can see that the transition occurs in several stages which vary from year to year. In 2003, for example, a "first jump" in early April brings the precipitation maximum from south of the equator to the equatorial region (0°N - 7°N). In late May, another jump occurs, bringing rainfall to 10° N. A similar two-stage transition is also clearly observed in 2002 and 2005. In other years (e.g., 2000), one jump from approximately 10° S to 7°

N occurs in April, after which the rainfall north of the equator migrates slowly northward and intensifies; in these years the second jump is not pronounced. The timing of the first jump can vary between 20 March and 20 April. The subsequent northward shift from 7° N to 10° N occurs between early May and early June.

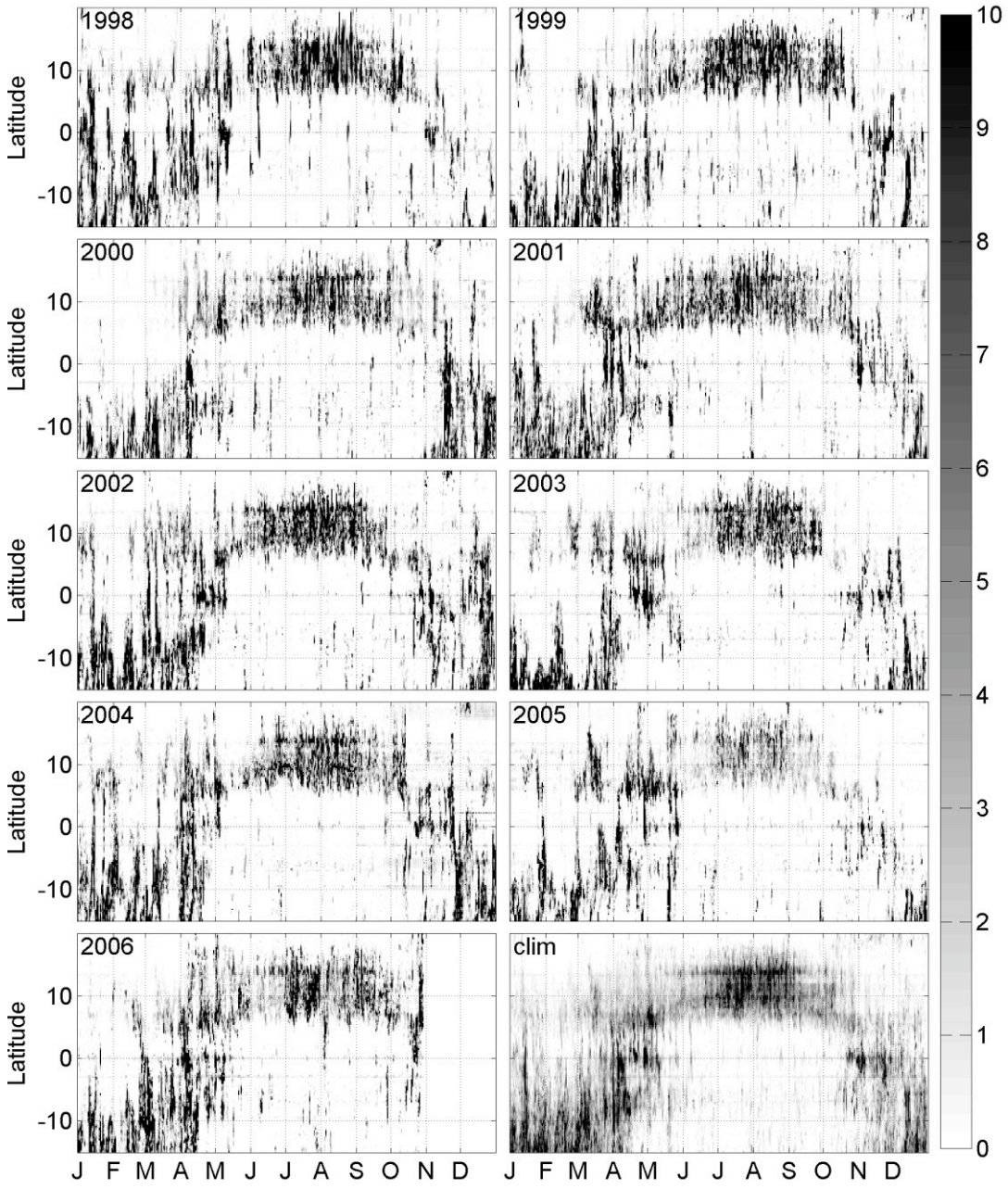

Figure 2.9: Daily TRMM precipitation (mm/day) averaged between 33º and 43º E longitude for 9 years (1998-2006) and a climatology.

During the transition period (April and May), two rainfall bands are often present: one band persisting south of the equator and second developing north of the equator. In this sense, the transition is not precisely a "jump" in rainfall, but rather the rapid development of a second branch of rainfall north of the equator. Later in the season, the southern branch dissipates or, in another interpretation, migrates rapidly northward to merge with the northern branch (Semazzi, personal communication). The two rainfall bands may represent a double ITCZ, similar to that observed by *Anyah and Semazzi* [2006] during October and November. For simplicity we will continue to refer the abrupt latitude transitions over the GHA as "jumps", though it is understood that rainfall south of the equator may persist for a short time after the onset of rainfall in the north.

During some years (e.g., 1999, 2003, 2004), a reversed jump is also present during boreal fall, while in other years (e.g., 2001, 2005, 1998) the southern recession of rainfall is smoother. When the reverse jump is present, the latitude of maximum rainfall shifts abruptly from 10° N to the equator in mid-October, and then from the equator to about 10° S in early December.

The MM5 simulations capture the dominant features of these jumps in 2002 and 2003 (Figure 2.10). The timing of the transitions for 2002 and 2003 agrees very well with the observations. In the climate simulation, the day-to-day variability is suppressed because of the smoothly varying lateral and surface boundary conditions. Nonetheless, relatively abrupt shifts in the latitude of rainfall occur, suggesting a non-linear response to the smooth external forcing. In contrast to the individual years, the initial jump in the climate simulation is somewhat later than in the observations. In all three model simulations, persisting summer rainfall south of the equator is a result of the anomalous precipitation near Lake Victoria and over the western Indian Ocean (Figure 2.4).

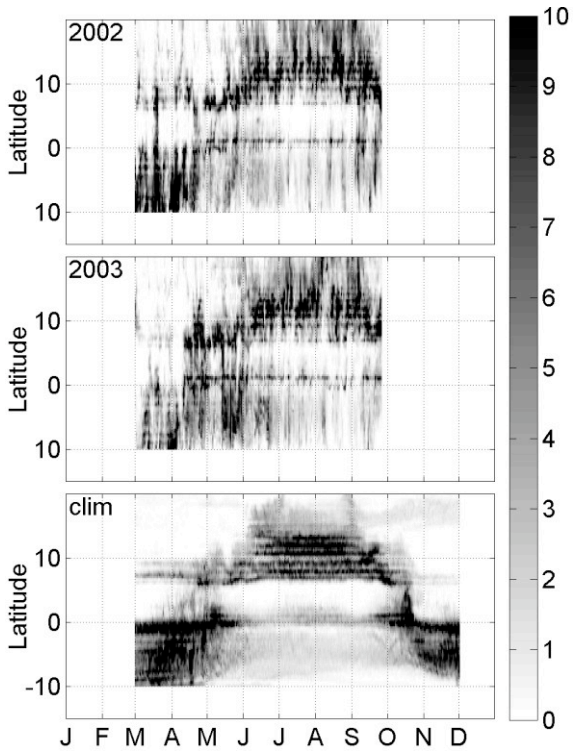

Figure 2.10: Daily MM5 simulated precipitation (mm/day) averaged between 33º and 43º E longitude for two years (2002-2003) and a climate-mode simulation.

Based on the timing of these jumps, it is useful to divide the evolution of the boreal summer rainy season into three stages. The first stage occurs in March before the first jump. The second, transitional stage occurs in between the jumps during the last half of April and the first half of May. The final stage, associated with the summer rainy season persists from June through early September. In this three-stage description of the monsoon onset, the Ethiopian *belg* rainy season (MAM) is divided between the first and second stages described above, while the summer rainy season (*kiremt*) is associated with the final stage.

Figures 2.11a-f show precipitation maps over Ethiopia for each stage at quarter degree resolution. During Stage 1 (March), precipitation is weak and primarily confined to the southwestern part of the country. In the Stage 2 (April/May), precipitation covers southern and eastern Ethiopia. This is the primary rainy season in

the south. In Stage 3 (June), the rainfall is strongest in the northwestern highlands. The summer precipitation pattern shown here for June continues through September.

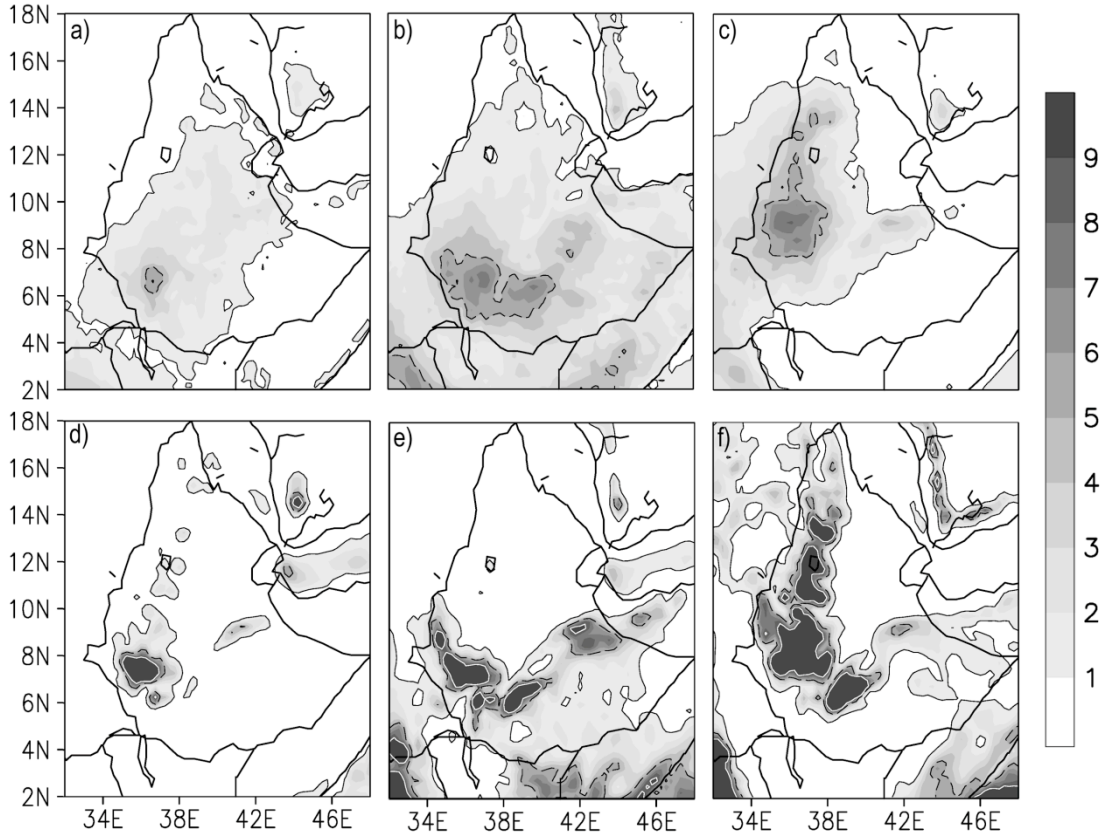

Figure 2.11: (Top) Maps of precipitation (mm/day) based on TRMM precipitation data for (a) Stage 1, (b) Stage 2, and (c) Stage 3 of the rainy season onset. (Bottom) MM5 climate-mode precipitation for (d) Stage 1, (e) Stage 2, and (f) Stage 3.

The hydrodynamical features that accompany these jumps are examined below to better understand why they occur, and how they are related to larger-scale circulation patterns and moisture sources.

2.5.3 Monsoon Onset Hydrodynamics

Figures 2.12a, b, and c show low-level (850 hPa) geopotential heights and moisture flux vectors from the MM5 climate mode simulation for Stages 1, 2, and 3,

respectively. Before the first jump, in Stage 1 (March), the low-level moisture flux is primarily easterly across the Horn of Africa, including Ethiopia. Between the equator and about 10°N the zonal geopotential height gradient is positive. The resulting flow down the height gradient transports modest amounts of moisture through the Turkana channel from the Arabian Sea. Recall that precipitation rates are quite low north of the equator during this period (Figure 2.11).

In Stage 2 (April/May), low geopotential heights over the western part of the domain persist, but are located further north. Southerly flow organizes along the equatorial coast forming the meridional branch of the Somali jet. The jet brings moisture from the Southern Hemisphere into southern Ethiopia, producing rainfall on the southern slopes of the Ethiopian plateau.

In June (Stage 3), the geopotential height field is dominated by two features: 1) the Indian monsoon trough which extends over the Arabian Peninsula, and 2) a ridge located along the East African topography in the south of the domain. These features generate a very strong geopotential height gradient from the southwest to the northeast corner of the domain. A trough in the western part of the domain persists as well, located still further north over the Sudan.

The fully formed Somali jet flows across the southwest-northeast pressure gradient. Both the meridional and zonal branches of the jet are now present and the meridional cross-equatorial branch of the jet is wider than in April/May. The zonal (northern) branch, not present in April/May, carries moisture across the Arabian Sea toward the Indian monsoon, and thus diverts the primary moisture source that fueled the Ethiopian spring rains.

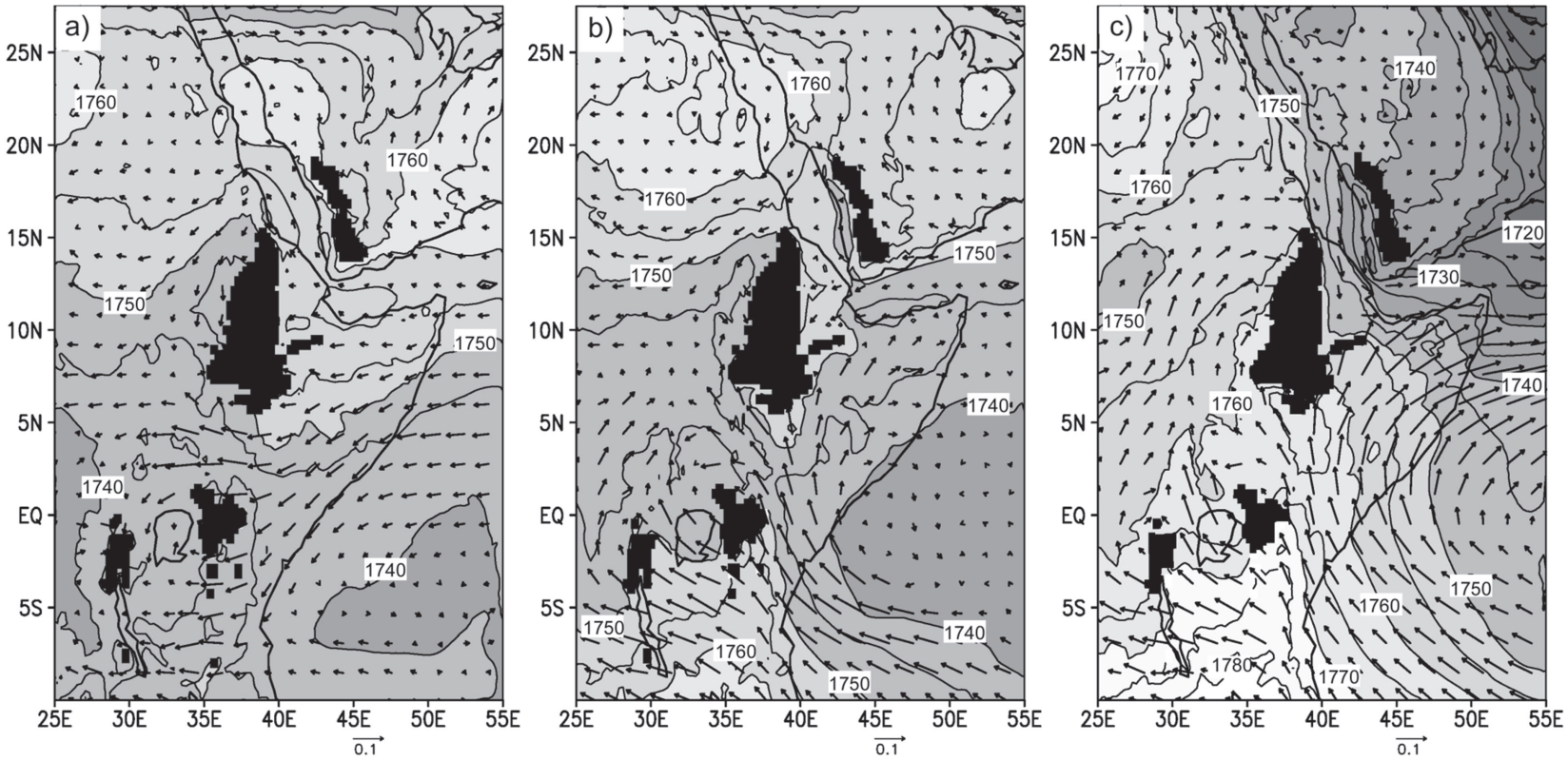

Figure 2.12. Maps of 825 hPa geopotential height (m) and moisture flux ($g/m^2/s$) based on the MM5 climate-mode simulation for (a) Stage 1, (b) Stage 2, and (c) Stage 3 of the rainy season onset. Grid points below the topography are shaded black.

During the summer, moisture is drawn into northern Ethiopia by a combination of factors. First, southeasterly flow associated with the trough over the Sudan brings moisture northward from the Congo basin. Second, the deep monsoon trough to the east introduces a negative geopotential height gradient across northern Ethiopia and the Red Sea, drawing the moisture eastward towards northwestern Ethiopia and Eritrea. Over the northwestern Ethiopian highlands, this inflow provides moisture for the summer rainy season. These results are consistent with those of *Camberlin* [1997] who shows summer rainfall over northern Ethiopia to be highly correlated with the strength of Indian monsoon indices. A deepening of the Indian monsoon trough leads both to increased Indian monsoon rainfall, and to stronger westerlies across northern Ethiopia, drawing increased moisture from central Africa [*Vizy and Cook*, 2003].

Figure 2.13 provides validation of these results using the NCEP reanalysis. As before, Figures 2.13a, b, and c show low-level (925 hPa) geopotential heights and moisture flux vectors from the NCEP reanalysis for Stages 1, 2, and 3, respectively. All of the primary features discussed above are present in the reanalysis. However, many detailed features, such as the horizontal structure of the coastal Somali jet and the flow through the Turkana channel, are not resolved in the 2.5º reanalysis fields

In both the model and the reanalysis (Figures 2.12 and 2.13), the meridional branch of the Somali jet forms along the East African topography almost a month before the zonal branch. This is in contrast to the original description of the springtime development of the jet by *Findlater* [1971] who suggested that the full jet forms offshore in February and slowly moves onshore throughout the spring.

The results presented in this section are robust in both the model and the observations/reanalysis. However, the model simulation is important in that it solidifies the physical link between circulation and precipitation processes that would otherwise only be observed in independent datasets.

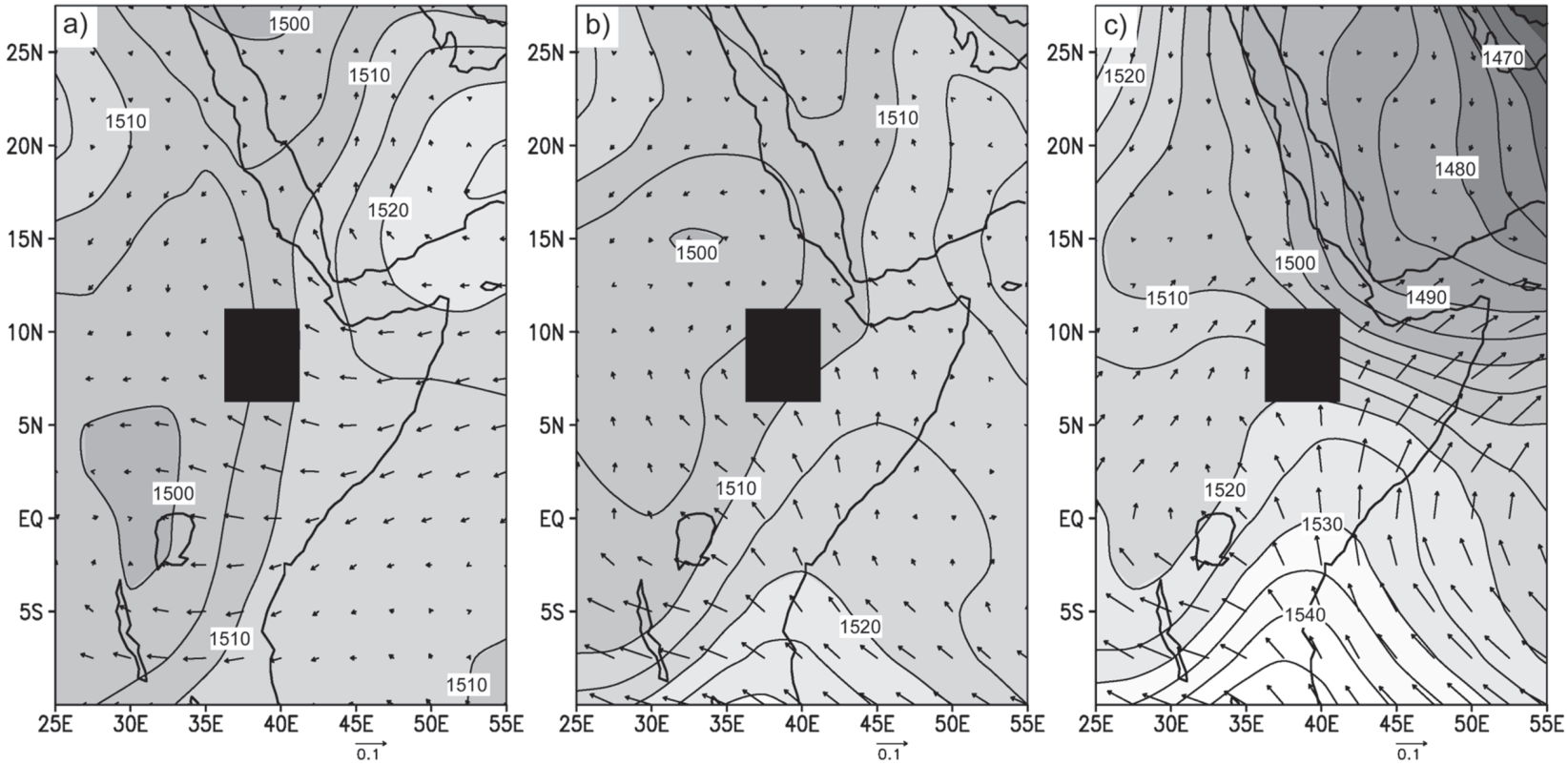

Figure 2.13. Maps of 850 hPa geopotential height (m) and moisture flux ($g/m^2/s$) based on the NCEP reanalysis for (a) Stage 1, (b) Stage 2, and (c) Stage 3 of the rainy season onset. Grid points below the topography are shaded black.

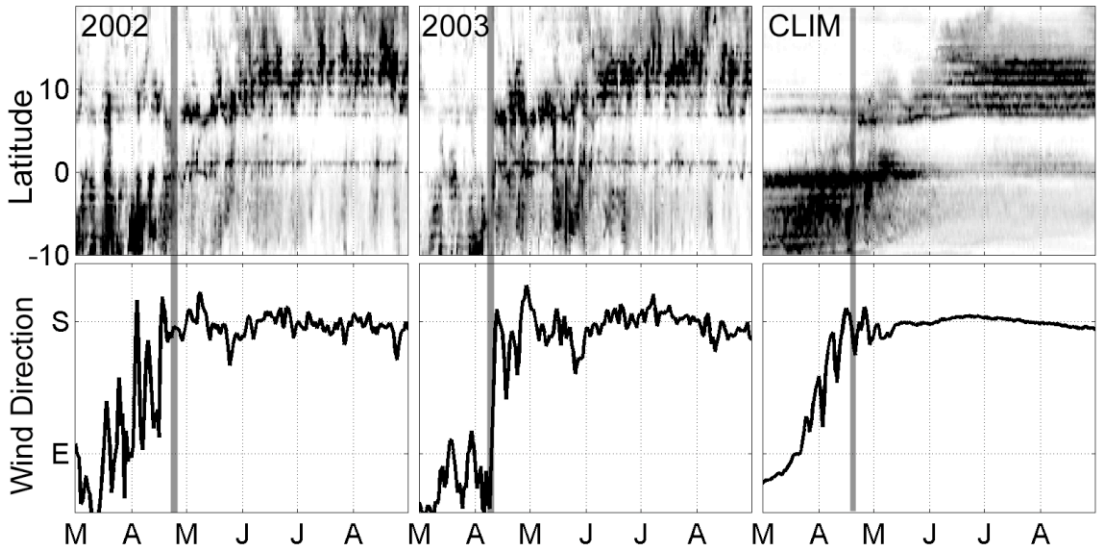

Figure 2.14: (Top) Zonally-averaged precipitation (33°-43° E) and (bottom) 910 hPa equatorial wind direction averaged over 38°E-45°E longitude and 2.5°S-2.5°N latitude based on 2002, 2003 and climate-mode simulations. Gray-scale is the same as in Figure 2.9. Vertical grey lines indicate the timing of the first precipitation jump.

2.5.4 Timing of the Monsoon Jumps

Figure 2.14 demonstrates the association between the timing of first monsoon jump, which initiates the spring rains in southern Ethiopia, and the formation of the meridional branch of the Somali jet. The top row of Figure 2.14 shows zonally-averaged precipitation (33°E to 43°E) for the 2002, 2003 and climate-mode simulations. The bottom row displays the 910 hPa wind direction averaged over a box between 38°E-45°E and 2.5°S-2.5°N. The flip in these equatorial winds from easterly to southerly is used as a proxy for the formation of the meridional branch of the Somali jet. Grey vertical lines mark the approximate date of the first jump in precipitation for each simulation. It is clear that the timing of the most-prominent precipitation jump corresponds with a shift in the direction of the equatorial winds.

In 2002 and 2003, the equatorial wind direction changes abruptly in both the model simulations and the NCEP reanalysis (not shown). In 2002, equatorial winds oscillate for several weeks between easterly and southerly before stabilizing in mid-April. Rainfall north of the equator is likewise intermittent in early April. The final northward jump in rainfall (grey vertical line) occurs roughly one week after winds have stabilized. In 2003, the flip in wind direction is remarkably abrupt, occurring over a two-day period. The onset of rainfall north of the equator is similarly abrupt and coincident with the change in wind direction.

In the climate-mode simulation the wind direction changes more smoothly, over the course of about a month. This suggests that winds within the domain are influenced by the wind field at the lateral boundaries, which is smoothly interpolated from monthly mean reanalysis. The jump in rainfall is nonetheless present in the climate simulation, but does not occur until the end of April, after the meridional jet has completely formed.

The sample size is too small to infer any statistical correlation between the two processes (the flip in equatorial wind direction and jump in precipitation). However, the similarity in timescales, along with the simple physical mechanism linking cross-equatorial moisture transport to southern Ethiopian precipitation, strongly suggests that the two events are connected. This analysis does not, however, establish a cause-and-effect relationship between the two events.

Figure 2.15 is similar to Figure 2.14 but focused on the second precipitation jump, which brings rainfall to the northwestern Ethiopian highlands, and the formation of the zonal branch of the Somali jet. To capture zonal jet formation, the wind direction is averaged between 50ºE – 55ºE and 10ºN – 15ºN, off of the tip of Somalia. In both 2002 and 2003, the wind direction in this region is chaotic during March and April, before the stable southwesterly jet is established in mid-May. In both years, the

jump in rainfall (grey vertical lines) occurs several weeks after the jet is first established. However, initially, the jet does not extend across the Arabian Sea, but feeds a local circulation off the coast of Africa (not shown). The jump in rainfall occurs only after the zonal branch of the jet strengthens, and the winds across northern Ethiopia switch from easterly to westerly.

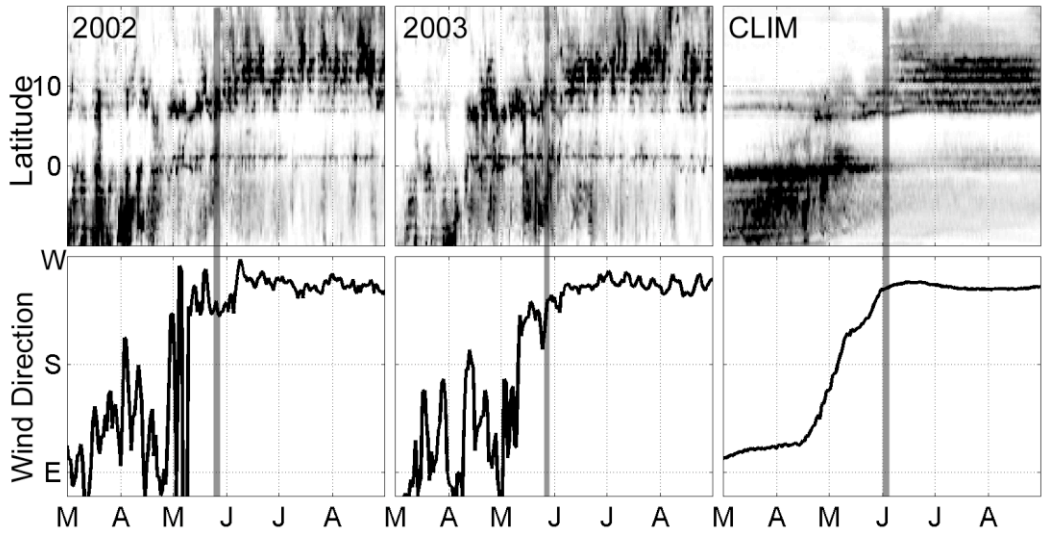

Figure 2.15: (Top) Zonally-averaged precipitation (33°-43° E) and (bottom) 910 hPa equatorial wind direction averaged over 50°E-55°E longitude and 5°N-10°N latitude based on 2002, 2003 and climate-mode simulations. Gray-scale is the same as in Figure 2.9. Vertical grey lines indicate the timing of the second precipitation jump.

In the climate-mode simulation, the wind direction changes smoothly over a month and a half. The onset of rainfall occurs only after the wind direction has stabilized and the full jet has formed.

2.6 Conclusions

Improved forecasts of rainy season onset and termination over the GHA would greatly benefit people in the region, for example, by allowing farmers to plan when to plant their crops and communities to better manage their water resources. However,

forecasting the timing of intraseasonal changes in rainfall is difficult, and a better understanding of the processes governing these changes is necessary before useful forecasts can be achieved.

In this study, we have examined the onset of the boreal spring and summer rainy seasons over the GHA, using observed and analyzed datasets and regional climate model simulations. Precipitation climatologies were generated from three precipitation datasets, two primarily satellite-based (TRMM and FEWS), and one surface-based (CRU). While each of these datasets has disadvantages (the satellite-based records are short, and the surface stations are sparse and available only over land), combined with the regional climate model simulations they provide a consistent and reliable picture of the rainy season evolution.

The MM5 simulations using 2002, 2003 and climatological lateral and surface boundary conditions were carried out at 30 kilometer resolution. These simulations augment existing three-dimensional datasets (e.g., NCEP-2 reanalysis) by providing high enough spatial resolution to capture the complex topography of East Africa (e.g., the Turkana Channel), and linking the atmospheric circulation with a realistic precipitation cycle.

The rainfall climatologies and simulations both show that rainfall over the GHA is not zonally uniform as would be suggested by a simple migration of a zonally-symmetric ITCZ. Because of this, the rainfall cycles and the relative importance of different rainy seasons vary significantly from one region to another. Over Ethiopia, for example, four separate regions can be identified with unique seasonal cycles. These complexities must be considered when generating regional forecasts.

A primary result of this paper is the documentation of a 20° latitude jump in rainfall that occurs in the boreal spring over the GHA. The jump occurs during the months of April and May at which time the rainfall moves abruptly from

approximately 10° south of the equator to 10° north of the equator. The precipitation jump is larger than the 5° latitude jump documented during the onset of the West African monsoon [*Sultan and Janicot*, 2000].

The full jump is often composed of two smaller jumps. A large first jump occurs between late March and early April when precipitation moves from 10°S into the northern hemisphere, bringing rain to the southern slopes of the Ethiopian plateau. The second smaller jump occurs in May, bringing the rainfall band further north into the western Ethiopian highlands. Thus, the onset of the monsoon over the GHA is divided into three stages: 1) early spring (March) before the initial jump, 2) a transitional period (April/May) between the two jumps, and 3) the summer rainy season (June) after the second jump.

The associated circulation patterns were investigated with the MM5 simulations, using the NCEP-2 reanalysis for a course-scale validation. When examined separately, each of the onset stages represents a different phase in development of the Somali jet. During Stage 1, the equatorial winds are easterly and the Somali jet has not yet begun to form. During Stage 2, only a meridional branch of the Somali jet is present; equatorial winds are southerly, but not yet diverted eastward towards the Arabian Sea. This provides a moisture source for the southern slopes of the Ethiopian plateau. The Somali jet is fully formed in Stage 3.

The circulation changes associated with the formation of the jet are often abrupt and roughly coincident with the jumps in precipitation. This is particularly true in 2003 when the equatorial winds flip direction over a period of two days at the same time as the precipitation jumps north of the equator. This process is very different than over West Africa [*Sultan and Janicot*, 2000], where the monsoon jump is thought to be caused by a local inertial instability along the Gulf of Guinea [*Hagos and Cook*, 2007].

To our knowledge, the two-phase development of the Somali jet and its association with GHA precipitation has not been previously documented in the literature. From early observations [*Findlater*, 1971], the jet was thought to form offshore in the early spring, and slowly move onshore as the season develops.

This study identifies a monsoon jump over the GHA, and shows that the precipitation jump coincides with the formation of the Somali jet. However, to support prediction, cause-and-effect relationships must be established between the background climate regime, the Somali jet development, and the associated changes in precipitation. The model simulations presented here lay the groundwork for exploring these subjects in greater depth.

2.7 Acknowledgements

This research is published in the Journal of Geophysical Research, Atmospheres, coauthored by Dr. Kerry Cook, currently at the University of Texas, Austin. The research was supported by the NASA Earth Systems Science Fellowship program and NSF grant # ATM-0415481. We extend our gratitude to Dr. Edward Vizy for his valuable assistance with the model simulations and analysis, and also to three anonymous reviewers at the Journal of Geophysical Research for their very careful and insightful comments which have greatly improved this manuscript.

REFERENCES

Anyah, R. O., and F. H. M. Semazzi (2004), Simulation of the sensitivity of Lake Victoria basin climate to lake surface temperatures, *Theoret. Appl. Climatol., 79*, 55-69.

Anyah, R. O., and F. H. M. Semazzi (2006), Climate variability over the Greater Horn of Africa based on NCAR AGCM ensemble, *Theoret. Appl. Climatol., 86*(1-4), 39-62.

Anyah, R. O., and F. H. M. Semazzi (2007), Variability of East African rainfall based on multiyear RegCM3 simulations, *Int. J. Climatol., 27*(3), 357-371.

Behera, S. K. , J. J. Luo, S. Masson, P. Delecluse, S. Gualdi, A. Navarra, and T. Yamagata (2005), Paramount impact of the Indian Ocean dipole on the East African short rains: A CGCM study, *J. Clim.*, *18*(21), 4514-4530.

Beltrando, G., and P. Camberlin (1993), Interannual variability of rainfall in the Eastern Horn of Africa and indicators of atmospheric circulation, *Int. J. Climatol*., 13(5), 533-546.

Bhatt, U. S. (1989), Circulation regimes of rainfall anomalies in the African-South Asian monsoon belt. *J. Clim, 2*(10), 1133-1144.

Black, E. (2005), The relationship between Indian Ocean sea-surface temperature and east African rainfall, *Philos. Trans. R. Soc., Ser. A, 363,* 42-47.

Black, E., J. Slingo and K. R. Sperber (2003), An observational study of the relationship between excessively strong short rains in coastal East Africa and Indian Ocean SST, *Mon. Weather Rev., 131*(1), 74-94.

Blackadar, A.K. (1979), High resolution models of the planetary boundary layer, *Adv. Environ. Sci. Eng., 1*, 50-85.

Bowden, J. H., and F. H. M. Semazzi (2007), Empirical analysis of intraseasonal climate variability over the Greater Horn of Africa, *J. Clim.,20*(23), 5715-5731.

Camberlin, P. (1995), June-September rainfall in north-eastern Africa and atmospheric signals over the tropics: A zonal perspective, *Int. J. Climatol., 15*, 773-783.

Camberlin, P. (1997), Rainfall anomalies in the source region of the Nile and their connection with the Indian summer monsoon. *J. Clim., 10,* 1380-1392.

Camberlin P., and R. E. Okoola (2003), The onset and cessation of the "long rains" in eastern Africa and their interannual variability, *Theoret. Appl. Climatol. (75)*, 43-54.

Camberlin, P., and N. Philippon (2002), The East African March-May rainy season: Associated atmospheric dynamics and predictability over the 1968-1997 period, *J. Clim., 15*, 1002-1019.

Camberlin, P., and J. G. Wairoto (1997), Intraseasonal wind anomalies related to wet and dry spells during the "long" and "short" rainy seasons in Kenya, *Theoret. Appl. Climatol., 58,* 57-69.

Clark, C. O., P. J. Webster, and J. E. Cole (2003), Interdecadal variability of the relationship between in the Indian Ocean zonal mode and East African coastal rainfall anomalies, *J. Clim*., 16(3), 548-554.

Conway, D., C. E. Hanson, R. Doherty, and A. Persechino (2007), GCM simulations of the Indian Ocean dipole influence on East African rainfall: Present and future, *Geophys. Res. Lett., 34* (3), L03705. doi: 10.1029/2006GL027597

Dudhia, J. (1989), Numerical study of convection observed during the winter monsoon experiment using a mesoscale two-dimensional model. *J. Atmos. Sci., 46***,** 3077-3107.

Findlater, J. (1969), A major low-level air current near the Indian Ocean during the northern summer, *Q. J. R. Meteor. Soc., 95*, 362-380.

Findlater, J. (1971), Mean monthly airflow at low levels over the western Indian Ocean, *Geophys. Memoirs*, *16*(115), 1-48.

Flohn, H. (1987), Rainfall teleconnections in northern and northeastern Africa, *Theoret. Appl. Climatol., 38*(3), 191-197.

Gissila T., E. Black, D. I. F. Grimes, and J. M. Slingo (2004), Seasonal forecasting of the Ethiopian summer rains, *Int. J. Climatol., 24*(11), 1345-1358.

Goddard, L. and Graham N. E. (1999), Importance of the Indian Ocean for simulating rainfall anomalies over eastern and southern Africa, *J. Geophys. Res., 104*(D16), 19099-19116.

Grell, G. A., J. Dudhia, and D. R. Stauffer (1994), A description of the fifth-generation Penn State/ NCAR mesoscale model (MM5), *NCAR Tech. Note, NCAR/TN-398+STR,* 112 pp., Natl. Cent. For Atmos. Res., Boulder, Colo.

Hagos, S. M., and K. H. Cook (2007), Dynamics of the West African monsoon jump, *J. Clim.,20*(21), 5264-5284.

Hastenrath, S., A. Nicklis, and L. Greischar (1993), Atmospheric-hydrospheric mechanisms of climate anomalies in the western equatorial Indian Ocean. *J. Geophys. Res.,* 98, 20219-20235.

Herman, A., V. B. Kumar, P. A. Arkin, and J. V. Kousky (1997), Objectively determined 10-day African rainfall estimates created for famine early warming systems, *Int. J. Remote Sens.**, 18,*** 2147-2159.

Huffman, G. J., R. F. Adler, D. T. Bolvin, G. Gu, E. J. Nelkin, K. P. Bowman, Y. Hong, E. F. Stocker, and D. B. Wolff (2007), The TRMM multi-satellite precipitation analysis (TMPA): Quasi-global, multiyear, combined-sensor precipitation estimates at fine scales. *J. Hydrometeor., 8* (1), 38-55.

Indeje, M., F. H. M. Semazzi and L. J. Ogallo (2000), ENSO signals in East African rainfall seasons, *Int. J. Climatol., 20*(1), 19-46.

Indeje, M., F. H. M. Semazzi, L. Xie, L. J. Ogallo (2001), Mechanistic model simulations of the East African climate using NCAR regional climate model: Influence of large-scale orography on the Turkana low-level jet, *J. Clim.**, 14***,** 2710-2724.

Kain, J. S. (2004), The Kain-Fritsch Convective Parameterization: An update, *J. Appl. Meteorol., 43*, 170-181.

Kanamitsu, M., W. Ebisuzaki, J. Woollen, S. K. Yang, J. J. Hnilo, M. Fiorino, and G. L. Potter (2002), NCEP-DOE AMIP-II Reanalysis (R-2), *Bull. Amer. Meteorol. Soc.*, *83*, 1631-1643.

Kinuthia, J. H., and G. C. Asnani (1982), A newly found jet in North Kenya (Turkana Channel), *Mon. Weather Rev., 110*, 1722-1728.

Korecha D., and A. G. Barnston (2007), Predictability of June-September rainfall in Ethiopia, *Mon. Weather Rev., 135*(2), 628-650.

Luseno, W. K., J. G. McPeak, C. B. Barrett, P. D. Little, and G. Gebru (2003), Assessing the value of climate forecast information for pastoralists: Evidence from southern Ethiopia and northern Kenya, *World Development, 31,* 1477-1494.

Mitchel, T. D., and P. D. Jones (2005), An improved method of constructing a database of monthly climate observations and associated high-resolution grids, *Int. J. Climatol., 25*(6), 693-712.

Mlawer, E. J., S. J. Taubman, P. D. Brown, M. J. Iacono, and S. A. Clough (1997), Radiative transfer for inhomogeneous atmospheres: RRTM, a validated correlated-k model for the longwave, *J. Geophys. Res., 102*(D14), 16663-16682.

Mutai, C. C., and M. N. Ward (2000), East African rainfall and the tropical circulation/convection on intraseasonal timescales, *J. Clim., 13*, 3915-3939.

New, M., D. Lister, M. Hulme, and I. Makin (2002), A high-resolution data set of surface climate over global land areas, *Clim. Res.**, 21,*** 1-25.

Ogallo, L. J. (1988), Relationships between seasonal rainfall in East Africa and the Southern Oscillation, *Int. J. Climatol., 8*, 31-43.

Okoola, R. E. (1999), A diagnostic study of the eastern Africa monsoon circulation during the northern hemisphere spring season. *Int. J. Climatol., 19*, 143-168.

Patricola, C. M., and K. H. Cook (2007), Dynamics of the West African monsoon under mid-Holocene precessional forcing: Regional climate model simulations, *J. Clim., 20*, 694-716.

Pohl, B., and P. Camberlin (2006a), Influence of the Madden-Julian Oscillation on East African rainfall. I: Intraseasonal variability and regional dependency, *Q. J. R. Meteorol. Soc., 132*(621), 2521-2539.

Pohl, B., and P. Camberlin (2006b), Influence of the Madden-Julian Oscillation on East African rainfall. II: March-May season extremes and interannual variability, *Q. J. R. Meteorol. Soc. 132*(621), 2541-2558.

Rodwell, M. J., and B. J. Hoskins (1995), A model of the Asian summer monsoon. Part II: Cross-equatorial flow and PV behavior, *J. Atmos. Sci*, *52*(9), 1341-1356.

Segele Z. T., and P. J. Lamb (2005), Characterization and variability of Kiremt rainy season over Ethiopia, *Meteorol. Atmos. Phys., 89*(1-4), 153-180.

Shea, D. J., K. E. Trenberth, and W. R. Reynolds (1992), A global monthly sea-surface temperature climatology, *J. Clim., 5*, 987-1001.

Shanko, D., and P. Camberlin (1998), The effects of the Southwest Indian Ocean tropical cyclones on Ethiopian drought. *Int. J. Climatol., 18*, 1373-1388.

Slingo, J., H. Spencer, B. Hoskins, P. Berrisford, and E. Black (2005), The meteorology of the Western Indian Ocean, and the influence of the east African highlands, *Philos. Trans. R. Soc., Ser. A, 363*, 25-42.

Sultan, B., and S. Janicot (2000), Abrupt shift of the ITCZ over West Africa and intra-seasonal variability, *Geophys. Res. Lett.*, *27*, 3353-3356.

Sun, L. Q., F. H. M. Semazzi, F. Giorgi, and L. Ogallo (1999), Application of the NCAR regional climate model to eastern Africa 2. Simulation of interannual variability of short rains, *J. Geophys. Res. 105*, 6549-6562.

Thiaw, W. M., A. G. Barnston, and V. Kumar (1999), Predictions of African rainfall on the seasonal timescale, *J. Geophys. Res.*, *104 (*D24), 31589-31597.

Verdin, J., C. Funk, G. Senay, and R. Choularton (2005), Climate science and famine early warning, *Philos. Trans. R. Soc., Ser. B, 360*, 2155-2168.

Vizy, E. K., and K. H. Cook (2002), Development and application of a mesoscale climate model for the tropics: Influence of sea surface temperature anomalies on the West African monsoon, *J. Geophys. Res., 107*(D3), 4023, doi:10.1029/2001JD000686

Vizy, E. K., and K. H. Cook (2003) Connections between the summer east Africa and Indian rainfall regimes, *J. Geophys. Res., 108*(D16), 4510, doi:10.1029/2003JD003452

Xue, Y., H.-M. H. Juang, W.-P. Li, S. Prince, R. DeFries, Y. Jiao, and R. Vasic (2004), Role of land surface processes in monsoon development: East Asia and West Africa, *J. Geophys. Res.,109*(D3), D03105, doi:10.1029/2003JD003556.

Zorita, E., and F. F. Tilya (2002), Rainfall variability in Northern Tanzania in the March-May season (long rains) and its links to large-scale climate forcing, *Clim. Res., 20,* 31-40.

CHAPTER 3

STATISTICAL INDICES OF THE NORTHWARD RAINFALL PROGRESSION OVER EASTERN AFRICA

3.1 Introduction

Over eastern Africa, as in much of the tropics, the seasonal cycle of rainfall is dominated by the north-south migration of the Intertropical Convergence Zone (ITCZ), following the solar insolation cycle. Planting and harvesting seasons are timed to correspond with the passage of ITCZ rainfall. Agricultural regions from Tanzania to Ethiopia experience at least one of their primary growing seasons between January and July, during the northward progression of the ITCZ. The "long rains" in Kenya and northern Tanzania, the *belg* rains in Ethiopia, and *gu* rains in Somalia all peak during March-May, when the latitude of rainfall is moving northward most rapidly (Figure 3.1a). Understanding the timing and variability of this northward progression is thus of much importance to farmers throughout the region.

Figure 3.1b demonstrates that the northward migration of rainfall over eastern Africa is not always smooth, but instead characterized by abrupt shifts in latitude. In 2003, for example, an abrupt northward shift, or "jump" in the latitude of rainfall is apparent on 11 April. This was followed by a temporary southward shift in May and a subsequent northward transition to 10° N at the beginning of June (Figure 3.1b). *Riddle and Cook* [2008] show that similar jumps occur in many years, but that the jumps vary in character and timing from one year to the next. These results are consistent with earlier studies [e.g., *Camberlin and Okoola*, 2003] which show significant interannual variability in the onset timing of March – May (MAM) "long

rains". Better understanding of the mechanisms controlling these jumps could improve forecasts at both short range (days to weeks) and seasonal timescales.

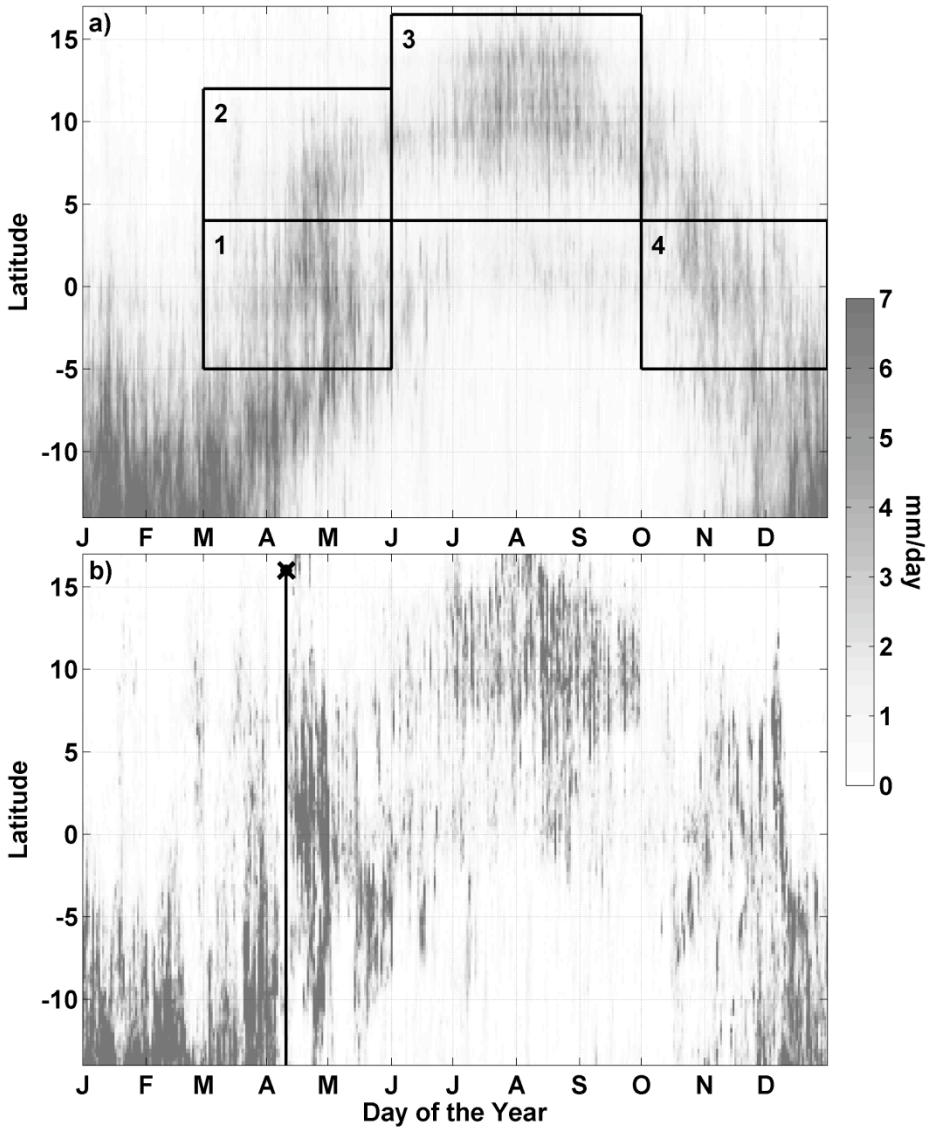

Figure 3.1: **(a)** Daily Tropical Rainfall Measuring Mission (TRMM) rainfall climatology averaged over 27.5 – 52.5 degrees E longitude. The data are displayed at 0.25 degree latitude increments. The climatological averages are taken over all years available for a given day (either 12 or 13 years, depending on the day). Boxes show seasons and latitude bands of several eastern African rainy seasons: 1) the long rains over Kenya, Uganda and northern Tanzania, 2) the *belg* rainy season over Ethiopia and *gu* rainy season over Somalia, 3) the *kiremt* rainy season over Ethiopia, and 4) the short rains over Kenya, Uganda and northern Tanzania. **(b)** Daily TRMM rainfall for 2003 averaged over the same longitude band as (a). The first rainfall jump in 2003, which occurs on 11 April, is marked with a black vertical line and an 'x' at top.

While previous studies have examined various aspects of local rainy season variability, a framework has not yet been established to describe the observed rainfall jumps over eastern Africa. The purpose of this paper is to develop statistical indices that capture spatial characteristics of the late January – late July rainfall cycle over eastern Africa, including rainfall jumps. The indices are then used to characterize variability over a sequence of years around the average seasonal cycle, and investigate atmospheric perturbations associated with jumps ahead or behind the mean seasonal progression. Though not addressed here, these indices could also be useful for exploring the short-range and seasonal predictability of rainfall transitions.

3.2 Background

Abrupt jumps in the latitude of ITCZ rainfall are not unusual in the tropics. In fact, when averaged globally, the ITCZ jumps abruptly from the winter to summer hemispheres during both the boreal and austral spring seasons [*Hu et al.,* 2007]. The jumps, which occur over approximately 10 days, are not uniform across the globe. Instead, they are observed in certain regions only, including eastern Africa, the Indian Ocean, the western Pacific and South America. Latitude jumps are not observed over central Africa, the Atlantic or the eastern Pacific [*Hu et al.*, 2007].

Theoretical studies of ITCZ dynamics have described how abrupt latitude shifts could occur in a purely oceanic environment [e.g., *Lindzen and Hou*, 1988; *Xian and Miller*, 2008]. However, many prominent ITCZ jumps occur over regions with a seasonal monsoon system (e.g., over the Indian Ocean and the western Pacific), suggesting that the observed rainfall jumps may often be associated with monsoon dynamics. Several studies have noted abrupt jumps in the latitude of rainfall during monsoon onsets, including during the onset of the West African monsoon [e.g., *Sultan*

and Janicot, 2000; *Hagos and Cook*, 2007] and the East Asian Monsoon [*Xue et al.*, 2004].

Eastern Africa is situated in a unique location at the western boundary of the Indian monsoon region, between central Africa (where the migration of the ITCZ is smooth) and the Indian Ocean (where the migration of the ITCZ is abrupt). *Riddle and Cook* [2008] describe two rainfall jumps over eastern Africa, one in April when the latitude of maximum rainfall transitions from south the equator (5° to 10° S) to just north of the equator (0° to 7° N). A second transition, which may be smooth or abrupt, occurs in late May and early June when the latitude of maximum rainfall moves from 7° N to 10° N. In some years, jumps into the southern hemisphere are also observed in October and November.

While latitude jumps over eastern Africa have only recently been highlighted, a body of literature has examined temporal and spatial characteristics of east African rainfall over a range of regions, seasons and timescales. We focus here on studies of rainy seasons that peak during March-May, when the ITCZ makes its transition from the southern to the northern hemisphere.

The March-May (MAM) season is arguably the least understood and the most complex of the eastern African rainy periods. Unlike other seasons, MAM rainfall averages over eastern Africa do not exhibit very strong relationships with external modes of variability such as El Nino or the Indian Ocean dipole mode [e.g., *Ogallo,* 1988; *Hastenrath et al.,* 1993]. Because of this, a number of authors have suggested that rainfall variability must be considered at smaller spatial and temporal scales [*Camberlin and Philippon,* 2002; *Zorita and Tilya*, 2003; *Camberlin et al.,* 2009].

Camberlin and Phillipon [2002] indentify equatorial East Africa (Kenya, Uganda and N. Tanzania), and Ethiopia as two regions with relatively strong internal coherence with respect to their interannual timeseries. However, studies focusing

narrowly within these "coherent" regions still indicate complex internal spatial relationships in MAM rainfall. *Camberlin et al.* [2009] show that station-to-station correlations of interannual timeseries across equatorial East Africa (EEA) are weaker in April and May than during any other rainy month. *Pohl et al.* [2006a, 2006b] suggest that a division between coastal and highlands regions is necessary to understand interactions between equatorial east African (EEA) rainfall variability and the Madden-Julien Oscillation (MJO). Within Ethiopia, studies have identified between four and six homogeneous sub-regions, each with different seasonal rainfall cycles and/or different modes of interannual variability [*Gissila et al.*, 2004; *Diro et al.*, 2008; *Riddle and Cook*, 2008].

Despite this complexity, some consistent patterns have emerged relating to MAM rainfall. In March and April, over equatorial East Africa (EEA), many authors [e.g., *Camberlin and Wairoto*, 1997; *Okoola*, 1999; *Camberlin and Philippon*, 2002; *Zorita and Tilya*, 2002; *Camberlin and Okoola*, 2003; *Pohl et al.,* 2006a*,* 2006b] observe a connection between wet (dry) conditions and equatorial westerly (easterly) anomalies in the mid to lower troposphere across the African continent. This connection is noted at a range of timescales from intraseasonal to interannual [e.g., *Camberlin and Phillipon*, 2002; *Camberlin and Okoola*, 2003]. In examining connections with MJO, *Pohl et al.* [2006a, 2006b] find that equatorial westerly anomalies are associated with deep convection over the EEA highlands, while easterly wind anomalies can be associated with positive rainfall anomalies at the coast.

In May, studies suggest that dry conditions over EEA are connected to an early onset of the Indian summer monsoon [*Camberlin and Phillipon*, 2003; *Camberlin et al.*, 2010]. This connection is also noted at both interannual [*Camberlin and Phillipon,* 2002] and intraseasonal [*Camberlin et al*., 2010] timescales. These authors suggest that the Indian monsoon flow creates divergent conditions over EEA.

Fewer studies have examined MAM rainfall over Ethiopia. *Camberlin and Phillipon* [2003] and *Habtemichael and Paegley* [1977] note a connection between MAM rainfall over Ethiopia and southward excursions of the subtropical westerly jet. *Shanko and Camberlin* [1998] demonstrate a negative correlation between Ethiopian rainfall in MAM and the number of tropical cyclones over western Indian Ocean. *Diro et al.* [2008] develop a seasonal prediction model for five Ethiopian sub-regions using global SSTs in the preceding eight months.

Riddle and Cook [2008] show that the onset of heavy rainfall over Ethiopia in April is coincident with an early stage in the development of the Somali Jet. During this early phase, a narrow cross-equatorial southerly jet (the "nascent" Somali Jet) forms at low levels along the eastern coast of Africa. In April, the nascent jet terminates over Ethiopia; only later in the season (late May) does the fully formed Somali Jet extend across the Arabian Sea. Others have also identified southerly and southeasterly flow from the Indian Ocean as the primary moisture source for the southern Ethiopian MAM rainy season [*Nicholson*, 2006; *Levin et al.*, 2009].

Studies of Ethiopian rainfall suggest that dry May conditions are associated with early onset of the Indian monsoon [*Riddle and Cook,* 2008; *Camberlin et al.,* 2010]. *Riddle and Cook* [2008] suggest that the development of the Arabian Sea branch of the Somali Jet removes the primary moisture source for the S. Ethiopian *belg* rainfall. *Levin et al.* [2009] note that the equivalent potential temperature of low-level air originating from the southern Indian Ocean decreases from April to July, making this a less productive source for convection in May, as opposed to March and April.

Together, previous studies suggest that rainfall variability over eastern Africa is complex, and that important changes occur between the beginning and end of the MAM period. Previous papers have generally handled these changing seasonal

conditions by dividing the rainy season into quasi-stationary intervals (usually months, or longer), or by subtracting the seasonal cycle and assuming that the anomalies are stationary. This paper takes a different approach, by focusing directly on describing seasonal cycle and using a large enough domain to capture the full northward progression of the ITCZ.

We use two different methods, a principal component analysis (PCA) and a dynamical cluster analysis, to calculate indices to capture the northward rainfall progression. Both of these techniques have been used previously in studies of east African rainfall. Principal component analyses have been used to examine interannual to decadal signals in MAM rainfall totals [e.g., *Camberlin and Phillipon*, 2002], characterize localized rainfall anomalies over EEA [*Pohl et al*., 2006a, 2006b], and to create an index of the monsoon onset and cessation over EEA [*Camberlin and Okoola*, 2003]. *Pohl et al.* [2005] used a dynamical cluster analysis to create a typology of circulation anomalies during the MAM and OND rainy seasons over eastern Africa. Here, these techniques are applied directly to daily rainfall fields to extract the seasonal signal over all of eastern Africa.

3.3 Methods

3.3.1 Dataset and domain selection

The rainfall dataset used for this study is the Tropical Rainfall Measurement Mission (TRMM) 3B42 V6 rainfall product [*Huffman et al*., 2007]. This product is derived using a combination of satellite sensors (passive microwave and infrared sensors, and the TRMM precipitation radar), and calibrated using monthly averaged rain gauge data. The TRMM product is available every three hours at a resolution of 0.25° x 0.25°. Data are available from 1998 to the present, representing 13 years of data for most months in our study. *Riddle and Cook* [2008] show that the TRMM

dataset shows similar seasonal patterns over Ethiopia to the CRU and CPC rainfall datasets.

Advantages of the TRMM dataset include high spatial and temporal resolution and uniform geographic coverage over both land and water. The primary disadvantage is the short duration of the dataset, which constrains analysis of variability at multiyear timescales. However, since the focus of this study is on spatial shifts in rainfall that occur over short (daily) timescales, we believe that the advantages of higher resolution and uniform coverage outweigh the disadvantages.

Before analyzing the rainfall data, the 3-hourly TRMM data are first converted to daily averages, and the 0.25° x 0.25° grid is converted to 1° x 1° resolution. This lower resolution has been subjectively determined, based on Hovmöller diagrams, to be sufficient to capture rainfall jumps, and makes the PCA and cluster analysis more tractable computationally. In order to represent the full transition from boreal winter to boreal summer conditions, we use the 2279 available days between 25 January and 25 July for the TRMM years (1998-2010). These dates correspond with the northward rainfall progression, as defined by our Seasonal Position Index (SPI) described below. This time period includes 182 days in most years except for 1999 when data for 9 April are missing, and 2010 when data for June and July are not yet available.

Wind and geopotential height fields from the European Center for Medium-Range Weather Forecasts (ECMWF) reanalysis are used to examine dynamics associated with rainfall excursions ahead of and behind the mean seasonal cycle. Diro *et al.* (2010) show that the ECMWF reanalysis provides better rainfall estimates than the National Center for Environmental Prediction (NCEP) reanalysis, which is commonly used. Because the reanalysis must overlap with the period of the TRMM data, the ECMWF Interim Reanalysis is used [*Simmons et al.*, 2007]. The Interim Reanalysis is available for all days in the TRMM dataset, except during May, 2010,

which was not yet available online when this analysis was performed. The ECMWF model used in the Interim reanalysis is run at T159 resolution (approximately 1.125°) and the interim reanalysis product is available on a 1.5° x 1.5° degree grid.

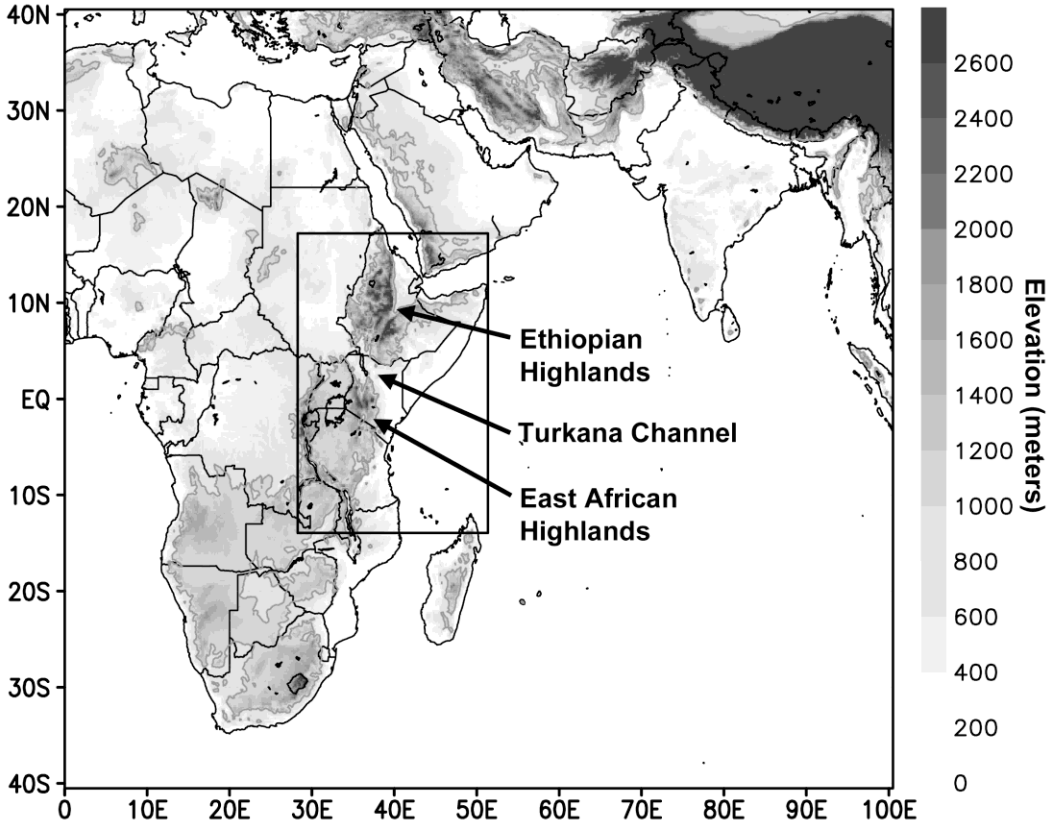

Figure 3.2: Topography over Africa and central Asia based on the NOAA GLOBE digital elevation model, displayed on a 10-minute grid. In addition to grid shading, the 1000-meter elevation contour is highlighted with a grey contour line. The domain used for our eastern African rainfall analysis is indicated by a black rectangle.

The domain chosen for the rainfall index development is shown as the solid rectangle in Figure 3.2, ranging from 28.5 E to 51.5 E and 14 S to 17 N. Using this domain, at 1° resolution, the spatial domain includes 713 (23 x 31) grid points. This domain covers the full range of the ITCZ migration over eastern Africa, including the Greater Horn of Africa (Ethiopia, Somalia, Eritrea, Djibouti and part of Sudan),

equatorial East Africa (Tanzania, Kenya, Uganda, and northern Mozambique) and parts of the western Indian Ocean. Topography is shown in Figure 3.2 with the Ethiopian Highlands, the Turkana Channel, and the East African highland regions indicated. The reanalysis is analyzed on the full domain shown in Figure 3.2 to provide a large-scale dynamical context for the rainfall variations.

3.3.2 The Seasonal Position Index (SPI)

The exact temporal and spatial characteristics of the ITCZ migration vary from one year to the next. The Seasonal Position Index (SPI) concisely captures important aspects of this seasonal progression, condensing the p = 713 spatial dimensions associated with a daily rainfall map to a single-valued index which varies only in time. Principal Component Analysis (PCA) is a common approach for reducing the dimensionality of a dataset by extracting only the most important patterns of variability. Since rainfall in the tropics is dominated by the north/south migration of the ITCZ, the leading principal components of our dataset capture variations associated with this seasonal cycle.

The SPI for a given day is calculated from the leading two elements of the principal component (PC) vector. The PC vector for a given day is calculated from the eigenvectors of the rainfall correlation matrix and then shifted to ensure that the origin is associated with a map of zero precipitation, a property which is required for calculating the SPI. The shifted PC vector for the i^{th} day, $\mathbf{u_i}$, is given by:

$$\mathbf{u}_\mathrm{i} = [E]^\mathrm{T}\mathbf{z}_\mathrm{i} - [E]^\mathrm{T}\mathbf{z}_0 \qquad (\mathbf{3.1.1})$$

where $[E]$ is the rotation matrix whose columns are eigenvectors of the 713 x 713 rainfall correlation matrix, and $\mathbf{z}$ and $\mathbf{z}_0$ are given by:

$$\mathbf{z}_i = [D]^{-1}(\mathbf{x}_i - \bar{\mathbf{x}}) \qquad (\mathbf{3.1.2})$$

and

$$\mathbf{z_0} = [D]^{-1}(\mathbf{0} - \bar{\mathbf{x}}) \qquad (\mathbf{3.1.3}).$$

In Eq. 3.1.2 and 3.1.3, $\mathbf{x_i}$ is the rainfall vector for the i^{th} day, $\bar{\mathbf{x}}$ is the mean rainfall vector averaged over all 2279 days, [D] is a diagonal matrix with rainfall standard deviations along the diagonal , and $\mathbf{0}$ is a zero-vector corresponding to a map of zero precipitation. Eq. 3.1 is equivalent to performing a PCA on the standardized rainfall vectors, rather than their standardized anomalies. This is a reasonable approach for precipitation data which are not symmetric around the mean. The magnitudes of the resulting shifted PC vectors, $\mathbf{u_i}$, represent a weighted sum of the total rainfall for the day, while the direction (phase) of the vectors give information about the spatial pattern of rainfall.

The SPI extracts phase information from the first two elements of $\mathbf{u_i}$, which define a plane in the original 713-dimensional space, and together capture most aspects of the seasonal cycle. The SPI for the i^{th} day is calculated as:

$$\mathrm{SPI}_i = \begin{cases} 2\pi - \cos^{-1}\left(\dfrac{-u(2)_i}{\sqrt{u(1)_i^{\,2} + u(2)_i^{\,2}}}\right) & \text{if} \quad u(1)_i > 0 \\ \cos^{-1}\left(\dfrac{-u(2)_i}{\sqrt{u(1)_i^{\,2} + u(2)_i^{\,2}}}\right) & \text{if} \quad u(1)_i < 0 \end{cases} \qquad (\mathbf{3.2})$$

where $u(1)_i$ and $u(2)_i$ are the first two elements of $\mathbf{u_i}$. Geometrically, the SPI is the angle, in a clockwise direction, between the vector [0 -1] and the vector $[u(1)_i\ u(2)_i]$. The angle is defined this way because it increases as the season progresses and avoids the discontinuity between 0 and 2π for our dataset. The structure of this index is

analogous to the MJO index calculated by *Wheeler and Hendon* [2004]. In addition to the phase information captured by the SPI, the magnitude of the vector $[u(1)_i\ u(2)_i]$ is also used in parts of our analysis.

3.3.3 The Rainfall Regime Index (RRI)

Like the SPI, the Rainfall Regime Index (RRI) is a single-valued time-varying index that captures important structures in the northward progression of eastern African rainfall. This second approach to reducing dimensionality describes the seasonal cycle as a progression through a series of common rainfall regimes, identified using a cluster analysis. Unlike previous cluster analyses for precipitation over Africa [e.g., *Pohl et al.*, 2005; *Franchereau et al.*, 2009] which assume seasonal stationarity, this cluster analysis explicitly includes the seasonal cycle. Rainfall on a given day is represented by a single number – the cluster number or RRI - which represents a typical stage in the seasonal progression. Rainfall jumps are captured in this framework as transitions between clusters. This method has the advantage of incorporating some higher order modes of seasonal variability compared to the SPI, and represents the seasonal cycle as inherently jumpy rather than smoothly varying.

The cluster analysis is performed on the first 30 elements of the shifted principal components (Eq. 3.1), which together account for 52.3% of the total variance in rainfall. By truncating the principal components, the computational time for the cluster analysis is reduced, and the cluster analysis focuses on large-scale rainfall patterns, rather than gridpoint-by-gridpoint variations. The results are not very sensitive to the number of principal components retained, as will be shown later in the results section.

The clustering is done with a k-means clustering algorithm based on a cosine distance measure. The k-means algorithm partitions the 2279 daily rainfall maps into

k groups, where the number of groups, *k*, is a specified fixed parameter. The algorithm seeks to find an optimal partition where members within each cluster are similar to each other, but well separated from members of other clusters. *Wilks* [2006a] and *Michelangeli et al.* [2005] among others provide detailed descriptions of the k-means clustering algorithm.

All clustering algorithms require a measure to quantify the similarity between two multi-dimensional vectors. Here, the similarity between two truncated PC vectors, $\mathbf{u}_n'$ and $\mathbf{u}_m'$, is measured using the cosine distance:

$$R_{n,m} = 1 - \cos\theta_{n,m} \qquad (\mathbf{3.3.1})$$

where:

$$\cos\theta_{n,m} = \frac{\mathbf{u}_n' \cdot \mathbf{u}_m'}{|\mathbf{u}_n'||\mathbf{u}_m'|}\,. \qquad (\mathbf{3.3.2})$$

Here, $\mathbf{u}_n$ and $\mathbf{u}_m$ are defined by Eq. 3.1, and the primes denote that $\mathbf{u_n}$ and $\mathbf{u_m}$ are truncated after the first 30 elements.

By using cosine distance, the clustering focuses on similarities and differences in spatial rainfall patterns, irrespective of their scaled intensities. One advantage of the cosine distance is that the resulting distributions around each cluster centroid are closer to multinormal than they would be using a more conventional distance measure (e.g., squared Euclidian distance). Clustering using cosine distance is similar to projecting the rainfall data onto a unit-hypersphere and clustering on the surface of that sphere. On this surface, the points are distributed relatively evenly around seasonal means. In contrast, the data points in Euclidian space are concentrated near the origin, not near seasonal mean values. As a result, clustering in Euclidian space

leads to a classification that puts all predominantly dry days in the same cluster irrespective of season.

The k-means algorithm requires initial guesses for the *k* cluster centroids. For this study, the initial guesses are obtained by first running the k-means algorithm on 10% of the data. This preliminary clustering is itself initialized by drawing *k* random seeds from the data subset. Even with this pre-clustering step, the final partition can still be sensitive to the initial seeds. Therefore, following previous authors [e.g., *Michelangeli*, 2005], we repeat the whole clustering process 50 times with different random seeds, and retain the partition having the highest mean similarity to the other 49.

For this study, the number of clusters, *k*, is chosen to be six. Choosing the number of clusters is a somewhat subjective process that depends both on the natural number of clusters inherent in the data, and on the approximate number of divisions in the data that is useful to the problem at hand. To determine the natural number of clusters, several authors have used a methodology based on calculating a "classifiability index" over a range of values for *k* and comparing it to a noise model [e.g., *Chen and Wallace*, 1993; *Michelangeli et al.,* 2005; *Pohl et al.*, 2005; *Franchereau et al.,* 2008].

We applied this methodology using three slightly different seasonal intervals (01 Feb – 31 Jul; 15 Jan – 13 Jul; and 29 Jan – 29 Jul), and found that the optimal value for *k* was different for each interval, making it difficult to choose the number of clusters based on this methodology alone. Our choice of six clusters was therefore determined subjectively after experimenting with a range of values for *k*. We find that six clusters concisely capture the important stages in the seasonal cycle. The resulting six cluster centroids emerge consistently for the three different seasonal intervals that we tested.

After applying the clustering algorithm, the cluster labels are reordered so that the median dates of cluster 1 - cluster 6 occur successively later in the season. This ensures that the RRI, which is equal to the cluster label for a given day, tends to increase as the season progresses.

3.3.4 Reconstructing Rainfall Maps from the Indices

We also work backwards from the index values to reconstruct full daily rainfall maps, and thus examine how well the indices capture important aspects of the daily rainfall patterns. For the SPI, the reconstructed rainfall vector, $\mathbf{x_i}$, is calculated by:

$$\mathbf{x_i} = \bar{\mathbf{x}} + [\mathrm{D}][E'](\mathbf{u''_i} + [E'']^T\mathbf{z}_0) \qquad (\mathbf{3.4})$$

where the symbols are defined as in Eq. 3.1, and double primes indicate truncation after the first two elements for $\mathbf{u''_i}$, and after the first two columns (eigenvectors) for $[E'']$. Negative values are set to zero after the reconstruction. By retaining the first two elements of $\mathbf{u_i}$ **,** this reconstruction makes use of both phase (SPI) and magnitude information from the first two principal components, thus approximating each 713-dimensional rainfall map from a two-valued characterization of rainfall for each day.

For the RRI, the reconstructed rainfall vector, $\mathbf{x}_\mathrm{i}$, is calculated by:

$$\mathbf{x}_\mathrm{i} = \mathrm{s_i}\,\mathbf{X}_{\mathrm{RRI(i)}} \qquad (\mathbf{3.5.1})$$

where RRI(i) is the cluster number assigned to the to the ith day, $\mathbf{X}_{1,2,..,6}$ are mean rainfall maps for each of the six clusters, and $\mathrm{s_i}$ is a scaling factor used to scale the centroid rainfall to match the domain-averaged rainfall magnitude for the ith day:

$$s_i = \frac{\langle x_i \rangle}{\langle X_{RRI(i)} \rangle}. \qquad (3.5.2)$$

The angle brackets indicate an area average over all 713 grid points in the domain. As with the SPI reconstruction, this reconstruction requires both the RRI, which gives information about the spatial pattern of rainfall, and a scaling factor, which encapsulates magnitude information. Again, approximations to the full rainfall maps are reconstructed from this 2-dimensional representation of the daily rainfall.

3.3.5 Correlating SPI and Circulation Field Anomalies

In the last section of our results, we calculate correlations between daily SPI anomalies and 850 hPa circulation anomaly fields, after first subtracting the seasonal cycle. The goal of these correlations is to examine how rainfall excursions ahead of or behind the mean seasonal cycle are connected with low-level circulation excursions. To calculate daily anomaly values, an unsmoothed 13-year average is used to represent the seasonal cycle for the SPI, and for three 850 hPa circulation fields (u-wind, v-wind and geopotential height) at each ECMWF grid cell over the region from 40.5 S to 40.5 N, and 0 E to 100.5 E. By leaving the 13-year averages unsmoothed, we avoid smoothing over real kinks in the underlying seasonal cycles. The noise remaining in the 13-year average may degrade the daily signal, but will not lead to spurious correlations between the anomaly fields as might occur if the seasonal cycle were over-smoothed. With the seasonal cycles removed, points having similar seasonal cycles will not show significant correlations unless they also show covariance at other timescales.

Spearman rank correlations are calculated between SPI anomalies and 850 hPa wind and height anomalies for March, April and May. These include a total of 33660

correlations (3740 grid points x 3 variables x 3 months). The Spearman rank correlation is used to accommodate any deviations from normality.

The statistical significance associated with each correlation value is determined by performing a moving-blocks bootstrap for the full SPI anomaly timeseries, with the blocklength, L, determined following *Wilks* [1997]. This procedure generates synthetic datasets that are uncorrelated with the circulation timeseries, but which capture the relatively complicated autocorrelation structure in the SPI timeseries. Days in March, April and May are then extracted from each of the 1000 synthetic datasets and used to generate null distributions of Spearman rank correlation values. A total of 33,660 null distributions are generated, one for each of the correlation values, and local p-values are calculated with respect to these null distributions.

Even in the null case of no underlying correlation between the SPI and any of the circulation points, a number of local tests will return nominally significant results due to the very large number of tests performed. We account for this by controlling the false discovery rate at 5%. Following the methodology laid out in *Wilks* [2006b], we regard as statistically significant only those correlations for which the p-value is smaller than:

$$p_{thres} = \max_{j=1,\ldots K} \left[p_j : p_j \leq q\left(\frac{j}{K}\right) \right] \qquad (\mathbf{3.6})$$

where q = 0.05 is the desired false discovery rate, and p_j is the j^{th} smallest of the K=33,660 local p-values.

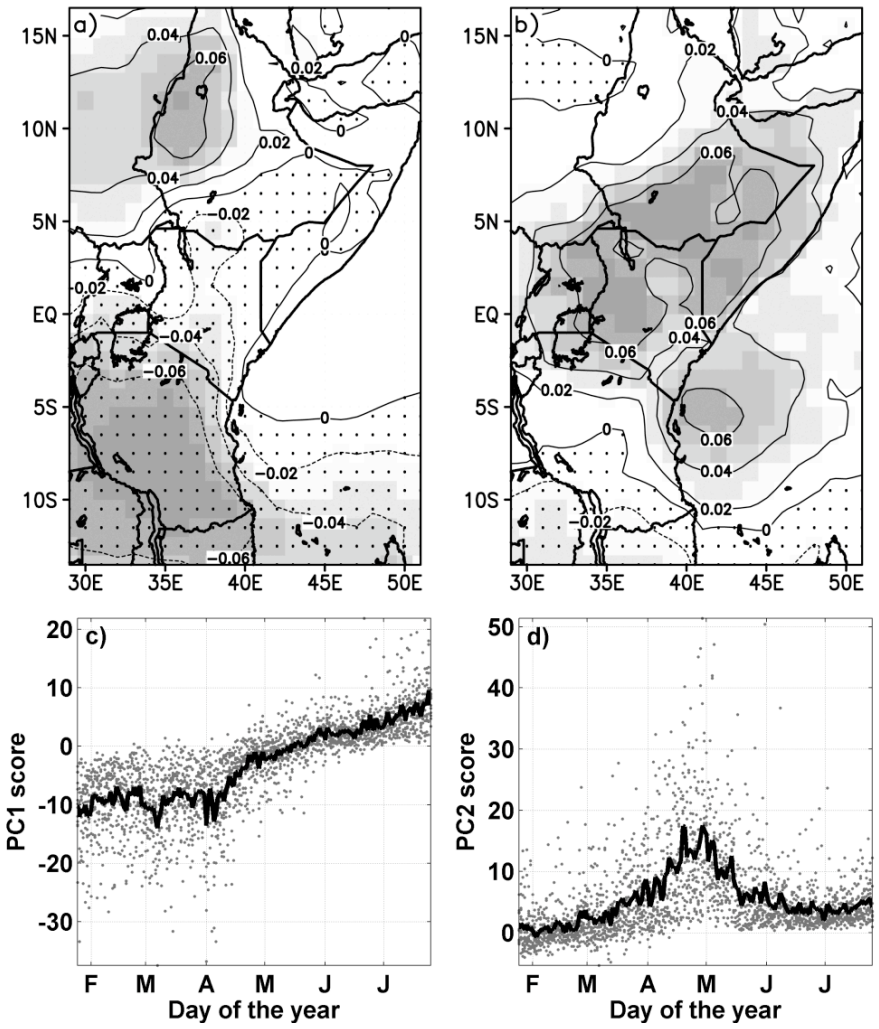

Figure 3.3: **(a)** Map showing the eigenvector associated with the leading principal component in a PCA of TRMM rainfall from late-January through late-July. Shading corresponds to the magnitude of the eigenvector elements, and several contours are provided for scale. Stippled regions represent negative values. **(b)** Same as (a) but for the second principal component. Both eigenvectors are scaled to have unit length. **(c)** PC1 scores plotted verses the day of the year (grey dots), and their mean seasonal cycle (black solid line). **(d)** Same as (c) but for PC2.

3.4 Results

3.4.1 The Principal Component Analysis

Figure 3.3 shows the first two eigenvectors of the principal component analysis (PCA), as well as the seasonal cycle of associated principal component (PC) scores.

The two leading eigenvalues are well separated from each other (with respect to their 99% confidence intervals), and are also very well separated from all smaller eigenvalues, suggesting that the first two eigenvectors in Figure 3.3 are not sensitive to sampling errors. These two leading patterns account for 8.1% and 6.3% of the total variance, respectively. Because daily rainfall events are often localized, much of the rainfall variance remains at smaller spatial scales. Nonetheless, PC1 and PC2 capture important aspects of the regional-scale variability.

The PC scores plotted in Figure 3.3c and 3.3d are projections of daily rainfall fields onto the eigenvectors of PC1 and PC2, respectively. These scores, which exhibit strong seasonal cycles, are used to calculate the SPI. Other PC's, particularly PC3 (3.7% of the variance) and PC6 (2.3% of the variance), also exhibit seasonal signals (not shown), but represent substantially less variance than the two leading modes. Together PC1 and PC2 describe the north/south position of rainfall. Rainfall is strongest below the equator when PC1 scores are negative (winter) and strongest over the Ethiopian highlands when PC1 scores are positive (summer). Rainfall is strongest in an intermediate position, near the equator, when PC2 scores are positive, and PC1 scores are weak (spring).

The SPI for a given day is calculated by projecting a daily rainfall map onto the plane spanned by these first two principal components, and calculating the phase (Eq. 3.4). Figure 3.4 shows all 2279 points in the rainfall dataset plotted in PC1- PC2 space, with predominantly dry days clustered near the origin. Points in this plane can be viewed in polar coordinates as having a magnitude (related to the intensity of rainfall), and a phase (associated with a position along the seasonal cycle – the "seasonal position"). To demonstrate this, PC's associated with mean monthly rainfall maps are plotted on Figure 3.4 as black x's, and the distribution of phases experienced during each month are circumscribed with arcs. The solid lines and arcs in Figure 3.4

show that the seasonal evolution from winter to summer typically follows a clockwise progression around the origin (increasing SPI), but with relatively large variability within each month. The SPI is measured as the clockwise angle around the circle, with zero phase at "six o'clock".

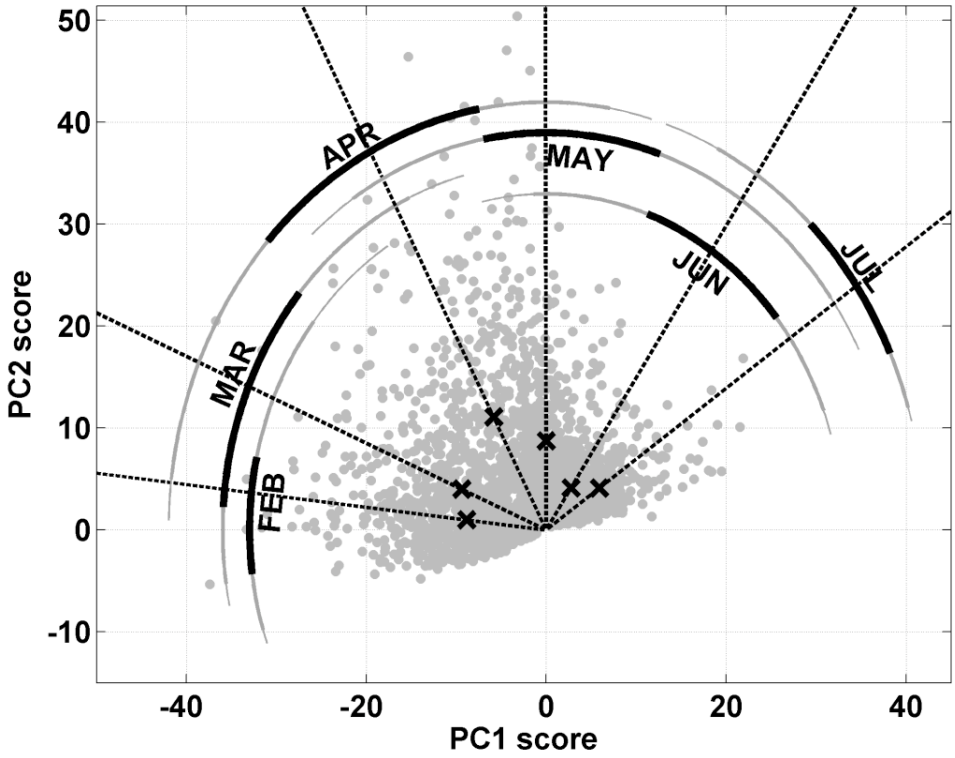

Figure 3.4: PC1 and PC2 scores for all 2278 days in the rainfall dataset (grey dots), as well as PC1 and PC2 scores associated with monthly mean rainfall maps for February through July (black x's). January is not shown since only the last seven days of January are included in the dataset. Arcs for each month (February – July) show the distribution of phases experienced during that month. Black arcs show the central 50% of the distribution, while grey arcs show the central 95%.

3.4.2 The Cluster Analysis

Results of the cluster analysis are shown in Figure 3.5. Mean rainfall maps for each of the six clusters are calculated by averaging rainfall maps from all days falling in a given cluster. These mean maps are shown in Figure 3.5a – 3.5f, and histograms showing the seasonal distribution of days in each cluster are shown in Figure 3.5g–

3.5l. Clusters are ordered by their median dates, which are also show on the plot. The RRI value for a given day is the cluster number for that day.

We tested the sensitivity of these results to the number of PC's retained. When comparing the results shown in Figure 3.5 (a-f) to results from a cluster analysis on the original data with no truncation, we find that pattern correlations are 0.997, 0.998, 0.999, 0.997, 0.993, and 0.995 for the six cluster centroids, respectively. Ninety-five percent of the days are classified into the same clusters using the two methods.

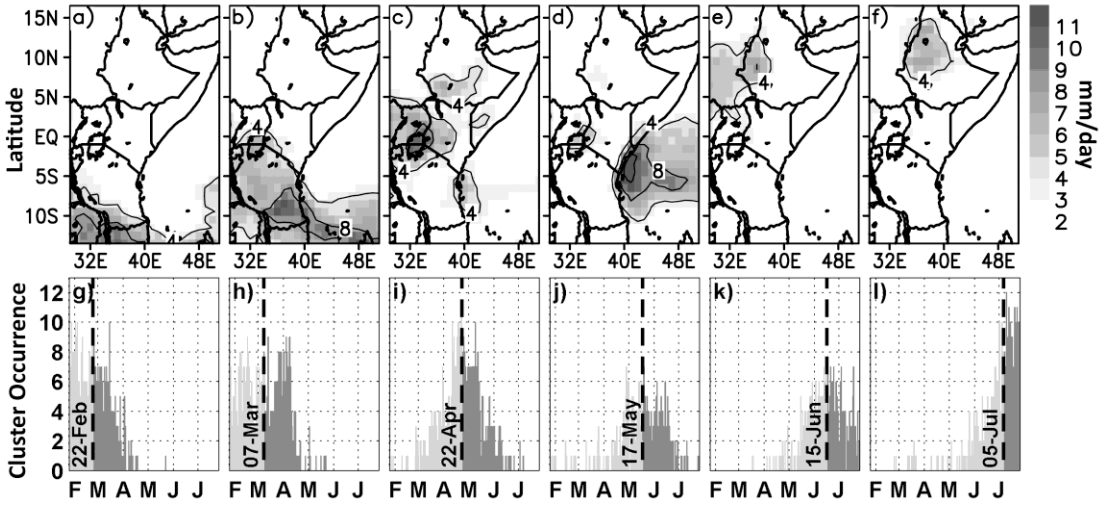

Figure 3.5: (a) Cluster 1 mean rainfall map, based on a k-means cluster analysis of TRMM daily rainfall. Shading shows the cluster mean rainfall rate in mm/day. Contour lines are displayed for 4 mm/day, 8 mm/day and 12 mm/day. **(b-f)** Same as (a), except for cluster 2 through cluster 6, respectively. **(g)** Histogram showing the seasonal distribution of cluster 1 in units of cluster occurrences per day of the year. The median date for cluster 1 is indicated by the black dotted line. Days in cluster 1 that occur on or before the median date are shown in light grey, while days in cluster 1 that occur after the median date are shown in dark grey. **(h-l)** Same as (g), except for cluster 2 through cluster 6, respectively.

In general, cluster rainfall moves from south to north as the median date increases. The exception to this pattern is cluster 4, which describes heavy rainfall just off the coast of Kenya and is centered further south than cluster 3. Cluster 4 is also unique from the other clusters in that it is common only during the northward rainfall

progression, and not during the reverse migration in September through November (not shown).

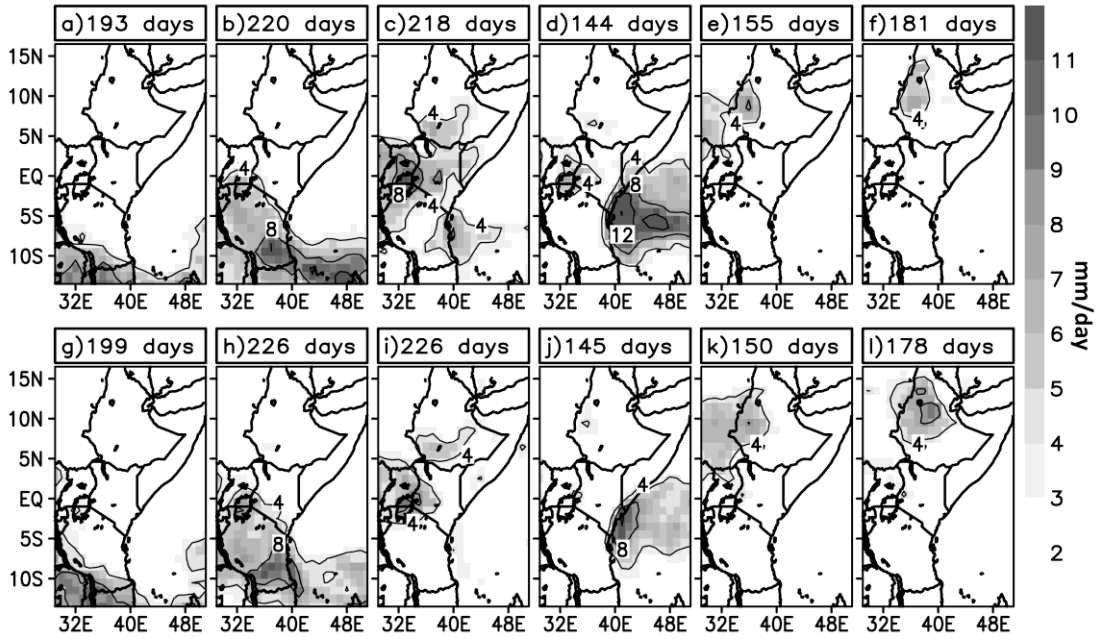

Figure 3.6: (a) Composite rainfall map for "early" days in cluster 1. Early days are defined as days in cluster 1 that occur earlier in the season than the median date for the cluster (indicated in Figure 3.5). The number of days composited in (a) is indicated in the plot label. **(b-f)** Same as (a), except for clusters 2-6, respectively. **(g)** Composite rainfall map for "late" days in cluster 1. Late days are defined as days in cluster 1 that occur later in the season than the median date for the cluster. The number of days composited is indicated in the label. **(h-l)** Same as (g), except for clusters 2-6, respectively. Cluster occurrences on the median date, are not included in either the "early" or the "late" composites.

Figure 3.6 shows composite maps for the same six clusters but divided into "early" and "late" groups according to whether the days fall before or after the median date for the cluster. The numbers of days that fall into each of these categories are also noted on the plot. The similarity of early and late maps for each cluster suggests that the clusters are adequately separated from each other and the clustering supersedes seasonality as an organizing structure. If the seasonal cycle were smooth rather than

jumpy, "early" and "late" composites would fall between the mean cluster maps in Figure 3.5.

Finally, Table 3.1 shows transition probabilities among the six clusters, with highlighted and bold entries representing higher transition probabilities (see Table 3.1 caption). As expected, the highest probabilities are on the diagonal, indicating that rainfall patterns generally remain within the same cluster for multiple consecutive days. The most common transitions between clusters occur between cluster 5 and cluster 6, suggesting that summer rainfall patterns transition frequently back and forth between these two clusters. Transitions between the two winter clusters (Clusters 1 and 2) are the next most common. Other adjacent clusters also show relatively high transition probabilities.

Table 3.1: Cluster transition probabilities, measured as a percent of the total cluster occurrence. For example, if a given day in the dataset is classified as cluster 4, then 14.1% of the following days are in cluster 5. Highlighted, bold numbers are transitions where the conditional transition probability is greater than twice unconditional probability of a day residing in a given cluster. Unhighlighted, bold numbers are transitions where the conditional probability is comparable to the unconditional probability of being in that cluster. Light grey numbers represent comparatively unlikely transitions.

Cluster Number	#	1	2	3	4	5	6
1	401	**67.8**	**23.4**	3.7	2.7	0.5	1.7
2	453	**20.8**	**64.0**	12.8	1.5	0.7	0
3	455	3.5	10.8	**64.4**	**12.5**	6.6	2.2
4	291	1.7	3.8	**17.2**	**55.5**	**14.1**	7.6
5	312	0.3	1.0	9.4	9.3	**38.4**	**41.6**
6	367	1.4	0	2.8	7.3	**32.8**	**55.5**
Any (Unconditional)	2279	17.6	19.9	20.0	12.8	13.7	16.1

The notable exception is for transitions between cluster 2 and cluster 3, where the conditional transition probabilities are less than half the overall (unconditional) probabilities of residing in these clusters. These transitions occur only 5-6 times a year on average - less frequently than transitions between other adjacent clusters. This transition is of particular interest because it is associated with jumps into the northern hemisphere.

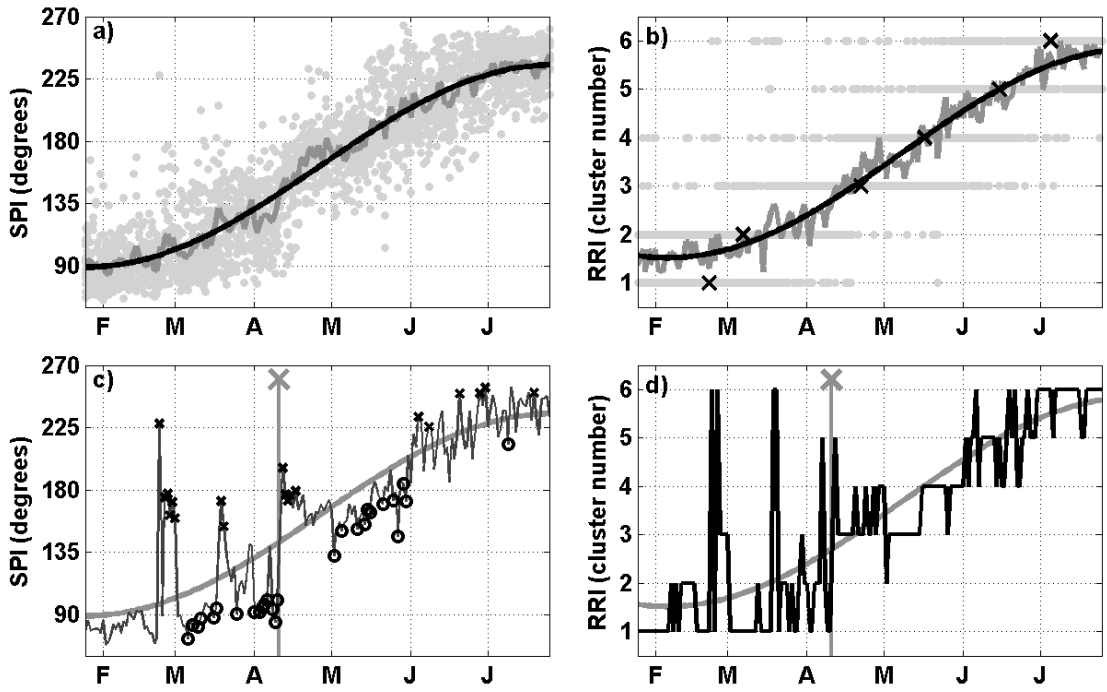

Figure 3.7: (a) The SPI for all 2279 daily rainfall points plotted versus the day of the year (grey dots), with the climatological mean SPI (grey line), and a fitted sine curve with the period constrained at 365 days (black line). Units are in degrees clockwise from the [0, -1] vector in PC1-PC 2 space. **(b)** Same as (a), except for the RRI. Median dates for each cluster are marked with black x's. **(c)** The SPI for 2003 (black line) with days that are more than one standard deviation above the mean marked with x's, and days that are more than one standard deviation below the mean marked with o's. An average standard deviation (over all 182 days of the year) is used for these classifications. The fitted sine curve from (a) is reproduced for comparison (dark grey line). The 2003 jump date from Figure 3.1 is noted as a grey vertical line marked with large grey "x" at top. **(d)** The RRI for 2003, with the sine curve from (b) reproduced as a dark grey line. As in (c), the 2003 jump date is marked with a grey vertical line and 'x' at top.

3.4.3 Index Representations of the Seasonal Rainfall Cycle

The top two panels of Figure 3.7 examine how the SPI and RRI represent the seasonal cycle of rainfall. The most important difference between the two indices is that the SPI is continuous, while the RRI is discrete. Otherwise, their seasonal cycles (Figures 3.7a and 3.7b) both generally increase between 25 January and 25 July, with their climatological means resembling a sinusoid with a 365-day period (though the data could also be fit well by other functions). The largest SPI deviations from the sinusoid occur in April when the mean SPI slope is particularly steep, possibly due to latitude jumps occurring during this period. Both indices can be used to determine if rainfall on a given day is "ahead of" or "behind" the seasonal mean. Grey dots above the solid lines represent days with seasonally advanced rainfall, whereas grey dots below the solid lines represent seasonally delayed rainfall.

The bottom two panels of Figure 3.7 examine how the two indices represent rainfall jumps in 2003. The year 2003 was chosen as a case study because the main rainfall jump across the equator is abrupt, and several other interesting transitions occur later in the season. Recall from Figure 3.1 that a distinct northward jump in the latitude of rainfall is apparent in 2003 on 11 April. This northward jump is followed by an anomalous southward excursion to 5° S, beginning on approximately 14 May, and a subsequent return northward to 10° N at the beginning of June (Figure 3.1b).

The large northward jump on 11 April is observable in both index representations, but is particularly clear in the SPI plot (Figure 3.7c). The SPI jumps between approximately 90 degrees on 10 April to approximately 180 degrees on 11 April, with this transition marked with a vertical dotted line. In the days before the jump, the SPI values are smaller than typical (marked with o's), while the days following the "jump" are larger than typical (marked with x's). For the RRI (Figure 3.7d), a one-day jump between cluster 1 (on 10 April), and cluster 5 (on 11 April) is

observed. In addition, a semi-permanent transition between the winter clusters (clusters 1 and 2) and the spring clusters (clusters 3 and 4) occurs at this time.

The late-season excursions in May and June 2003 are also apparent in the SPI and RRI representations. Both indices are smaller than typical in May, before returning to normal at the beginning of June. However, neither index captures the abruptness, timing, or magnitude of the southward excursion that occurs in the Figure 3.1 between 14 May and 01 June. A closer look reveals that the southward excursion in Figure 3.1 is associated with an offshore rainfall pattern resembling Cluster 4 (Figure 3.5d). Though south of the equator, this pattern is not a return to a typical early season (February/March) rainfall pattern, but rather a relatively common rainfall pattern in May. This explains why the SPI and RRI both increase throughout the month of May, despite the latitude of rainfall dipping well south of the equator starting on 14 May. In this sense, the SPI and RRI capture the true underlying seasonal cycle better than a purely latitude-based rainfall index, which ignores longitude information.

Figure 3.8 shows several Hovmöller diagrams for 2003, comparing zonal rainfall averages from the original full-dimensional TRMM dataset to similar averages from datasets reconstructed from the SPI and RRI, using Eq. 3.4 and Eq. 3.5, respectively. Except for the absence of fine-resolution details, many important aspects of the latitude jumps in Figure 3.8a are retained in the lower dimensional representations (Figures 3.8b and 3.8c).

The abrupt northward transition on 11 April is very apparent and quite realistic in both the SPI and RRI reconstructions, despite being comparatively difficult to identify in the previous RRI plot (Figure 3.7d). A large latitude difference between the winter clusters (1 and 2), and cluster 3 (see Figure 3.5) accounts for the prominent jump in the RRI reconstruction (Figure 3.8c). While transitions to cluster 3 (and clusters 5 and 6) occur earlier in the season (late February and March), these

transitions are temporary and generally occur on days with relatively light rainfall. A more permanent transition to cluster 3 does not occur until 11 April. Thus, rainfall jumps into the northern hemisphere can be associated with semi-permanent transitions from the winter clusters (1 and 2) into cluster 3.

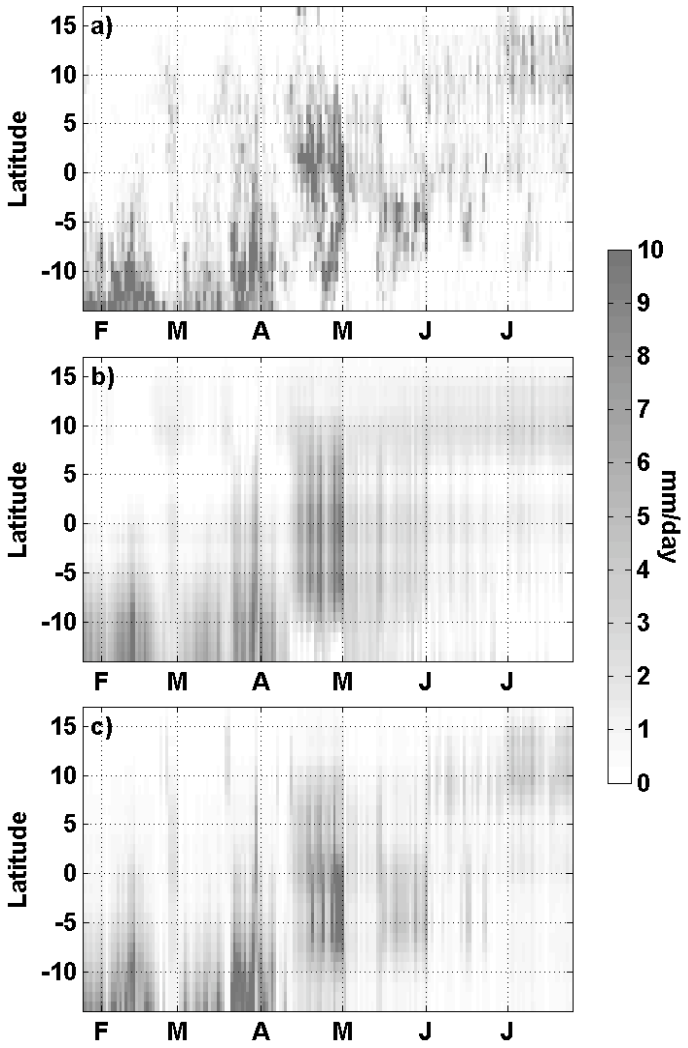

Figure 3.8: (a) Hovmöller diagram of TRMM rainfall data for 2003 averaged over 27.5° – 52.5° E longitude. This is the same as Figure 3.1b, except that the data are displayed at 1.0 degree latitude increments and truncated to the study dates (25 January through 25 July). **(b)** Reconstructed Hovmöller diagram based on the first two principal components retained in the SPI. **(c)** Reconstructed Hovmöller diagram based on the RRI and domain-averaged rainfall for each day in 2003. Detailed descriptions of these reconstructions are provided in the text.

In late May, the rainfall maximum near 5° S is poorly resolved in the SPI reconstruction (Figure 3.8b), but captured better in the RRI reconstruction (Figure 3.8c). This difference can be explained by the fact that more PC's are retained in the RRI representation, allowing it to better resolve the rainfall maximum off the coast of Kenya.

In general, these results suggest that rainfall jumps are captured well by the SPI and RRI for 2003. The RRI has the advantage of providing a more accurate reconstruction of rainfall than the SPI because it retains more principal components. The RRI also explicitly defines the jump into the northern hemisphere as the transition between the wintertime clusters (1 and 2), and cluster 3. In contrast, the SPI has the advantage of being a continuous index. In 2003, the latitude jumps are prominent and approximate jump dates can be determined by inspection of the rainfall data. In other years, however, the date of a jump is not as easy to define and the SPI provides a simple means to quantify leads ahead of or lags behind the mean climatology. Because one is discrete and the other continuous, the two indices complement each other and lend themselves to different applications.

3.4.4 Interannual Variability in Rainfall Jumps

As mentioned previously, rainfall jumps over eastern Africa vary from one year to the next. In some years, the latitude of rainfall jumps across the equator only once, while in other years multiple jumps are observed. Temporary excursions into the northern hemisphere are common in February and March before a more permanent jump occurs later in the season. Jumps also range in character from very abrupt to comparatively smooth.

The RRI and SPI provide means to characterize year-to-year differences in both the timing and character of the jumps. The two indices are used here to calculate

approximate dates for jumps into the northern hemisphere for the thirteen years of the TRMM dataset. Then, because a main jump is not always easy to identify, the indices are used to calculate a measure of jump clarity. On years when the clarity of the jump is low, the jump date will be less useful than in years when the clarity is high. Results are compared between the two indices.

The algorithm used to calculate the jump dates follows that used by Camberlin and *Okoola* [2003] to calculate the onset and cessation dates of the long rains over Kenya, Uganda and N. Tanzania. *Camberlin and Okoola* [2003] calculate the monsoon onset date as the date associated with the minimum of the integral of their rainfall index. For an increasing index that crosses zero, this algorithm finds the zero-crossing that is most associated with a permanent index shift from negative to positive.

In order to apply this algorithm, the SPI and RRI must first be calibrated so that the zero-point is associated with the rainfall jump across the equator. For the RRI, the analysis in section 3.5.2 concluded that the jump occurs as a transition between clusters 2 and 3. Therefore, a value of -1 is assigned to days in clusters 1 and 2, and a value of +1 to days in clusters 3-6. This modified index crosses zero during the desired cluster transitions. Using this methodology, jump dates derived from the RRI range from 24 March to 16 April. The mean jump date is on 6 April, and the median date is on 10 April.

Defining the zero-crossing of the SPI is somewhat less straightforward. Assuming that the median jump timing is captured correctly using the RRI, we adjust the SPI in order to artificially set the zero-crossing of the 13-year SPI mean (grey line in Figure 3.7a) to occur on 10 April, the median RRI jump date. This requires subtracting 138º from each SPI value. The resulting SPI-derived jump dates range from 4 April to 17 April, with median and mean jump dates both occurring on 10 April. A quick sensitivity study shows that the jump dates are relatively insensitive to

the exact number of degrees subtracted. For degree shifts between 134º and 144º, the median jump date remains constant and the mean jump date differs by only two days. The fact that the SPI and RRI methods arrive at the same median date is not surprising, since the two methods are tuned to have their zero-crossings occur at a similar time. On the other hand, year-to-year variability in jump dates is derived independently.

The "clarity" of the jump in a given year is determined by how well the jump date partitions the indices into positive and negative values. In a year with a single clear jump, an index will remain negative until the jump date, and remain positive afterwards. In a more complicated year with several jumps, several positive index values will occur before the jump and/or several negative index values will occur afterwards. The total number of "misfit" values in March - May in a given year is used as a measure the jump clarity, with low values representing high clarity.

Tables 3.2 and 3.3 summarize the jump date and jump clarity results from the SPI and RRI, respectively. The RRI-derived and SPI-derived jump dates are within one day of each other in nine out of the thirteen years. However, the remaining four years can differ significantly, with the RRI jump dates earlier than the SPI dates by as much as two weeks in 2008. All of these non-fit years are identified as either "low" or "medium" clarity, suggesting that the jump is more complicated in these years. Figure 3.9 shows the jump dates marked on Hovmöller diagrams for 1998-2002 and 2004-2010. A similar Hovmöller diagram is shown for 2003 in Figure 3.8b.

In addition to jump dates and jump clarity information, Tables 3.2 and 3.3 include information about raw monthly SPI and RRI anomalies averaged for the months of March, April and May. These anomalies are included to make a connection between differences in the timing and character of rainfall jumps, and daily index anomalies which will be used in next section to examine associated circulation patterns.

Table 3.2: Summary information for jumps in 1998 – 2008 based on the SPI. Algorithms for calculating the jump date and jump clarity index are described in the text. Jump dates that are the within a day of the RRI-derived jump dates are in bold. "Days early or late" are in comparison to the median jump date of 10 April. For the jump clarity index, the "Med" classification is given for standardized anomalies between -0.5 and 0.5. "Very High" and "Very Low" classifications are given for standardized anomalies >1.5 and <-1.5, respectively. In the monthly "SPI anomaly" columns, "N" and "S" refer to positive and negative anomalies in the monthly-averaged SPI. "NN" ("SS") indicate anomalies which are more than one standard deviation above (below) the mean.

Year	SPI-Derived Jump Date	Days Early or Late	Jump Clarity (SPI)	SPI Anomaly		
				March	April	May
1998	17 April	**+7**	**Low**	N	S	S
1999	**14 April**	+4	Low	N	S	**NN**
2000	**12 April**	+2	**High**	**SS**	N	**NN**
2001	**4 April**	**-6**	Low	**NN**	N	N
2002	**9 April**	-1	High	S	N	N
2003	**11 April**	+1	High	S	S	**SS**
2004	4 April	**-6**	Med	S	**NN**	N
2005	**5 April**	**-5**	**Low**	**NN**	N	S
2006	**17 April**	**+7**	Med	S	**SS**	S
2007	**11 April**	+1	Med	N	**SS**	S
2008	8 April	-2	Med	S	NN	S
2009	**10 April**	0	High	SS	S	**SS**
2010	10 April	0	Med	N	N	n/a

Table 3.3: Same as Table 2, except for the RRI, with jump dates that are within a day of the SPI-derived jump dates in bold.

Year	RRI-Derived Jump Date	Days Early or Late	Jump Clarity (RRI)	RRI Anomaly		
				March	April	May
1998	10 April	0	Low	N	N	N
1999	**14 April**	+3	Low	N	S	**NN**
2000	**12 April**	+2	**High**	**SS**	**NN**	**NN**
2001	**4 April**	**-6**	Low	N	S	N
2002	**9 April**	-1	High	S	N	N
2003	**11 April**	+1	High	**SS**	S	**SS**
2004	24 March	**-17**	Med	N	S	N
2005	**5 April**	**-5**	Low	**NN**	S	**SS**
2006	**16 April**	**+6**	Low	N	**SS**	S
2007	**11 April**	+1	Med	N	S	**SS**
2008	25 March	**-16**	Med	S	NN	S
2009	**10 April**	0	High	**SS**	S	**SS**
2010	28 March	**-13**	Med	N	**NN**	**SS**

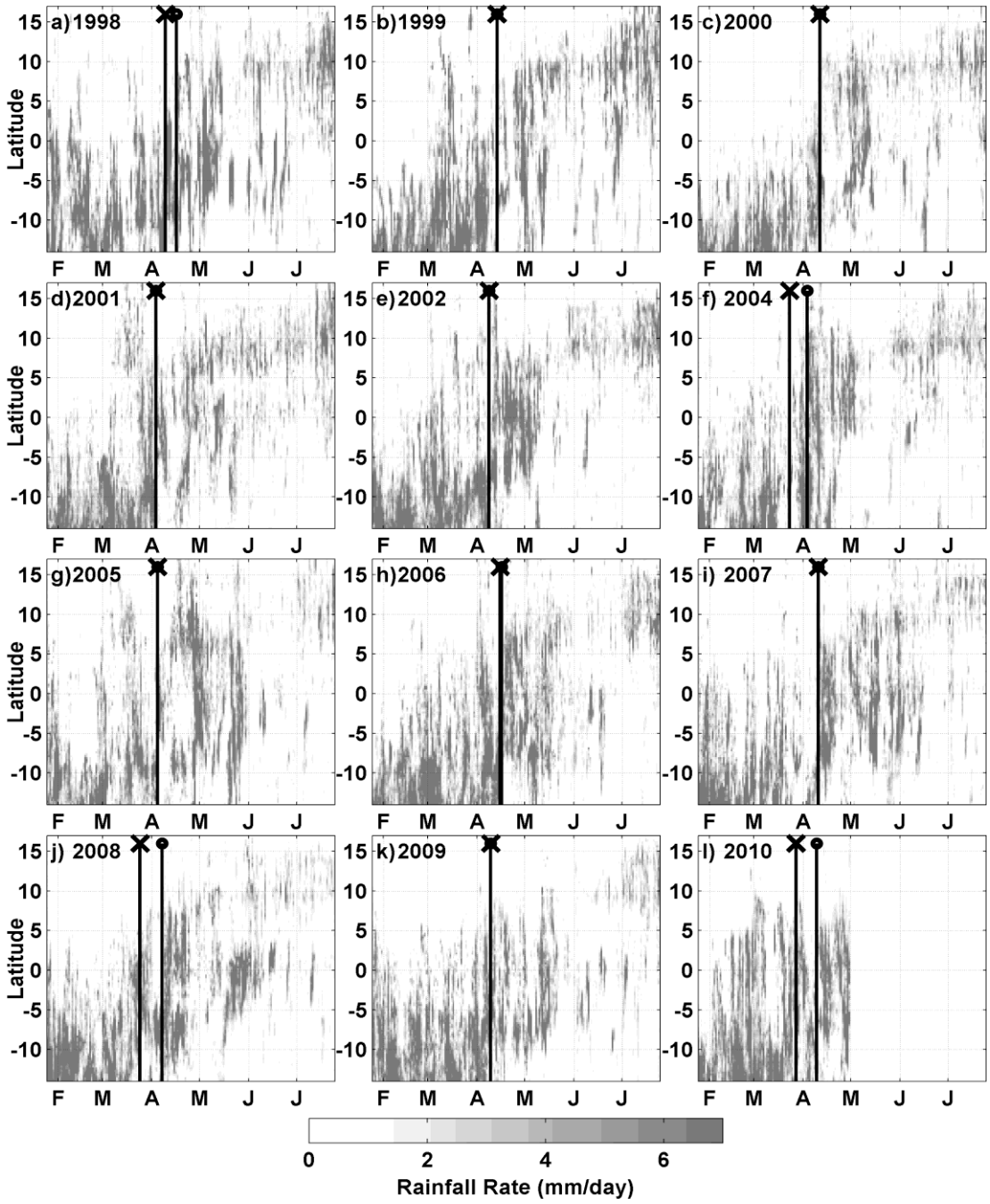

Figure 3.9: Hovmöller diagrams for 1998-2010, skipping 2003 because these data were already presented in Figures 3.1 and 3.8. SPI and RRI-derived jump dates are indicated with vertical black lines and symbols on top. The SPI-derived date is marked with an "x" and the RRI-derived date is marked with an "o". The two symbols are superimposed when the date is the same.

The monthly anomalies are not well correlated between the months of March, April and May, suggesting that deviations ahead or behind the seasonal cycle do not generally persist throughout the full MAM season. In addition, index anomalies in April are closely related to the jump timing, especially when using the SPI index. With a few exceptions (1998, 2000, and 2009), a higher (lower) than usual SPI in April is associated with an earlier (later) than usual jump. For the three exception years, the jump dates are either equal to or within a few days of the average. Finally, years with low jump clarity are all associated with northward index anomalies in March, as expressed by temporary early jumps north of the equator. These early excursions, which are associated with the March *belg* rains in Ethiopia are quite variable from one year to the next.

3.4.5 Dynamics Associated with Excursions from the Seasonal Cycle

Riddle and Cook [2008] hypothesized a connection between rainfall jumps over eastern Africa and stages in the development of the Somali Jet. Their hypothesis is as follows. Prior to the onset of the Indian summer monsoon (in late April and early May), a narrow cross-equatorial jet forms along the coast of eastern Africa. Unlike the fully formed Somali Jet, this "nascent" Somali Jet lacks a zonal branch across the Arabian Sea. Instead, it carries moisture from the southern Indian Ocean across the equator into southern Ethiopia. *Riddle and Cook* [2008] hypothesize that the formation of this nascent Somali Jet, and the associated cross-equatorial moisture transport, is associated with a northward jump in precipitation from the southern into the northern hemisphere. Later, in late May and June, this moisture source is removed as the Arabian Sea branch of the jet forms and carries the moisture across the Arabian Sea towards India. A new moisture source from the west fuels the Ethiopian summer rainy season.

Figure 3.10 (a-c) shows 850 hPa wind and climatological geopotential height fields for March, April and May. The cross-equatorial nascent jet is not yet present in March, but can be identified in the April average, and a full Somali Jet, including the Arabian Sea branch, can be observed in May. While the nascent jet is present in the April average, the equatorial wind direction changes considerably between early and late April as the nascent jet forms (not shown). In early April, climatological winds at the equator are primarily easterly or southeasterly near East African coast, while late in the month and in early May a clear southerly nascent jet is present along the coastline.

Riddle and Cook [2008] showed that the timing of the rainfall jump into the northern hemisphere is roughly coincident with the formation of the nascent Somali Jet both in the climatology and in regional model simulations of 2002 and 2003. However, they did not test this connection more generally over a range of years. One way to go about testing this connection is to use the SPI to measure excursions ahead of and behind the mean seasonal precipitation cycle and examine correlations with the development of the Somali Jet.

Figure 3.10 (d-l) shows correlations between SPI and circulation anomaly fields using the methodology described in Section 3.4.4. For the moving-block bootstrap, L, the block length, is equal to 119 elements, based on Eq. 19 in *Wilks* [1997]. The threshold p-value in Eq. 3.6 that controls the false discovery rate at 5% is found to be 0.0017, and thus only local tests with significance levels greater than 99.83% are shown on Figure 3.10. Since the ECMWF reanalysis does not assimilate precipitation, the TRMM-based SPI and the ECMWF circulation fields are based on independent observations and not inherently related.

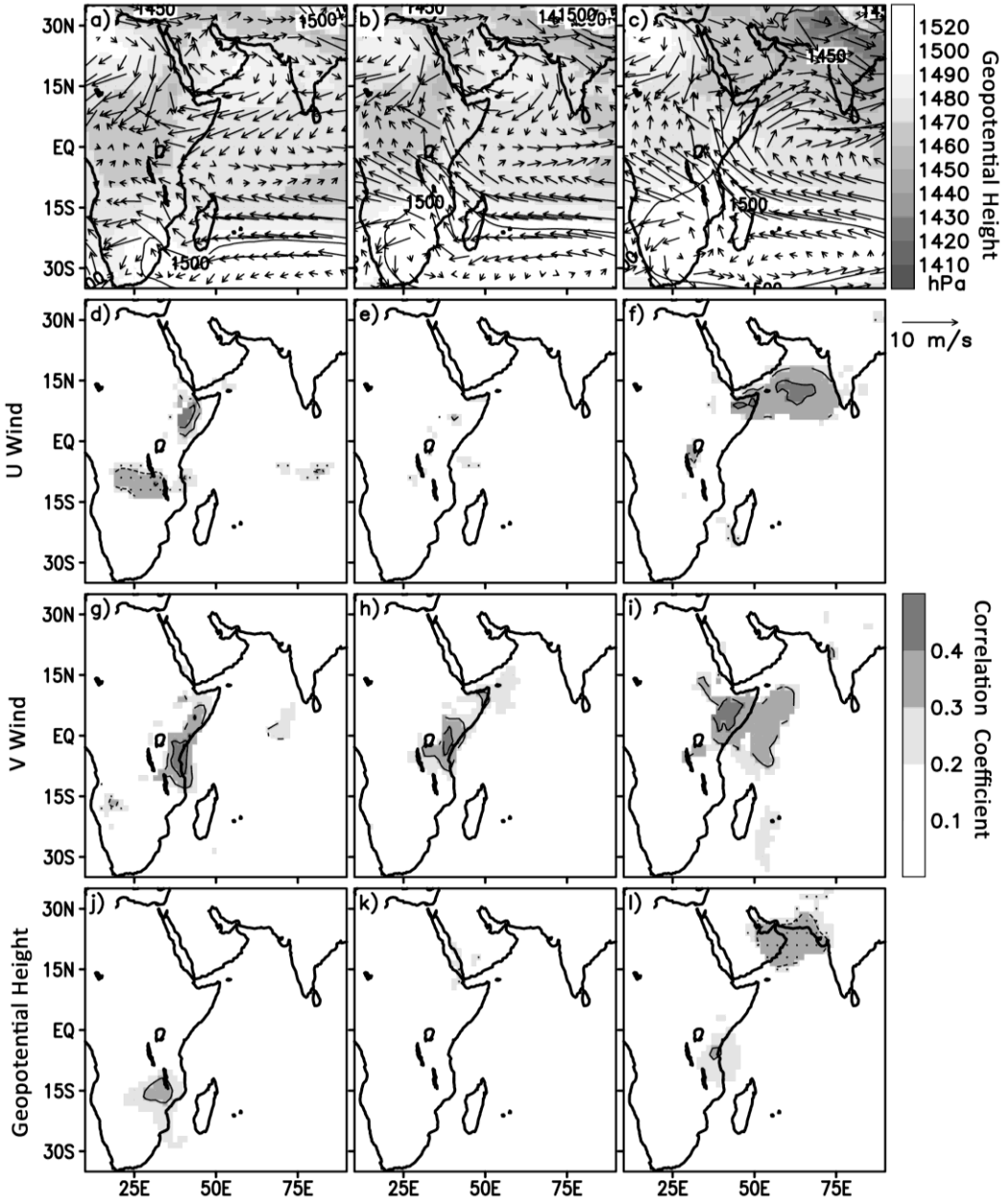

Figure 3.10: (a-c) 850 hPa geopotential heights and winds for March, April and May. The "nascent" Somali Jet is present in **(b)**, whereas the fully formed Somali Jet is present in **(c). (d-f)** Correlations between SPI anomalies and 850 hPa zonal wind anomalies for March, April and May. The mean seasonal cycle is removed from the SPI and from each grid point. Only points with local significance values greater than 99.85% are shown, controlling the false discovery rate at 5%. Negative correlations are indicated by stippling. **(g-i)** Same as for (d-f), but for meridional wind anomalies. **(j-l)** Same as (d-f), but for geopotential height anomalies.

We are particularly interested in SPI anomalies that occur during April since rainfall jumps into the northern hemisphere typically occur in April. Excursions in the SPI ahead of or behind the mean seasonal progression during the month of April are likely to be associated with early or late rainfall jumps (e.g., Figure 3.7c). The strongest correlations for the month of April are observed between the SPI anomalies and anomalies in the meridional wind (Figure 3.10h) near the equatorial east African coast, in the region of the nascent Somali Jet. Southerly cross-equatorial anomalies are positively correlated with northern rainfall anomalies. The maximum correlations in the jet region are 0.423, and have local significance levels of at least 99.93%. Similarly, strong correlations are not observed between SPI anomalies and 500 hPa meridional winds (not shown), suggesting that the correlations only hold with near-surface winds.

The nascent jet is generally not yet present in March. However, correlations between SPI anomalies and cross-equatorial wind anomalies are already significant in March. These correlations suggest that meridional winds in the jet region may be associated with the seasonal evolution of rainfall even before the formation of the nascent Somali Jet. Also in March, significant positive correlations are observed between SPI anomalies and easterly flow over southern equatorial Africa. Positive height anomalies over southeastern Africa are also significantly associated with positive SPI anomalies.

In May, the strongest correlations are observed between SPI anomalies and zonal wind anomalies over the Arabian Sea in the region of the zonal arm of the Somali Jet. In addition, strong correlations are observed with meridional winds over Somalia and extending off the coast into the western Indian Oceans. Significant correlation values ($r > 0.3$; $p < 0.0017$) are also observed between SPI anomalies and geopotential height anomalies over the northern Arabian Sea. These correlations are

all consistent with earlier-than-usual developments in the formation of the Somali Jet, including the development of a zonal branch across the Arabian Sea and widening and strengthening of the equatorial branch.

The correlations observed in Figure 3.10 are consistent with the hypothesis of Riddle and Cook (2008), and show that the seasonal evolution of the Indian monsoon circulation – including the development of the Somali Jet – is connected at a daily to intraseasonal timescale to the timing of the evolution of rainfall over eastern Africa.

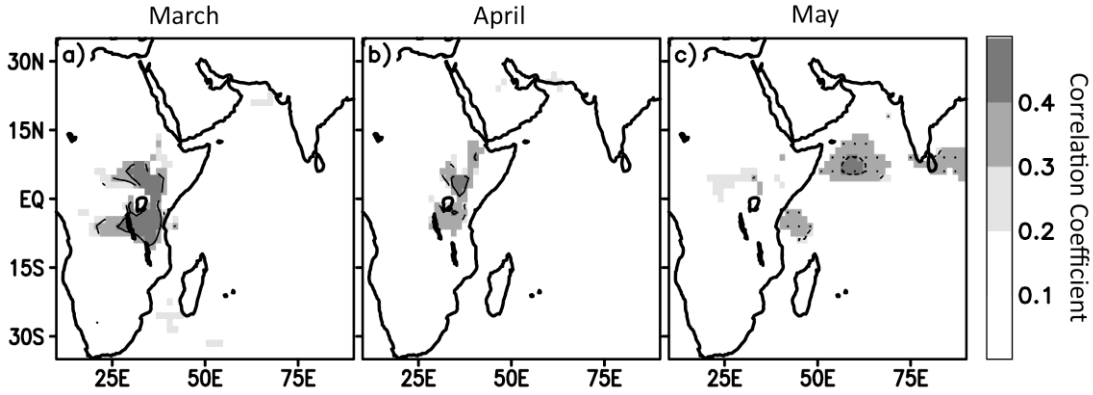

Figure 3.11: (a-c) Correlations between domain-averaged daily rainfall anomalies and 850 hPa zonal wind anomalies for March, April and May. Only local correlations significant at the 99.9% level are shown, controlling the false discovery rate at 6%. Negative correlations are indicated by stippling.

In addition to the phase correlations displayed in Figure 3.10, we also examine correlations between the magnitudes of the [PC1 PC2] vectors and 850 hPa circulation fields in Figure 3.11. The methodology for these correlations is identical to that for the SPI correlations, except that L=132 for the moving bootstrap due stronger autocorrelation than in the SPI time series. For the magnitude correlations, the false discovery rate (FDR) is controlled at 6% since no significant values are obtained using a 5% FDR. The threshold p-value in Eq. 3.6 is found to be 0.00067.

For the magnitude correlations, the most significant correlations are with the zonal wind, so only the zonal wind correlations are shown in Figure 3.11. The results here are consistent with those discussed by previous authors [e.g., *Camberlin and Phillipon,* 2002]. In both March and April, wet rainfall conditions are associated with strong easterly anomalies in the lower- and mid- troposphere. In May, wet (dry) conditions are associated with a weakened (enhanced) monsoon flow across the Indian Ocean. These results suggest that despite the relatively short record, the TRMM rainfall product is able to extract these signals noted in previous studies.

3.5 Summary and Conclusions

The Seasonal Position Index (SPI) and the Rainfall Regime Index (RRI) provide single-dimensional representations of the January – July progression of the ITCZ over East Africa. Reconstructions rainfall based on the SPI and RRI capture many important aspects of the spatial progression of rainfall, including jumps in latitude. The approach in this paper differs from previous studies in that it focuses directly on the seasonal cycle, and how day-to-day patterns of rainfall develop statistically as the season progresses.

Jump dates calculated from the two indices show a median jump date of 10 April. The two indices, though calculated very differently (the RRI through a cluster analysis and the SPI through a Principal Component Analysis), show quite similar results when analyzing year-to-year variability in the timing and character of rainfall jumps. Early (late) jumps are associated with positive (negative) index anomalies in April. Positive index anomalies in March are generally indicative of temporary early-season jumps above the equator, leading to more complicated jump structures and low jump clarity.

The SPI is used to examine dynamics associated with spatial anomalies ahead of and behind the mean seasonal cycle. Correlations between the SPI and circulation fields in March and April show a connection, on the daily timescale, between the cross-equatorial winds in the region of the nascent Somali Jet, and northward rainfall excursions. These results are consistent with the hypothesis of *Riddle and Cook* [2008], who suggest that jumps in the latitude of rainfall are associated with the nascent jet formation. While the formation of the nascent jet is correlated with the north/south position of rainfall, it does not appear to be correlated with the daily magnitude of rainfall, when averaged over the whole eastern African domain. Instead, the total magnitude of rainfall during March and April is correlated with equatorial westerly anomalies, a result which has been observed in several previous studies.

Correlations between the SPI and circulation fields in the May confirm a connection, on the daily timescale, between the strength of the Arabian Sea branch of the Somali Jet and northward rainfall excursions. The overall rainfall magnitude over eastern Africa is also negatively correlated with the Arabian Sea branch of the jet. These results are also consistent with previous studies which have connected dry conditions over eastern Africa in May with the onset of Indian monsoon flow across the Arabian Sea.

In summary, the SPI and RRI encapsulate important features of the northward progression of the ITCZ, including jumps ahead of and behind the mean climatology. In addition, a number of important dynamical relationships are captured using the unique framework developed in this paper. Since the location of the ITCZ is an important variable in tropical rainfall forecasts, we suggest that the SPI and RRI could be useful variables to examine in short-range or seasonal predictability studies of east African rainfall.

3.6 Acknowledgements

This research is to be submitted as a paper to the International Journal of Climatology, coauthored by Daniel Wilks. The work was supported by the American Association for University Women (AAUW) American Dissertation Fellowship. The ERA Interim Analysis for this research was provided by the European Center for Medium Range Weather Forecasts. We extend our gratitude to Natalie Mahowald and M. Todd Walter for editorial comments.

REFERENCES

Camberlin, P., and R. E. Okoola (2003), The onset and cessation of the ‘‘long rains’’ in eastern Africa and their interannual variability, Theor. Appl. Climatol., 75(1– 2), 43–54.

Camberlin, P., and N. Philippon (2002), The East African March-May rainy season: Associated atmospheric dynamics and predictability over the 1968–1997 period, J. Clim., 15, 1002–1019.

Camberlin, P., and J. G. Wairoto (1997), Intraseasonal wind anomalies related to wet and dry spells during the ‘‘long’’ and ‘‘short’’ rainy seasons in Kenya, Theor. Appl. Climatol., 58, 57– 69.

Camberlin, P., V. Moron, R. Okoola, N. Philappon, and W. Giteau (2009), Components of rainy seasons' variability in Equatorial East Africa: onset, cessation, rainfall frequency and intensity, Theor. Appl. Climatol., 98, 237-249.

Camberlin, P., B. Fontaine, S. Louvet, P. Oettli, P. Valimba (2010), Climate adjustments over Africa accompanying the Indian monsoon onset, J. Clim., *in press*

Chen, X., and J. M. Wallace (1993), Cluster analysis of the northern hemisphere wintertime 500-hPa height field: Spatial patterns, J. Atmos. Sci., 50 (6), 2674-2696.

Diro, G. T., E. Black, and D. I. F. Grimes (2008), Seasonal forecasting of Ethiopian spring rains, Meteorol. Appl., 15, 73-83.

Diro, G. T., D. I. F. Grimes, E. Black, A. O'Neill, and E. Pardo-Iguzquiza (2009), Evaluation of reanalysis rainfall estimates over Ethiopia, Int. J. Climlatol., 29, 67-78.

Franchereau, P.-A., B. Pohl, and C. J. C Reason (2008), Recurrent daily OLR patterns in the Southern Africa/Southwest Indian Ocean region, incplications for South African rainfall and teleconnections, Clim. Dyn., DOI: 10.1007/s00382-008-0426-2

Gissila, T., E. Black, D. I. F. Grimes, and J. M. Slingo (2004), Seasonal forecasting of the Ethiopian summer rains, Int. J. Climatol., 24(11), 1345–1358.

Hagos, S. M., and K. H. Cook (2007), Dynamics of the West African monsoon jump, J. Clim., 20(21), 5264– 5284.

Hastenrath, S., A. Nicklis, and L. Greischar (1993), Atmospheric-hydrospheric mechanisms of climate anomalies in the western equatorial Indian Ocean, J. Geophys. Res., 98(C11), 20,219– 20,235.

Herman, A., V. B. Kumar, P. A. Arkin, and J. V. Kousky (1997), Objectively determined 10-day African rainfall estimates created for famine early warming systems, Int. J. Remote Sens., 18, 2147– 2159.

Hu, Y.Y., D. Li, and J.P. Liu (2007), Abrupt seasonal variation of the ITCZ and the Hadley circulation, Geophys. Res. Lett., 34, L18814, doi: 10.1029/2007GL030950

Huffman, G. J., R. F. Adler, D. T. Bolvin, G. Gu, E. J. Nelkin, K. P. Bowman, Y. Hong, E. F. Stocker, and D. B. Wolff (2007), The TRMM multi-satellite precipitation analysis (TMPA): Quasi-global, multiyear, combined-sensor precipitation estimates at fine scales, J. Hydrometeorol., 8(1), 38– 55.

Levin, N. E., E. J. Zipser, and T. E. Cerling (2009), Isotopic composition of waters from Ethiopia and Kenya, J. Geophys. Res., 114, D23306, doi: 10.1029/2009JD012166.

Michelangeli, P.-A., R. Vautard, and B. Legras (1995), Weather Regimes: Recurrence and Quasi Stationarity. J. Atmos. Sci., 52(8), 1237-1256.

Mutai, C. C., and M. N. Ward (2000), East African rainfall and the tropical circulation/convection on intraseasonal timescales, *J. Clim.*, 13, 3915– 3939.

New, M., D. Lister, M. Hulme, and I. Makin (2002), A high-resolution data set of surface climate over global land areas, *Clim. Res.*, 21, 1 –25.

Nicholson, S. E. (1996), A review of climate dynamics and climate variability in eastern Africa, in *The Limnology, Climatology and Paleoclimatology of the East African Lakes*, edited by T. C. Johnson and E. O. Odada, pp. 25-56, Gordon and Breach, Amsterdam.

Ogallo, L. J. (1988), Relationships between seasonal rainfall in East Africa and the Southern Oscillation, *Int. J. Climatol.*, 8, 31–43.

Okoola, R. E. (1999), A diagnostic study of the eastern Africa monsoon circulation during the Northern Hemisphere spring season, Int. J. Climatol., 19, 143– 168.

Pohl, B., P. Camberlin, and P. Roucou (2005), Typology of pentad circulation anomalies over the Eastern Africa – Western Indian Ocean region, and their relationship with rainfall, Clim. Res., 29: 111-127.

Pohl, B., and P. Camberlin (2006a), Influence of the Madden-Julian Oscillation on East African rainfall. part I: Intraseasonal variability and regional dependency, *Q. J. R. Meteorol. Soc*., 132(621), 2521– 2539.

Pohl, B., and P. Camberlin (2006b), Influence of the Madden-Julian Oscillation on East African rainfall. part II: March-May season extremes and interannual variability, Q. J. R. Meteorol. Soc., 132(621), 2541– 2558.

Riddle E.E and K.H. Cook (2008), Abrupt transitions in rainfall over the Greater Horn of Africa: Observations and Regional Climate simulations, Journal of Geophysical Research 113 (D15), D15109.

Segele, Z. T., and P. J. Lamb (2005), Characterization and variability of Kiremt rainy season over Ethiopia, Meteorol. Atmos. Phys., 89(1 – 4), 153– 180.

Shanko, D., and P. Camberlin (1998), The effects of the Southwest Indian Ocean tropical cyclones on Ethiopian drought, Int. J. Climatol., 18, 1373– 1388.

Simmons, A, S. Uppala, D. Dee, and S. Kobayashi, 2007: *ERA-Interim: New ECMWF reanalysis products from 1989 onwards.* Newsletter 110 - Winter 2006/07, ECMWF, 11 pp.

Sultan, B., and S. Janicot (2000), Abrupt shift of the ITCZ over West Africa and intra-seasonal variability, Geophys. Res. Lett., 27(20), 3353– 3356.

Wheeler, M. C., and H. Hendon (2004), An all-season real-time multivariate MJO index: Development of an index for monitoring and prediction. Mon. Weather Rev., 132, 1917-1932.

Wilks, D. S. (1997), Resampling hypothesis tests for autocorrelated fields. *Journal of Climate*, 10, 65-82.

Wilks, D. S. (2006a), *Statistical Methods in the Atmospheric Sciences*, Vol 91, International Geophysics Series, Academic Press

Wilks, D. S. (2006b), On "field significance" and the false discovery rate, J. Appl. Meteorol. and Climatol., 45 (9), 1181-1189: doi: 10.1175/JAM2404.1

Xian, P. and R. L. Miller (2008), Abrupt seasonal migration of the ITCZ into the summer hemisphere, J. Atmos. Sci., 65, 1878-1895.

Xue, Y., H.-M. H. Juang, W.-P. Li, S. Prince, R. DeFries, Y. Jiao, and R. Vasic (2004), Role of land surface processes in monsoon development: East Asia and West Africa, J. Geophys. Res., 109(D3), D03105, doi:10.1029/2003JD003556.

Zorita, E., and F. F. Tilya (2002), Rainfall variability in Northern Tanzania in the March-May season (long rains) and its links to large-scale climate forcing, Clim. Res., 20, 31– 40.

CHAPTER 4

VARIABILITY AND DYNAMICS OF THE "NASCENT" SOMALI JET

4.1 Introduction

The Somali Jet (SJ) dominates the low-level atmospheric circulation over the western Indian Ocean during the boreal summer. This major cross-equatorial jet stream, which is also sometimes called the East African Jet, the Findlater Jet or the East African low-level jet is an important component of the regional and global climate system. It transports water vapor and energy across the equator, providing moisture for the Indian summer monsoon and impacting global distributions of rainfall.

While the SJ is strongest during the summer months (June-September), studies have shown that the cross-equatorial branch of the jet begins to form along the coast of East Africa much earlier in the year. Using wind velocity measurements from radar and balloons, *Findlater* [1971] demonstrates the presence of a southerly jet along equatorial East Africa as early as April. This cross-equatorial coastal jet, which we will call the nascent Somali Jet (NSJ), is also resolved during April and May in the NCEP and ERA-40 reanalyses, in 30-km regional climate model simulations [*Riddle and Cook*, 2008], and in GCM simulations [*Slingo et al.*, 2005]. The nascent SJ and the fully-formed SJ are shown in Figure 4.1. This study focuses on the cross-equatorial portion of the jet (indicated by the inset box in Figure 4.1).

Variability of the NSJ is potentially important climatologically. *Riddle and Cook* [2008] propose, for example, that the jet is an essential source of moisture for the spring rains over southern Ethiopia. Therefore, understanding the timing of the jet development could be important for improving rainfall prediction in that region.

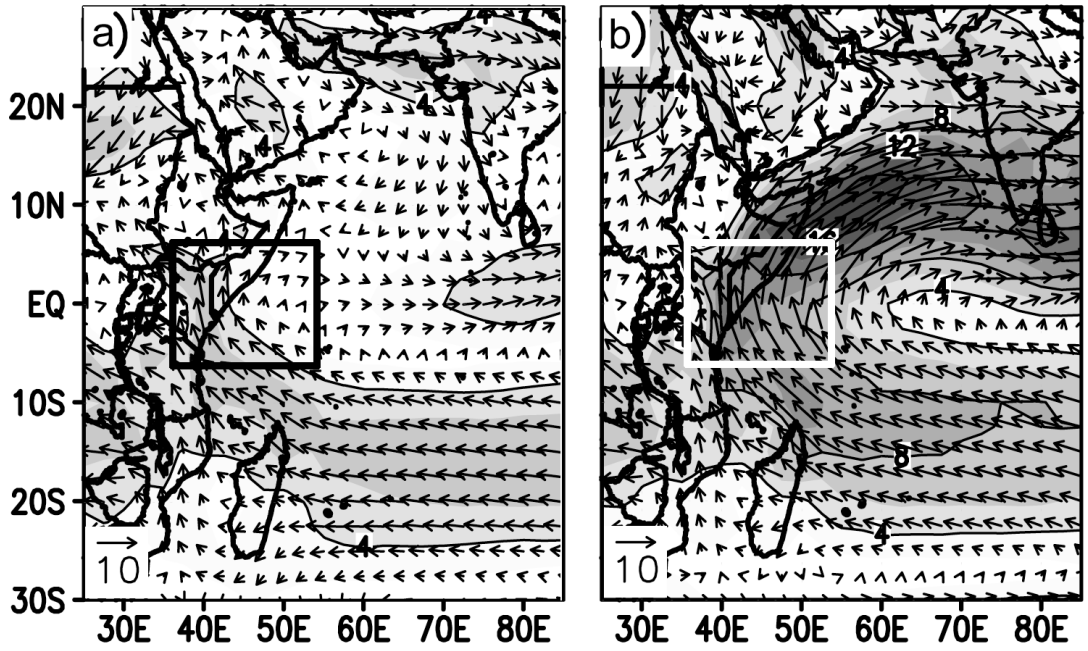

Figure 4.1: 850 hPa isotachs and wind velocities from the ERA-40 reanalysis showing the (a) nascent SJ (15 April – 15 May) and (b) fully-formed SJ (01June – 30 June). The jet focus region (37.5 E to 52.5 E; 5 S to 5 N) is shown as a black square in (a) and as a white square in (b).

This paper fills a gap in the literature by providing a detailed description of the nascent Somali Jet. The first section uses the NCEP-2 and ERA-40 reanalyses to describe the climatological evolution and dynamics of the nascent jet. The second section describes interannual variability in the NSJ development, and takes a preliminary step towards understanding the timing of the jet formation. The final section examines the diurnal cycle of the nascent jet and compares it to the diurnal cycle of rainfall over southern Ethiopia.

4.2 Background

The East African low-level jet stream was identified as a major summertime circulation feature by J. J. Findlater in the late 1960's [*Findlater*, 1966, 1967, 1969a, 1969b]. Findlater was also the first to document the seasonal cycle of the jet using

radar and balloon measurements and to note a branch of the jet "protruding across the equator into eastern Africa" during the months of April and May, well before the onset of the Indian monsoon [*Findlater*, 1971]. Since this early description of the nascent jet, most studies have focused on the fully established SJ in the boreal summer months (June – September).

The large-scale dynamics controlling the summertime SJ have been examined using simplified models as well as full numerical simulations [*Anderson,* 1976; *Krishnamurti et al.*, 1976; *Hart,* 1977; *Bannon,* 1979a; *Bannon,* 1979b; *Bannon,* 1982; *Paegle and Geisler,* 1986; *Hoskins and Rodwell,* 1995; *Rodwell and Hoskins,* 1995; *Chakrabody et al.,* 2009]. These models demonstrate that the low-level flow across the equator is fundamentally driven by strong inter-hemispheric gradients in diabatic heating associated with the Indian summer monsoon [e.g., *Anderson,* 1976; *Hart,* 1977; *Hoskins and Rodwell,* 1995, *Chakrabody et al.,* 2009]. For example, *Hoskins and Rodwell* [1995] show that without the inter-hemsipheric difference in diabatic heating, the cross-equatorial jet does not form.

These studies have also emphasized the importance of the East African topography in concentrating the cross-equatorial flow into a coherent jet east of the East African highlands. Simulations that remove the East African topography show that, while a gentle cross-equatorial flow still exists, it is much broader and penetrates further across the African continent than when the topography is present [e.g., *Kirshnamurti et al.*, 1976; *Paegle and Geisler,* 1986; *Hoskins and Rodwell,* 1995; *Slingo et al.*, 2005; *Sepulchre et al.*, 2006; *Chakrabody et al.,* 2009]. The strong wind velocities observed in the jet core, averaging approximately 18-24 m/s for July [*Findlater,* 1971], are generated east of the mountains by the process of western boundary current intensification [e.g., *Anderson*, 1976].

Friction over the African continent is also thought to play an important role in determining the structure of the jet. Horizontal shear on the western side of the jet core is controlled by surface friction [e.g., *Bannon,* 1979a; *Hart,* 1977]. In addition, the generation of potential vorticity from friction as the jet passes over Somalia may be important for maintaining the jet position north the equator as it crosses the Arabian Sea [*Rodwell and Hoskins,* 1995].

The summertime SJ exhibits intraseasonal and synoptic variability. A 14-day oscillation in strength of cross equatorial winds has been linked to variability in the meridional monsoon pressure gradient across the Arabian Sea [*Krisnamurti and Bhalme*, 1976; *Raghavan et al.*, 1975; *Bannon*, 1982]. Other studies show a link between synoptic disturbances in the southern hemisphere and the strength and structure of the summertime cross-equatorial SJ. Mid-latitude disturbances have been observed to cause surges through the Mozambique Channel, increasing the strength and changing the mesoscale structure of cross-equatorial flow a few days later [*Findlater*, 1969b*; Hart et al.*, 1978; *Cadet and Desbois*, 1981; *Rao and Haney*, 1982; *Van de Boogaard and Rao*, 1984]. These surges can propagate northward via the SJ into the northern hemisphere [*Bannon*, 1979b, 1982] and potentially trigger break periods in the Indian summer monsoon [*Rodwell*, 1997; *Joseph and Sijikumar*, 2004].

In 1977 and 1979, two intensive campaigns (MONSOON77 and MONEX79) were organized to probe the structure of the summertime jet near the coast of East Africa using aircraft, pilot balloons, and long-duration constant altitude balloon flights. Results from these campaigns were used to examine the balance of forces acting on the boundary layer of the summertime SJ [*Krishnamurti and Wong*, 1979; *Reverdin and Sommeria*, 1983; *Krisnamurti et al.,* 1983].

The summertime cross-equatorial branch of the SJ exhibits a significant diurnal cycle, with daytime windspeeds near the equator approximately 30% smaller

on average than during the nighttime [*Findlater,* 1977; *Hart et al.*, 1978]. At some locations (e.g., over northern Somalia) the diurnal cycle is even larger, with daytime winds half of the maximum nighttime wind speed [*Ardanuy*, 1979]. In addition, wind velocities have been observed to have a slightly stronger easterly component during the day than during the night [*Hart et al.*, 1978; *Ardunuy*, 1979]. The majority of authors explain the diurnal cycle as a response to increased convection and turbulence causing more friction over land during the day, possibly combined with a land/sea breeze circulation [*Hart et al.*, 1978; *Bannon,* 1979b; *Rubenstein,* 1981].

Fewer papers have examined the Somali Jet during the boreal springtime. Of these papers, most have been interested in the formation of the Arabian Sea branch of the jet in early June associated with the onset of the Asian Summer monsoon [e.g., *Annamalai et al.*, 1999; *Wu et al.*, 2001; *Taniguchi and Koike*, 2006; *Boos and Emmanuel*, 2009]. *Fasullo and Webster* [2003] have found that meridional moisture transport over the Arabian Sea (mostly via the SJ) can be used as a good index to describe the Indian monsoon onset.

Besides Findlater's original paper in 1971, very few papers have examined the cross-equatorial portion of the "nascent" Somali Jet in March-May. *Slingo et. al.* [2005] describe the seasonal low-level circulation cycle over the western Indian Ocean and examine how it changes in a global circulation model when the East African topography is removed. The nascent cross-equatorial jet can be resolved in their simulations during the MAM season, but this feature was not explicitly discussed in the paper. *Reverdin and Sommeria* [1983] analyze trajectories from super-pressure balloons which were launched north of Madagascar during 20-30 May 1979. Several of these quasi-Lagrangian balloon trajectories followed the nascent jet across the equator, continuing northward into the Horn of Africa.

Riddle and Cook [2008] demonstrate a connection between the evolution of the nascent jet and latitude shifts in rainfall over the Greater Horn of Africa (GHA). Their regional climate model simulations suggest that transport of moisture across the equator associated with the formation of the NSJ may be responsible for the onset of the boreal springtime rainy season over southern Ethiopia. In June, the Arabian Sea branch of the SJ removes this moisture source, and rainfall over southern Ethiopia decreases [*Riddle and Cook*, 2008]. These results highlight the potential impact of the nascent SJ on the hydrologic cycle of the region.

4.3 Data and Model Description

This study uses ERA-40 [*Uppala et al.,* 2005] and NCEP-2 [*Kanamitsu*, 2002] reanalyses to study the seasonal cycle and onset characteristics of the nascent Somali Jet (NSJ) and a 30-km regional model simulation to examine the jet's diurnal cycle.

Climatologies created from the reanalyses are used to examine the climatological evolution of the NSJ. For comparison, the two reanalyses are averaged over the same 23-year period common to both projects (1979-2001) and interpolated to the same 2.5 degree grid. For brevity, some results are presented based on the ERA-40 reanalysis only while any major differences between the two products are discussed in the text. The ERA-40 model is T159 (approx. 1.125 deg) and the NCEP-2 model is T62 (approx. 1.9 deg). These different underlying resolutions can be important given the complex topography of East Africa.

Both ERA-40 and NCEP-2 reanalyses assimilate radiosonde, satellite and surface observations. The ERA-40 reanalysis assimilates available measurements from 38 upper air stations in the equatorial jet region (10 S to 10 N and 35 E to 65 E), though the data from some of these stations are incomplete or of poor quality. Soundings from only ten of the of the 38 stations are retained in the ERA-40

assimilation process at an overall rate greater than one sounding per week when averaged over the 92 month period used for this study (March-June 1979-2001).

A regional model with a 30 km horizontal grid is used to examine the diurnal cycle of the NSJ. The regional model used for this study is the Weather Research and Forecasting model version 2.2 (WRF2.2) using the Advanced Research WRF dynamical core (*Shamrock et al.*, 2005). WRF is a next-generation limited-area non-hydrostatic model run on terrain-following sigma coordinates with a suite of physical parameterization options.

For this simulation, we use the new Kain-Fritch convective scheme (e.g., *Kain,* 2004), the Purdue Lin microphysics scheme (Lin *et. al.* 1983), the Rapid Radiative Transfer Model (RRTM) longwave [*Mlawer et al.*, 1997] and Dudhia shortwave [*Dudhia*, 1989] radiation schemes, the Mellor-Yamada-Janjic TKE boundary layer and surface layer schemes [e.g., *Mellor and Yamada,* 1982; *Janjic,* 2002] and the land surface model from the Rapid Update Cycle (RUC) forecast model [e.g., *Smirnova et al.*, 2000]. Over Africa, the RUC land surface model has been shown to perform better in conjunction with WRF than the more commonly used NOAH land surface model [*Patricola and Cook*, 2010].

The domain for the simulation extends from 11 S to 30 N and 23 E to 57 E. The simulation is run on a 30 km grid with a two-minute model time step. This domain was chosen to include the entire region of the cross-equatorial SJ with a resolution sufficient to effectively capture many important features of the region's complex topography, including the Turkana channel between the Ethiopian and East African highlands. Previous MM5 simulations using this same domain and resolution were able to accurately capture the seasonal evolution of the SJ [*Riddle and Cook*, 2008]. WRF was used here to update the older simulations using the current state-of–the-art in regional modeling [*Shamrock et al.*, 2005].

Figure 4.2 shows the model domain with topography resolved at (a) the 2.5° resolution of the gridded reanalysis used for this study, (b) the underlying T159 model resolution of the ERA-40 reanalysis, and (c) the 30 km regional model resolution). The underlying model resolution of the NCEP reanalysis is intermediate between the resolutions shown in Figure 4.2a and Figure 4.2b.

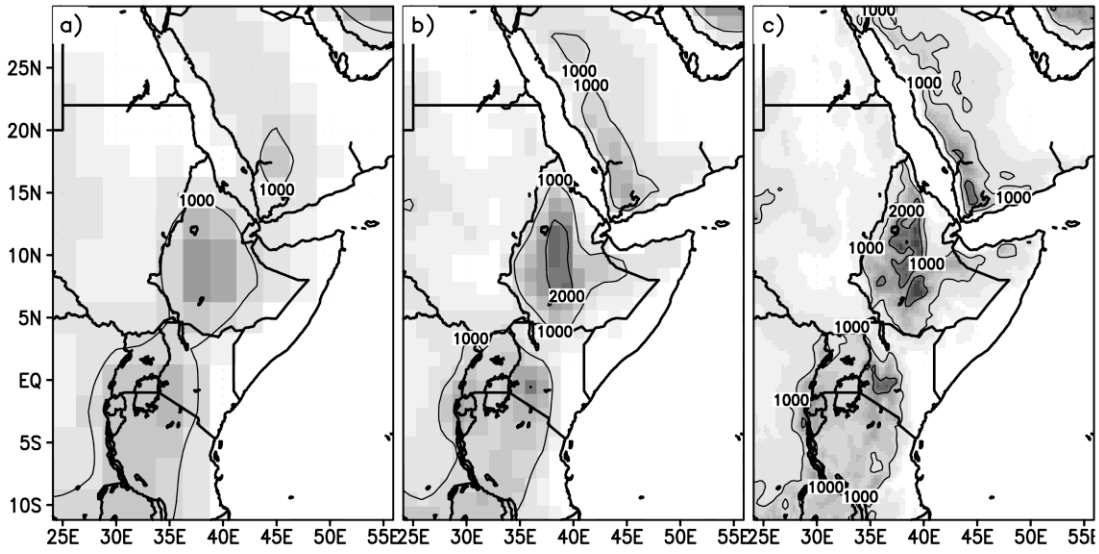

Figure 4.2: Model domain with topography in meters at (a) 2.5° resolution, (b) ERA-40 model (T159) resolution and (c) the regional model (30 km) resolution. Contours are shown at 1000 and 2000 meters.

The initial and boundary conditions for the simulation are derived from a 10-year (1980-1989) ERA-40 reanalysis climatology [*Uppala et al.*, 2005]. Sea surface temperatures are also prescribed based on this reanalysis. To create the lateral boundary data, mean monthly ERA-40 output on a 2.5° grid is interpolated linearly to 12 hour intervals before being input to the model. By using smoothed climatological data at the boundaries, synoptic and diurnal perturbations entering the domain from the lateral margins are absent from the simulation. A number of previous studies [e.g., *Vizy and Cook*, 2002; *Patricola and Cook*, 2007] have shown that the observed mean

seasonal cycle can be accurately reproduced in the tropics even when transients on the lateral boundaries are ignored. In this paper, we demonstrate that the diurnal cycle simulated internally from the 24-hour solar cycle captures the diurnal variability of the jet reasonably well.

The WRF simulation is five months long, from 15 February to 15 July, with 15 days discarded for spin-up and output saved every three hours. The mean diurnal cycle is then calculated for three separate 30-day periods, showing three stages in the formation of the SJ: 1) a period before the SJ formation (pre-jet), 2) a period during the nascent springtime SJ (nascent jet) and 3) a period during the fully-formed summertime SJ (full jet).

The model and reanalysis are evaluated using up-to-date radiosonde data as well as observations compiled in earlier papers describing the jet [*Findlater*, 1971; *Hart et al.*, 1978]. A radiosonde station over Garissa, Kenya (39.6 E, 0.5 S) is chosen to evaluate the jet strength and diurnal variability because of its location near the jet core. Radiosonde data is obtained from the ERA-40 upper air radiosonde observation feedback reports created at NCAR and selected to coincide with the years averaged in the reanalysis (1979-2001). Data that are either rejected or blacklisted by the ERA-40 quality control are not used in the comparison. Aircraft transects taken during the MONSOON77 campaign and reported in a paper by *Hart et al.* [1978] are used for evaluation of the June/July diurnal cycle.

4.4 Climatological Evolution of the NSJ

In order to understand variability in the formation of the NSJ, it is first necessary to document its mean climatological evolution. This section expands on previous work by 1) evaluating the ability of modern reanalysis products to capture the nascent jet development, 2) presenting the local momentum budget associated with the

nascent jet evolution, and 3) putting these local dynamics in the context of large-scale seasonal changes.

4.4.1 Evaluation of the Reanalyses

We devote a short section to assessing the quality of the two reanalyses at capturing seasonal evolution of the nascent Somali Jet (NSJ). The reanalyses will be compared with each other, with upper air soundings near the jet core, and with documentation of the jet from the literature [*Findlater*, 1971].

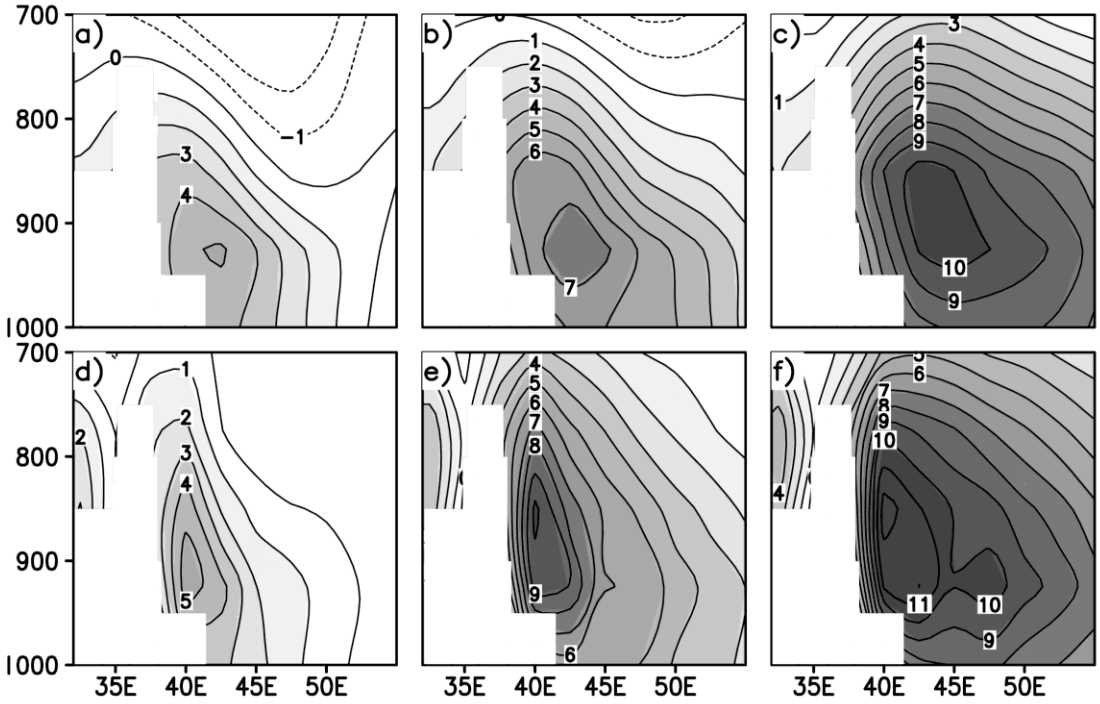

Figure 4.3: Meridional winds across the equator based on (a-c) the NCEP-2 reanalysis climatology (1979-2001) and (d-f) the ERA-40 reanalysis climatology for the months of April (left), May (center) and June (right). Topography for all panels (white) is taken from a 30 km topography grid.

Panels in Figure 4.3 show monthly-averaged (April - June) cross-sections of meridional winds at the equator based on the two reanalysis climatologies.

Topography, shown in white in Figure 4.3, is from a 30-km grid. In both reanalyses, the nascent jet is present, but weak, in April, and strengthens and widens in the subsequent months. However, the two reanalyses show some differences in both the strength and the location of the jet core. The ERA-40 reanalysis shows a stronger jet core, concentrated at a higher level and closer to the topography than the NCEP-2 reanalysis.

Findlater [1971] presents similar equatorial cross-sections of the jet for April, May and June (Figure 4 in *Findlater* [1971] – not reproduced here). These cross-sections are based on mean profiles calculated at nine different pilot balloon and radar stations located near or on the equator between 35 E and 65 E. Between two and ten years of data (from 1939-1967) were used at each station. Findlater's cross-sections show even stronger core windspeeds than ERA-40, with meridional jet core speeds over Garissa, Kenya (0.5 S, 39.6 E) averaging 12 m/s in May and 14 m/s in June. The position of the jet core in Findlater's plots (April - June) is similar to ERA-40, with maximum winds at approximately 40 E at 850 hPa. Recent soundings from Garissa (1979-2001), however, show core winds averaging only 9 m/s and 11 m/s for May and June respectively, with a lower core near 900 hPa. Since these recent soundings are most commonly taken during the afternoon when the jet is weakest, they may be biased low.

These comparisons suggest that both reanalysis products capture the SJ formation in April, May and June. Despite some uncertainties in the jet core height and strength, the comparisons suggest that the lateral position and strength of the jet core are more realistic in ERA-40 than in NCEP-2. This difference is likely due to the fact that the model topography is better resolved in the ERA-40 model.

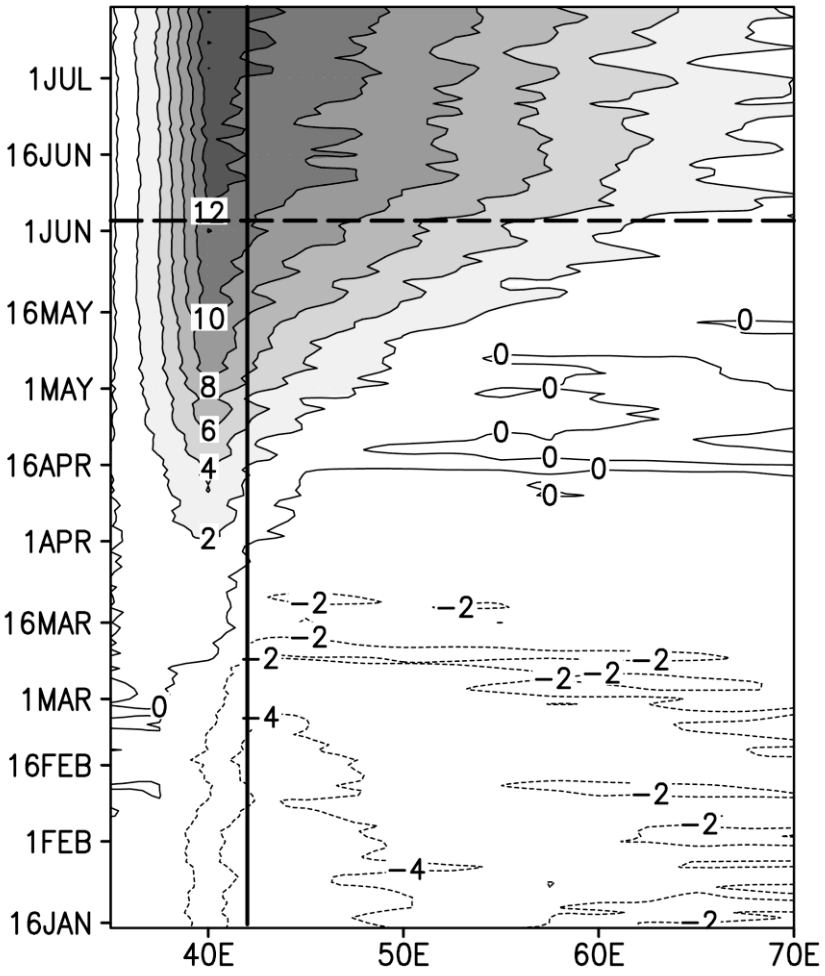

Figure 4.4: Hovmöller diagram showing the boreal springtime development of meridional 850 hPa winds across the equator. The vertical solid line shows the location of the coastline. The horizontal dashed line shows the mean onset date of the Indian summer monsoon.

4.4.2 Momentum Budget

A summary of the climatological formation of the jet is shown in Figure 4.4 in the format of a Hövmöller diagram. Meridional winds across the equator are weak in January through March and mostly northerly. Starting in March, a very weak southerly component develops in the flow over land near the East African topography. This southerly flow begins to strengthen in April and increases steadily throughout

April and May. During these months, the southerly flow also spreads gradually to the east across the Indian Ocean. The nascent jet is never in a static phase, but rather strengthens and grows continually throughout the months of April and May leading up to the onset of the Indian summer monsoon at approximately the beginning of June. A final rapid increase in the magnitude and breadth of the jet occurs concurrently with the monsoon onset.

A momentum budget is calculated based on the NCEP-2 and ERA-40 reanalyses to examine the relationship between the jet development and the local pressure gradient at 850 hPa over the jet focus region (37.5 E to 52.5 E; 5 S to 5 N) shown in Figure 4.1. The Eulerian budget for the horizontal momentum on a constant pressure surface is given by:

$$\underbrace{\frac{\partial \vec{u}_h}{\partial t}}_{1} = \underbrace{-\vec{u}_h \cdot \nabla \vec{u}_h}_{2} \underbrace{-\nabla_h \Phi}_{3} \underbrace{-f\left(\hat{k} \times \vec{u}_h\right)}_{4} \underbrace{-\omega \frac{\partial \vec{u}_h}{\partial P}}_{5} \underbrace{+\vec{F}}_{6} \tag{4.1}$$

where the subscript "h" refers to the component of a vector parallel to a constant pressure surface, Φ is the geopotential height, ω is the pressure velocity, and F is the vertical eddy diffusion of momentum.

The six terms in equation (1) represent: 1) the unsteady time rate of change of momentum, 2) horizontal advection of momentum, 3) the force due to the geopotential height gradient, 4) the coriolis force 5) vertical advection of momentum, and 6) vertical diffusion of momentum by eddies. Terms (1) through (4) are calculated with a standard first-order finite difference technique at the 850 hPa level based on the daily-averaged ERA-40 reanalysis climatology. Because the climatology smoothes out low-frequency variability, the unsteady term (1) is found to be very small throughout the jet's seasonal evolution and is not shown in the following analysis.

Terms five and six are lumped together and calculated as the residual in the momentum budget. When the residual is plotted (not shown) it is generally found to be stronger over land than over the ocean and to generally be nearly anti-aligned with the direction of the flow. Physically, this behavior suggests that residual is dominated by the term (6) in equation (1) and can be generally considered to be a proxy for the friction in most regions. This alignment is not perfect, however, and vertical advection and or truncation errors may also contribute to the residual in some regions, including over land points in the jet focus region (37.5 E to 52.5 E; 5 S to 5 N) shown in Figure 4.1.

Figure 4.5 shows the relationship between the wind direction and the direction of the pressure gradient force over the jet focus region marked in Figure 4.1. The black line in Figure 4.5 shows the wind direction. Winds in February are easterly over the land and northeasterly over the ocean. Starting in March, winds over both land and ocean begin to swing to the north. The wind direction changes most rapidly in April and southerly flow is established by the beginning of May.

The grey x's in Figure 4.5 show the direction of the pressure gradient force (PGF). Since the flow is at the equator, it might be expected that the wind direction and PGF would be aligned, since winds would generally flow down the pressure gradient in the absence of other forces except friction. While this is approximately true, over the ocean the directions of the wind and the PGF diverge as the jet develops with the winds lagging the pressure gradient force by approximately 45° in May and June. Over land, the NCEP-2 winds and PGF are closely aligned (not shown), while ERA-40 winds swing to the north more rapidly than the PGF.

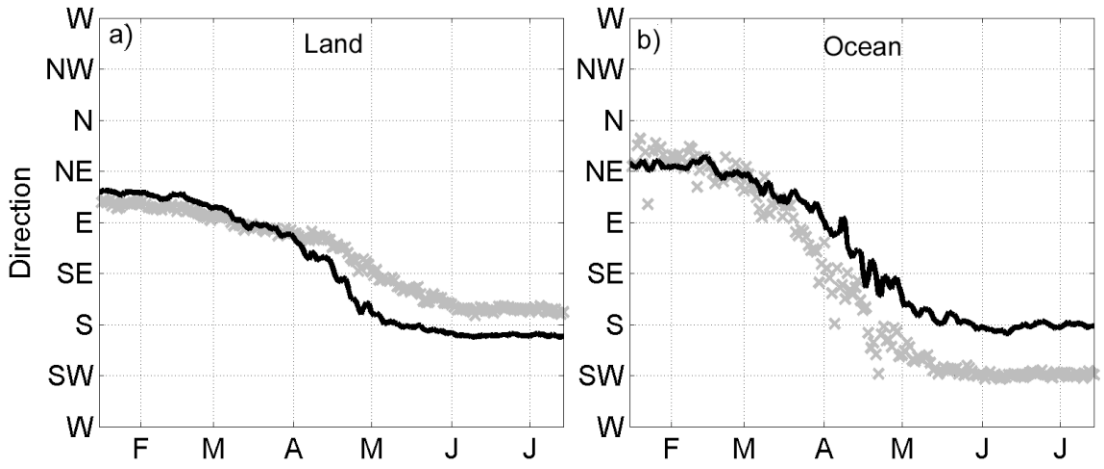

Figure 4.5. Direction of ERA-40 850 hPa climatological winds (black line) and direction of the 850 hPa pressure gradient force (grey x's) averaged over (a) land and (b) ocean points in the jet focus region (-5º S to 5º N; 37.5º E to 52.5º E).

Figure 4.6 shows the seasonal cycle of the terms in the momentum equation, based on the ERA-40 climatology. The terms in the momentum budget are averaged over the same land and ocean points as described in Figure 4.5. Figures 4.6a and 4.6b show the terms in the u-momentum budget over land and water respectively. Figures 4.6c and 4.6d show terms in the v-momentum budget, while Figures 4.6e and 4.6f compare the total magnitude of the terms.

Over land (Figures 4.6a, 4.6c and 4.6e) the pressure gradient force and the residual term show a tight balance, as expected. The coriolis and advections terms are not negligible, however, but tend to balance each other out. The zonal pressure gradient decreases throughout April and May at the same time the meridional pressure gradient increases.

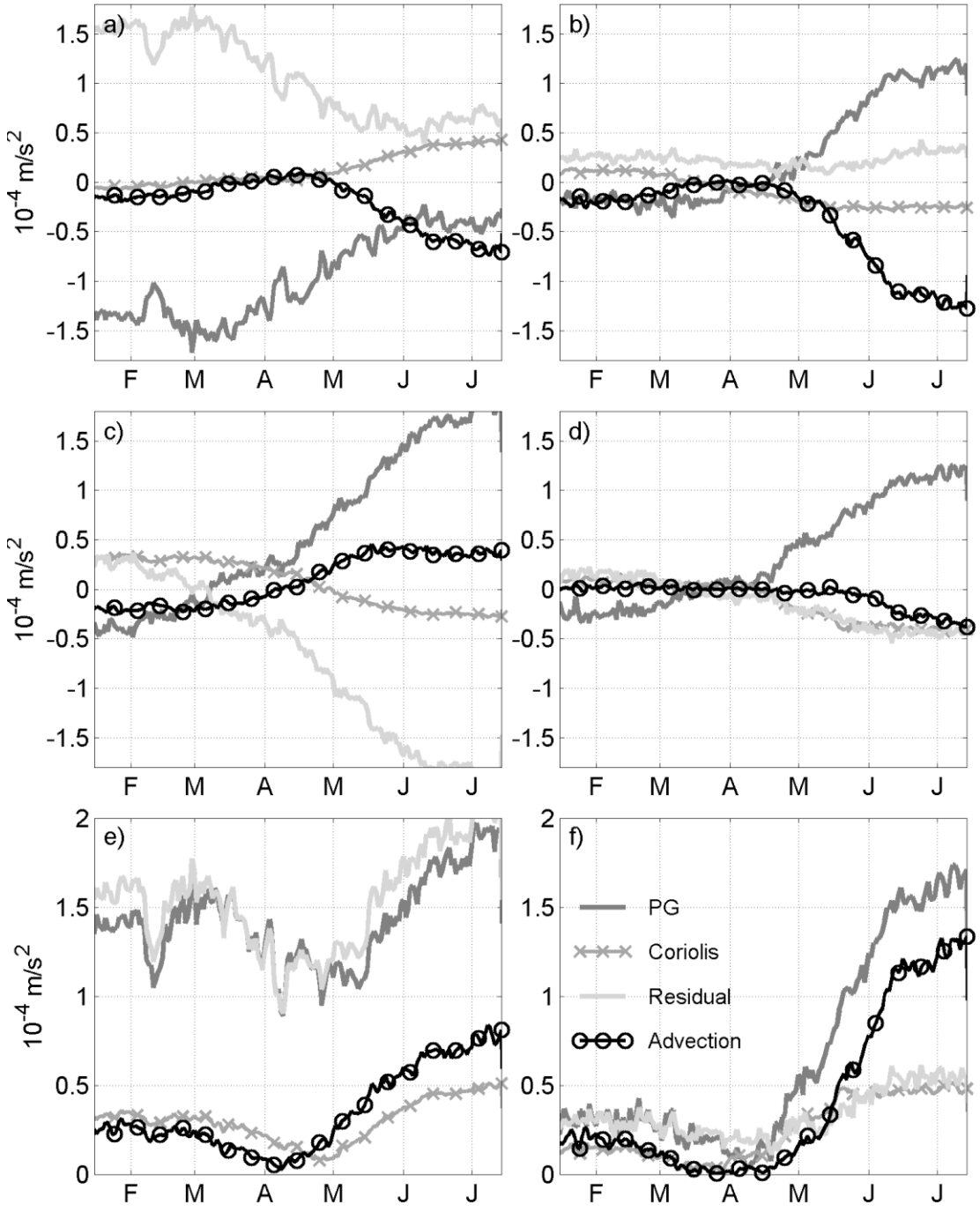

Figure 4.6: Terms in the x-momentum equation (a) over land and (b) over water, terms in the y-momentum equation (c) over land and (d) over water, and the total magnitude of terms in the momentum equation (e) over land and (f) over water. All are based on the ERA-40 momentum budget at 850 hPa averaged over the jet focus area (marked in Figure 4.1).

The tight balance between PGF and residual does not explain why the wind direction is not exactly aligned with the PGF in Figure 4.5a. The reason for the discrepancy is that the residual in this region is not exactly in opposition to the wind direction, suggesting that residual in this area cannot be explained entirely by surface friction. In contrast, the residual in the NCEP reanalysis opposes the direction of the flow in this region, and consequently the PGF and wind directions are tightly coupled in the NCEP reanalysis (not shown).

Over the ocean (Figures 4.6b, 4.6d and 4.6f) all forces are very weak until May when a southwesterly pressure gradient force begin to strengthen rapidly, balanced primarily by horizontal advection. The very rapid growth of this southwesterly pressure gradient force happens in conjunction with the striking increase in wind speeds over the ocean in May. From a Lagrangian perspective, this balance is between the pressure gradient force and an apparent centrifugal force generated as the jet bends in a clockwise direction near the equator. Because the advection term is not aligned with the flow, the jet winds over the ocean are not aligned with the pressure gradient force (Figure 4.5b).

These results for the summertime SJ agree with the literature. Several previous studies on the full Somali Jet have concluded that the strong horizontal shear at the western flank of the jet is generated by surface friction over the continent, while the horizontal shear on the eastern flank of the jet is inertial [e.g., *Hart*, 1977]. These results also agree with the results of *Krishnamurti and Wong* [1979] and *Reverdin and Sommeria* [1983] who found that advection was important to the boundary layer momentum balance in the SJ over the ocean.

In summary, since the nascent jet is primarily over land, its formation is governed by an approximate balance between the PGF and the residual, with the wind direction relatively closely aligned with the PGF, particularly in NCEP. The

widening of the jet over the ocean in May is governed primarily by a balance between the pressure gradient force and advection, with the residual playing a smaller role. As a result, the wind direction over the ocean lags the changes in pressure by 45 degrees.

4.4.3 Large-scale Context

The local momentum budget showed that the nascent jet formation over land is associated with a shift in the local pressure gradient force (PGF) from easterly to southerly. This section focuses on putting these local pressure changes in a larger-scale context.

Figure 4.7 shows 850 hPa geopotential heights and winds during the three stages of the jet development identified earlier (pre-jet, nascent jet, and full jet). In the southern hemisphere, the position of the Mascarene High shifts as the season evolves. In March (Figure 4.7a), the center of the high is located well away from the African continent at approximately 55 E and 35 S. In April/May, the Mascarene High is stronger, it is located further to the northwest and it is beginning to merge with a small high-pressure region over southern Africa. By June, the high is still stronger and has merged completely with the high over the continent. As the high moves to the west towards the African continent, the shape of the high also changes due to the development of a ridge extending to the north along the East African coast.

The geostrophic winds change in association with this shift in the position of the Mascarene High. In March, flow associated with the Mascarene High is anti-cyclonic around the high. As the high moves toward the continent and the ridge develops, the easterly trade winds north of Madagascar develop an equatorward component, eventually crossing the equator as part of the SJ.

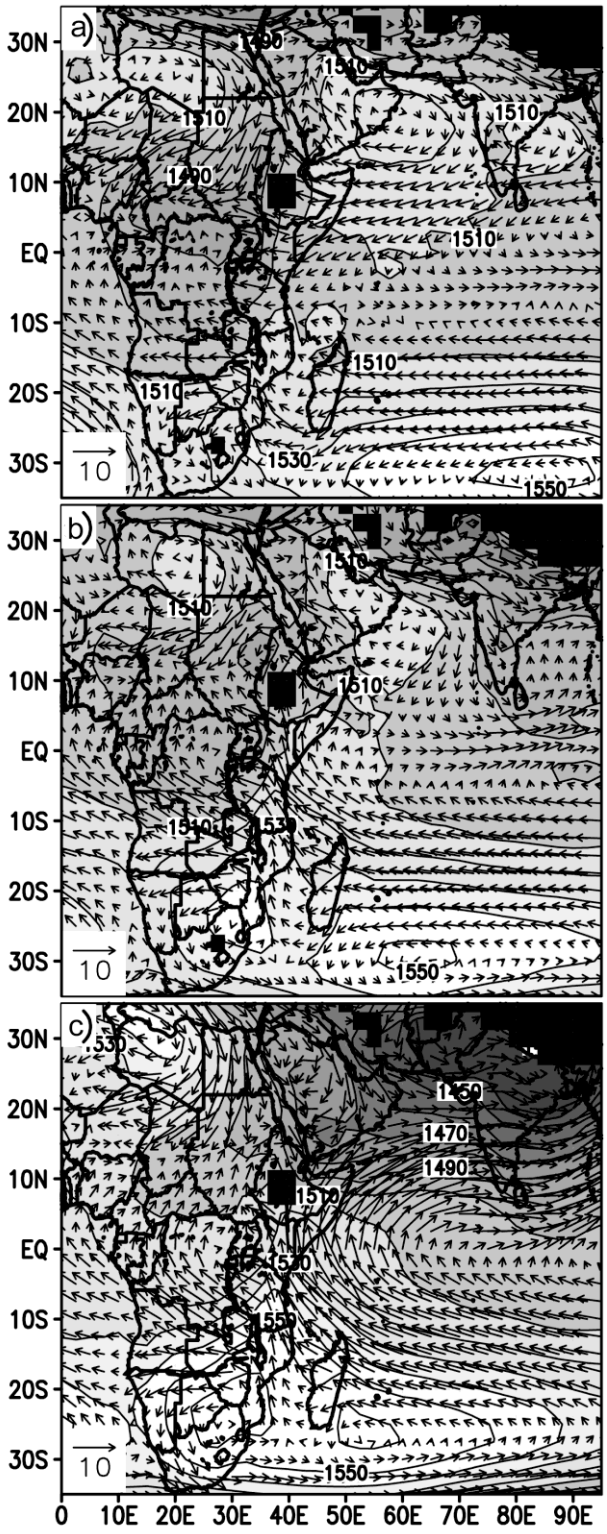

Figure 4.7: ERA-40 reanalysis climatology of 850 hPa geopotential heights and winds for (a) March, (b) mid-April to mid-May and (c) June.

The development of the ridge at the coastline is closely associated with the changing local pressure gradients discussed in the momentum budget analysis. The ridge increases geopotential heights over coastal Kenya just south of the equator leading to a strengthening of the cross-equatorial height gradient. In addition, by increasing onshore near-equatorial geopotential heights, the ridge serves to neutralize the zonal height gradient in the onshore region of the jet. Offshore, the position of the ridge in June also controls the south-easterly pressure gradient noted in the momentum budget. In short, the position of this ridge over the coastal equatorial region serves an important role in determining the local momentum budget of flow at the equator.

In the northern hemisphere, the height fields in Figure 4.7 show stages during the transition from the winter to summer monsoons. The height gradient over the Arabian Sea changes from a northerly gradient in March to a strong southerly gradient in June. This occurs as heights over India, the northern Arabian Sea and the southern Arabian Peninsula decrease steadily throughout the season. The local high over the southern Arabian Peninsula in March disappears by June as the Indian monsoon trough deepens and extends westward. The associated reversal of the geostrophic winds marks the development of zonal branch of the SJ across the Arabian Sea, and the onset of the summer monsoon circulation.

Figure 4.8 shows the differences in geopotential height, wind velocity and surface temperature between the stages shown in Figure 4.7. Figure 4.8a shows how the climatological heights and winds change between the pre-jet and nascent-jet stages. Figure 4.8b shows how these same fields change between the nascent-jet and full-jet stages. Figures 4.8c and 4.8d show the corresponding seasonal changes in surface temperature, also based on the ERA-40 reanalysis.

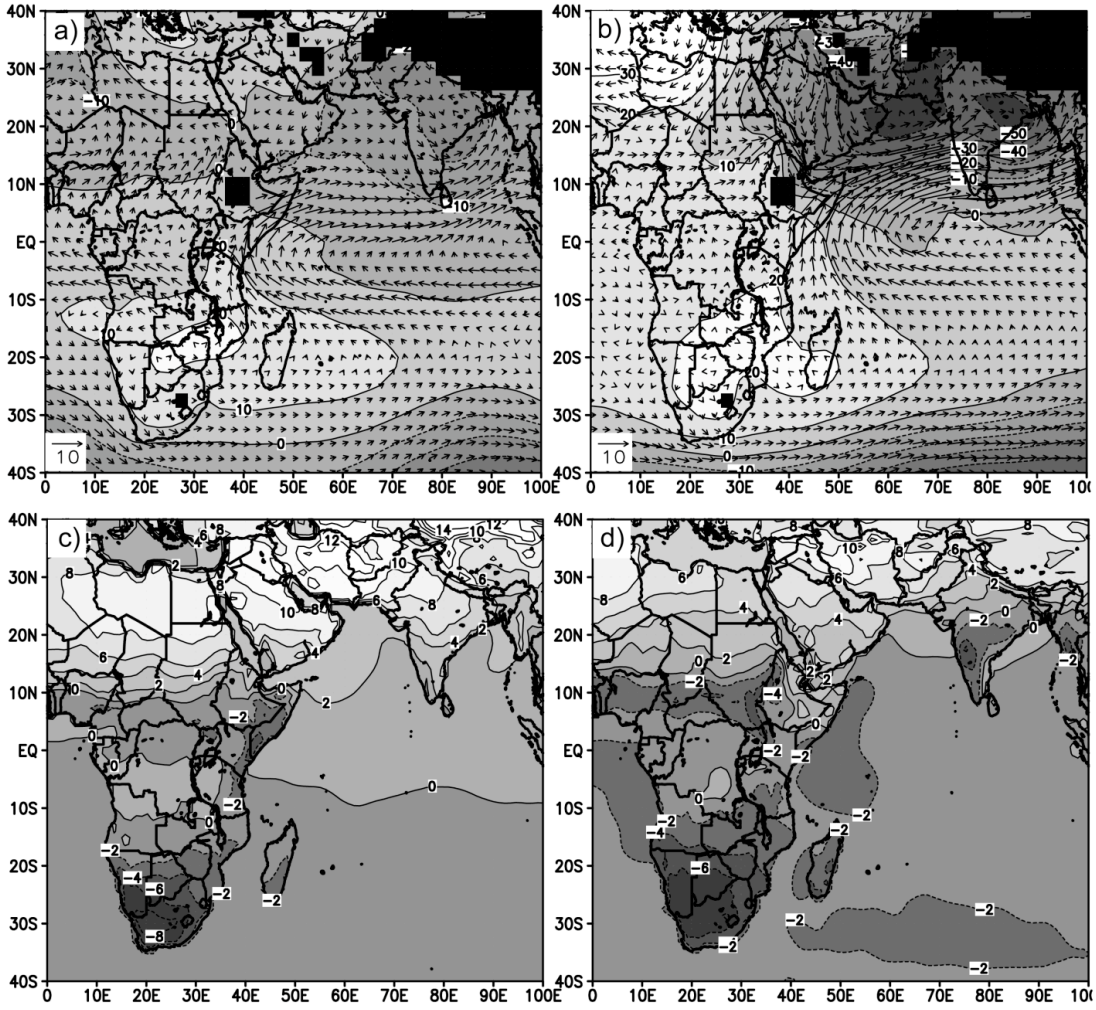

Figure 4.8: Mean seasonal changes in ERA-40 850 hPa geopotential heights (m) and winds (m/s) (a) from March to April/May and (b) from April/May to June and mean seasonal changes in surface temperature (K) based on the ERA-40 reanalysis climatology (1981-2000) (c) from March to April/May and (d) from April/May to June.

While it is not possible in this analysis to determine the causal relationship between changes at the surface and changes in 850 hPa pressure, Figure 4.8 shows that some of the features noted in Figure 4.7 are associated spatially and temporally with seasonal changes in surface temperature. Height increases centered over southern Africa and Madagascar, associated with the change in position of the Mascarene High,

happen concurrently with significant cooling (up to 8 K) of the land surface over this region (Figure 4.8c). In the northern hemisphere, drops in geopotential height over India and central Asia are generally associated with steadily rising surface temperatures over the Iranian and Tibetan Plateaus. Surface temperatures over these plateau regions increase by as much as 12 K between March and April/May (Figure 4.8c). Geopotential heights over Indian plunge further between April/May and June (Figure 4.8d) as diabatic heating from the summer monsoon rainfall accelerates the transition.

Some surface cooling along the East African coastline is observed between March and April/May (Figure 4.8c) and additional cooling is observed along the coast of Somalia between April/May and June (Fig 4.8d) due to coastal upwelling. This cooling along the coast is positioned nearby the coastal ridge which develops in close association with the NSJ. However, this cooling may not be of a large enough scale to be directly associated with the development of the ridge.

4.5 Timing of the Nascent Jet Formation

Since the nascent jet may be linked with rainfall over southern Ethiopia [*Riddle and Cook*, 2008], understanding the timing of the jet onset could be important for rainfall prediction. In this section, we document interannual variability in the jet formation, and suggest a mechanism that may influence the jet formation process.

The jet onset will be characterized using time series plots of 850 hPa wind direction, averaged over land points in the jet focus region (37.5 E to 52.5 E; 5 S to 5 N) shown in Figure 4.1. In the climatology, this index shifts gradually from easterly to southerly during April (Figure 4.5) and is plotted for six individual years in Figure 4.9. These years were chosen arbitrarily to show a representative range of important characteristics.

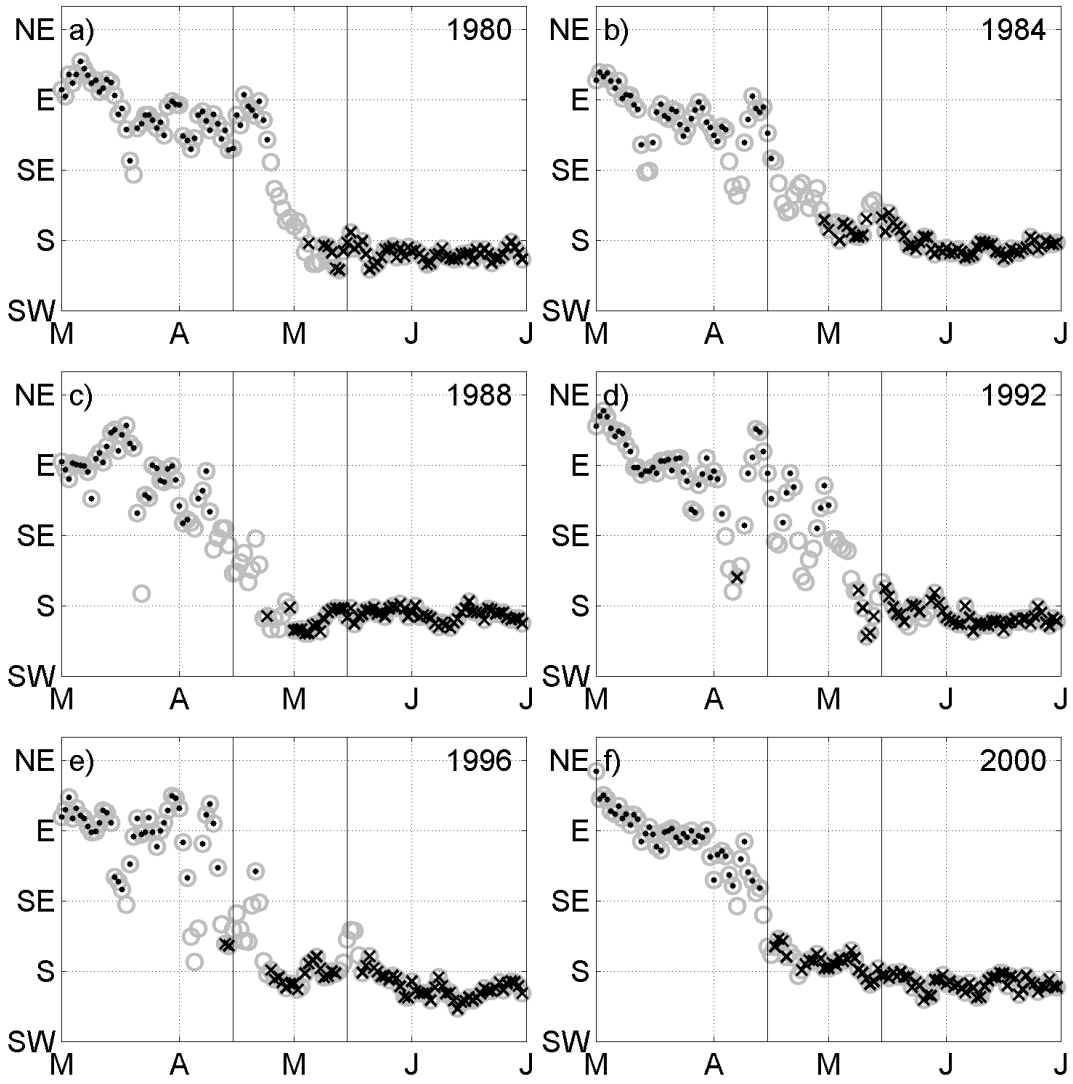

Figure 4.9: Examples of the jet formation in six sample years. Grey circles show wind direction averaged at 850 hPa over land points in the jet focus region (37.5 E to 52.5 E; 5 S to 5 N; shown in Figure 4.1). Black dots show days where the jet is absent or weak. Black x's show days with a strong southrly jet. Grey vertical lines show the time period over which the composite was formed.

Figure 4.9 shows that the character of the jet formation can be different from one year to the next. In some years (e.g., 1980 and 2000), a clear jet onset can be easily identified, while in other years (e.g., 1992 and 1996) winds flip back and forth several times between easterly and southerly before a stable jet is established. In

general, variability in the wind direction at time scales ranging from a few days to a few weeks is much stronger during April/May than in March or June.

The timing of the jet formation also shows significant interannual variability, with the jet formation occurring several weeks earlier in 2000 than in 1980, for example. Because the jet formation within an individual year can be intermittent, identifying the jet onset date is not necessarily straight forward. A jet "stabilization" date - when the wind direction stabilizes in a southerly orientation – is more readily indentified and will be used here to quantify interannual variability. Jet stabilization dates are subjectively chosen for 23 years (1979-2001). Over the 23 year period, the jet stabilization date ranges from 15 April in 2000 to 22 May in 1987 with an averages stabilization date of 03 May and a standard deviation of nine days.

The intermittent and/or abrupt character of the jet formation in most years suggests that gradual seasonal changes in heating may be modulated by variability on shorter timescales. To examine this variability, we created composites of days when the jet was present and strong, and days where the jet was absent or weak. For this categorization, the jet was defined as "strong" when the wind direction showed a bearing south of SSE, and the strength of meridional wind was greater than 5 m/s. The jet was defined as "weak" when the wind direction showed a bearing east of SE and meridional winds were weaker than 2.5 m/s. In Figure 4.9, days when the jet is "weak" are marked by black dots, whereas days when the jet is "strong" are indicated with black x's.

Using these criteria, 99.7% of the 690 days in June were classified as a "strong" jet and no days are classified as "weak". In March, 95% of days are classified as "weak" and no days are classified as "strong". During the period of the nascent jet (15 April – 15 May), 18% of days are classified as "weak" and 32% of days are classified as "strong", with 50% in between.

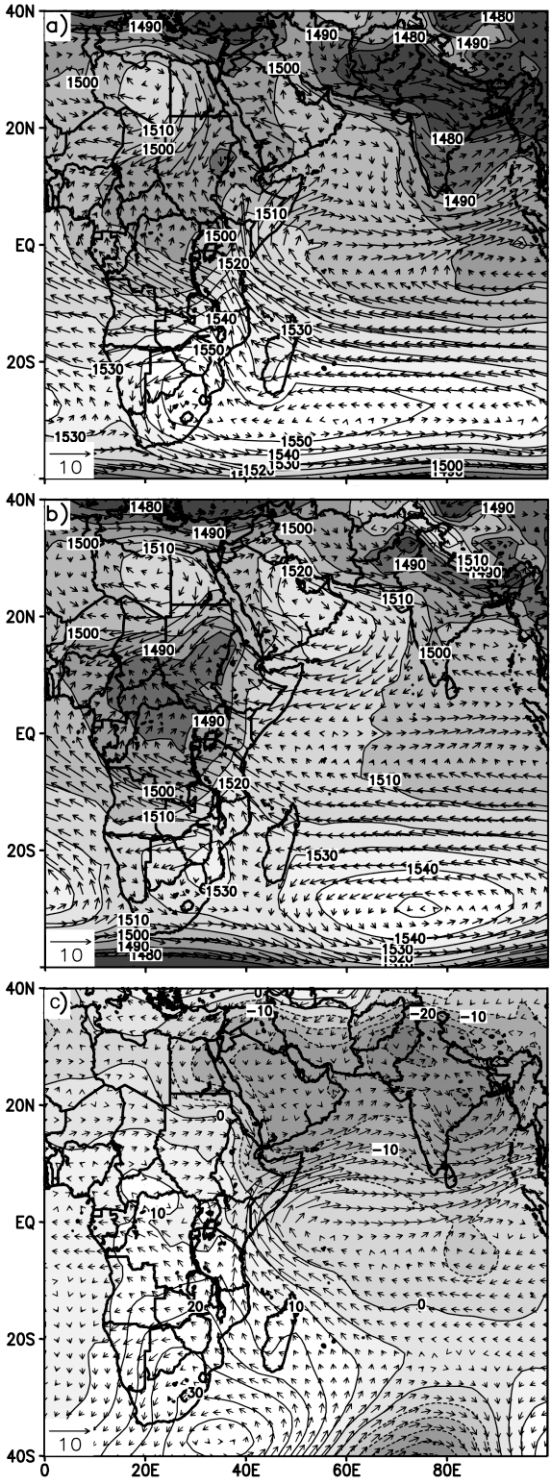

Figure 4.10: 850 hPa geopotential heights and winds averaged over days between 15 April to 15 May with (a) strong jet, (b) weak jet and (c) strong minus weak jet. The method for selecting days with the strong and weak jets is described in section 5.

Figure 4.10 shows composites of the wind and height fields for 226 "strong" jet days and 129 "weak" jet days falling during the nascent jet period (15 April – 15 May) and the anomaly field ("strong" minus "weak"). Since the seasonal cycle was not removed in these plots, some of the anomalies in Figure 4.10c are manifestations of the seasonal cycle, since more "strong" jet days occur later in the season, while more "weak" jet days occur earlier in the season. Indeed, Figure 4.10c shows some very similar patterns to Figures 4.8a and 4.8b which show seasonal cycle anomalies.

However, even without explicitly isolating synoptic variability from the seasonal cycle, the influence of southern hemisphere weather systems can be identified. A strong wave pattern is present at 40° S in the anomaly fields between the strong and weak jets (Figure 4.10c), despite being absent in the seasonal anomalies (Figure 4.8). Geopotential heights are raised south of the African continent (near 35 E) while they are lowered near 75 E. This wave pattern appears even more strongly in the NCEP reanalysis, though the ridge/trough pattern is centered approximately 5 degrees further west. Similar patterns are also robust when 10-year subsets of the 23 years are used for the composites.

These results suggest that southern hemisphere weather systems may play an important role in modulating the seasonal evolution of the NSJ in April and May. Previous studies have shown a link between synoptic disturbances in the southern hemisphere in June-September, and the strength and structure of the cross-equatorial SJ. During these austral winter months, mid-latitude disturbances have been observed to cause surges through the Mozambique Channel, increasing the strength of cross-equatorial flow a few days later [*Findlater*, 1969; *Hart*, 1978; *Cadet and Desbois*, 1981; Rao and Haney, 1982; *Van de Boogaard and Rao*, 1984]. Further work is needed to determine if surges through the Mozambique Channel in April and May also precede the nascent jet formation. If so, this result may have implications for short-

term prediction of the NSJ formation and of the associated changes in moisture transport.

4.6. Simulations of the NSJ Diurnal Cycle

While several studies have previously documented the diurnal cycle of the summertime SJ, none have examined the diurnal cycle of the nascent SJ. The diurnal cycle of the nascent jet is of interest, again because of its potential connection to rainfall. For example, if the jet is transporting moisture into southern Ethiopia, one might expect that the diurnal of the jet might be similar to that of Southern Ethiopian rainfall. Based on Tropical Rainfall Measurement Mission (TRMM) satellite rainfall estimates from 1998-2008 [*Huffman et al.*, 2007], the April/May diurnal cycle of rainfall over southern Ethiopia has two peaks. The first peak occurs between three and six in the morning local time and the second smaller peak is between three and six in the afternoon. In this section, we use regional climate model simulations to examine the diurnal cycle of the NSJ. Model validation is provided first, followed by a characterization of the nascent jet's diurnal cycle and comparison to the TRMM rainfall cycle.

4.6.1 Model Validation

Figure 4.11 compares 850hPa winds from the ERA-40 reanalysis (shown here on a T106 grid) with the WRF model simulation during the pre-jet, nascent jet and full jet stages. While the model captures the basic aspects of the jet development, the jet forms earlier in the model simulation than in the reanlayses. Because of this difference in timing, the dates for each stage of the jet are modified in the regional model. Stage 1 (pre-jet) takes place between 23 February and 25 March. Stage 2

(nascent jet) takes place between 26 March and 25 April. Stage 3 (full jet) takes place between 04 June and 03 July.

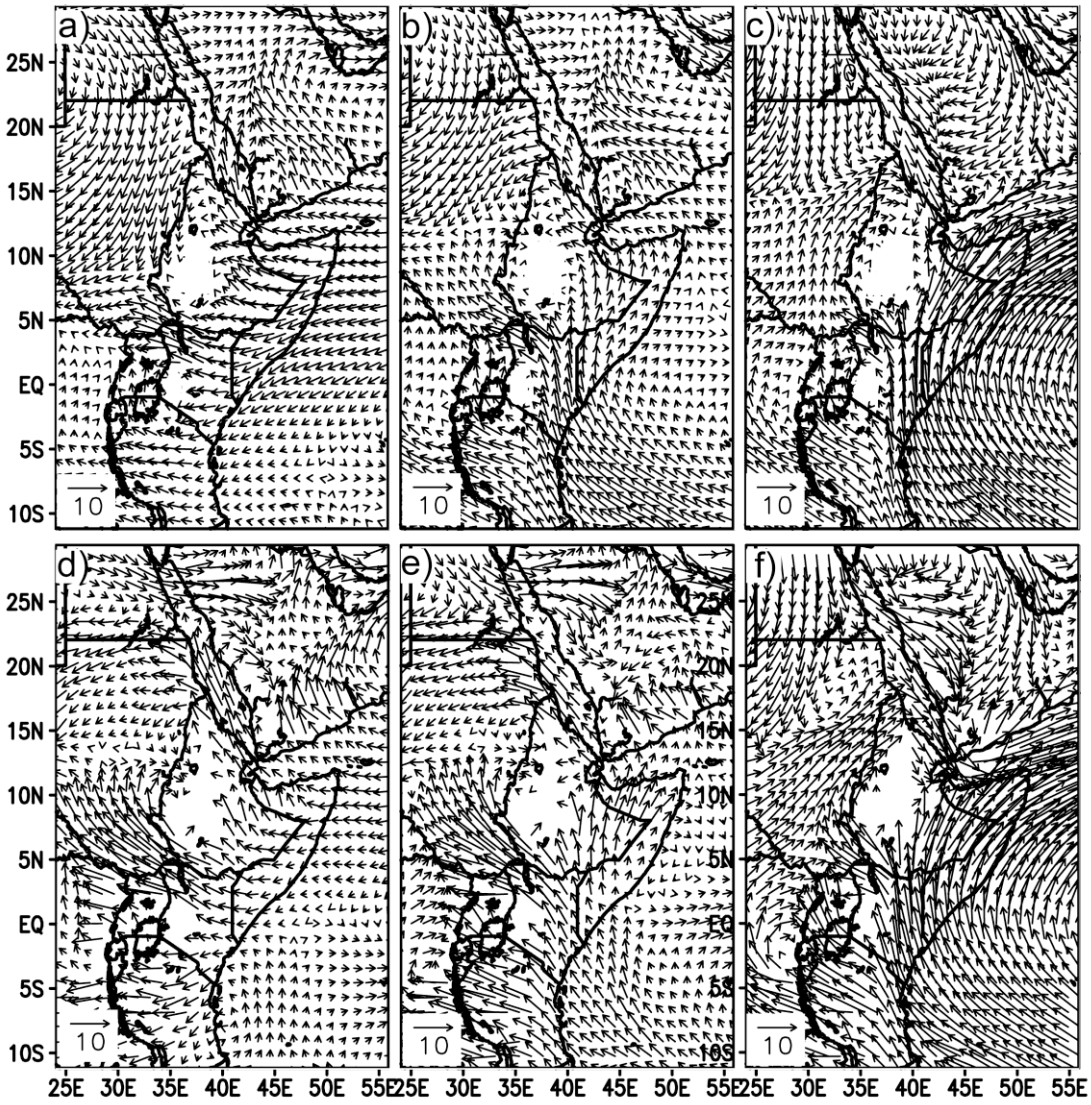

Figure 4.11: 850 hPa winds from (a-c) the ERA-40 reanalysis and (d-f) the WRF simulation during the three stages of the jet formation: pre-jet (left), nascent jet (middle) and full jet (right).

The most striking difference between the nascent jet in the WRF simulation and in the reanalysis is the relative strength of the Turkana Jet in the WRF simulation,

particularly in the pre-jet and nascent jet stages. The Turkana Jet, which passes through the Turkana Channel between the Ethiopian and the East African highlands [*Kinuthia and Asnani*, 1982], is almost twice as strong as the cross-equatorial NSJ in the WRF simulation, particularly in the pre-jet and nascent jet stages. In contrast, these jets are of comparable speed in the ERA40 reanalysis. Since previous work analyzing the Turkana Jet [e.g., *Kinuthia and Asnani*, 1982; *Kinuthia*, 1995] has focused on the winter and summer seasons, it is difficult to know which of these two pictures is more accurate.

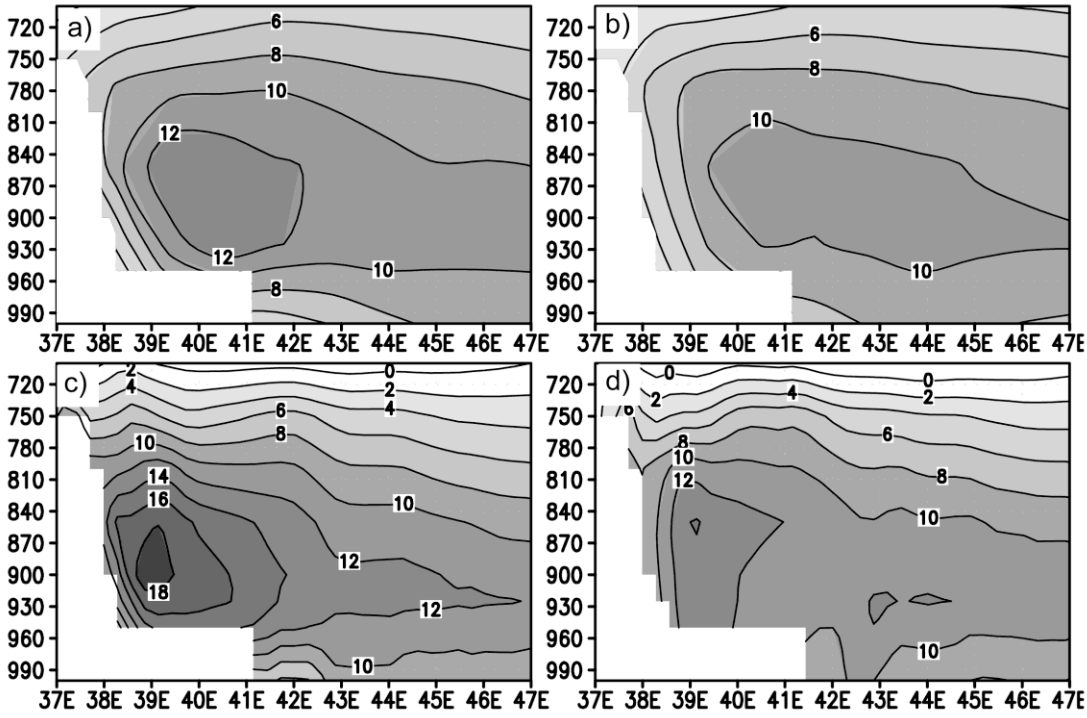

Figure 4.12. ERA-40 reanalysis winds across the equator during (a) nighttime and (b) daytime, and WRF simulation of winds across the equator during (c) nighttime and (d) daytime.

Cross-sections showing the daytime and nighttime structures of the fully formed SJ were presented by *Hart et al.* [1978] based on aircraft transects flown

during the MONSOON77 aircraft campaign. These plots (Figures 8 and 9 in *Hart et al*. [1978]) show day (night) core wind speeds of 12 m/s (17 m/s). Figure 4.12 shows similar cross-sections based on WRF regional model simulation and the ERA-40 reanalysis. The diurnal variability is much larger in the model than in the reanalysis, with daytime winds approximately 15% (30%) smaller than nighttime winds in the reanalysis (model). The larger diurnal cycle simulated by the model agrees better with observations. In addition, the aircraft transects showed that the jet had two separate cores during the daytime, located at approximately 40 E and 44 E. This double core structure is also simulated in the model. Radiosonde data from 1979-2001 over Garissa, Kenya (0.5 S, 39.6 E) also show a larger diurnal cycle than is present in the ERA-40 reanalysis. Nighttime average core wind speeds are 15 m/s compared with 10 m/s during the day. The nighttime peak in the radiosonde data is located at 900 hPa, similar to its location in the model.

We conclude that, while the timing of the jet development is not captured exactly in the model, the model is better than the reanalysis at capturing the diurnal cycle of the jet, when compared with radiosonde and aircraft measurements. This is despite the fact that 1) the radiosonde measurements have been assimilated into the reanalysis and 2) the diurnal cycle has been removed from the model lateral boundary conditions.

4.6.2 Diurnal Cycle of the Nascent Jet

Figure 4.13 shows cross-sections of flow crossing the equator at eight different times of the day, averaged over the nascent jet period (26 March – 25 April in the model). Like the fully established jet, the modeled nascent jet exhibits a diurnal cycle. Winds are maximum between 21:00 UTC and 03:00 UTC which is approximately equivalent to 00:00 to 06:00 local time. During these early morning

hours, core wind speeds are approximately 10 m/s and are located over land very near the surface.

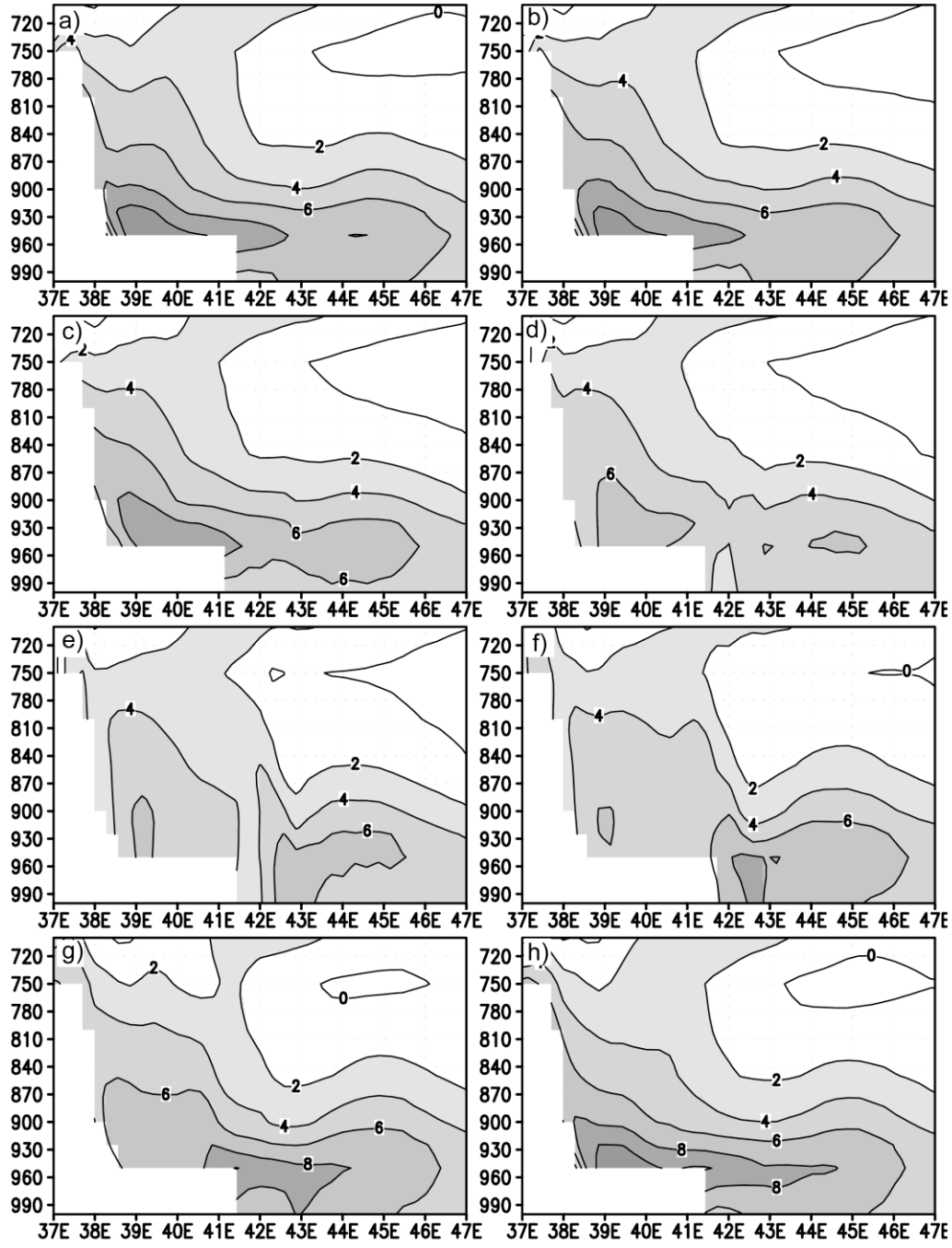

Figure 4.13: Cross-sections showing the diurnal cycle of meridional equatorial winds in the nascent SJ during the spring season based on the WRF simulation at (a) 00Z, (b) 03Z, (c) 06Z, (d) 09Z, (e) 12Z, (f) 15Z, (g) 18Z, (h) 21Z.

Wind speeds weaken over land throughout the day, reaching a minimum of 6 m/s at 15:00 UTC (6 pm local time). At the same time, a second core develops just offshore, strengthening between 09:00 UTC and 18:00 UTC (12 pm and 9 pm local time) and reaching a maximum of 8 m/s in the evening. The core of the jet then moves back onshore after dark. The offshore portion of the jet was not captured in the reanalysis, but resembles the second offshore core noticed in aircraft explorations of the summertime SJ [*Hart et al.*, 1978].

The timing of the maximum jet wind speeds corresponds roughly with the early morning (3:00 – 6:00 AM) peak in satellite observed rainfall over southern Ethiopia. This similarity in the timing of these peaks resembles observations over the central U.S., where a connection is observed between nighttime moisture transport via the Great Plains Low-level Jet (GPLLJ) and a corresponding nighttime peak in rainfall over the Central United States [*Higgins et al.,* 1997]. Since locally-driven convective rainfall is not typically strongest during these early morning hours, this concurrent timing provides one additional piece of evidence linking moisture transport via the nascent jet to rainfall over southern Ethiopia. The afternoon rainfall peak is more likely driven by local convection.

4.7 Discussion

In the previous sections, we have described the seasonal, synoptic and diurnal variability of the nascent jet and suggested that the timing of the jet formation may be connected to interactions with southern hemisphere weather systems. This result may be useful for short term prediction of the jet development. In addition, it would be useful to be able to isolate the underlying seasonal forcing mechanisms that cause the climatological jet evolution. For instance, what underlying seasonal heating changes are required before a synoptic disturbance affects equatorial wind direction?

While we cannot provide a conclusive answer to this question, a few possibilities are worth discussing. The momentum budget analysis suggested that the climatological changes in wind speed are closely linked to local pressure gradient changes. These changes, in turn, are closely associated with the development of a ridge which forms along the coast of East Africa in April/May and persists throughout the summer. However, it is not clear from the present analysis what causes the ridge that forms along the East African coastline.

One possibility is that it is primarily driven by enhanced local surface cooling in the vicinity of the coastline as was shown in Figure 4.8. However, this cooling may not be of a large enough scale to cause the ridge to form. Another hypothesis is that the ridge is the mutually adjusted response to the interaction between the flow and the physical topographic barrier represented by the coastal topography. Simple fluid dynamic models show similarly shaped height contours for a stratified flow impinging on a wall or a ledge [e.g., *Anderson*, 1976; *Paegle and Geisler*, 1986]. If this is true, larger regional-scale (rather than local-scale) changes in heating are likely to be the underlying forcing for the seasonal development of the NSJ.

Many early studies used simplified 1-layer models to examine the low-level dynamics of the jet. In these early models, diabatic heating and cooling were incorporated in the model as prescribed sources or sinks in the continuity equation, imposing divergent and convergent regions in the steady-state flow. In these early models, a zonally elongated mass source was generally prescribed near 15-20 S over southern Indian Ocean while a similarly elongated sink was prescribed near 15-20 N to represent uplift from the Indian summer monsoon. In these models, the sources and sinks were the ultimate drivers of the flow across the equator.

In a multi-layer atmosphere such as described in the reanalysis, regions of low-level convergence and divergence can be identified by calculating the velocity

potential. Because it identifies regions of low-level convergence and divergence, the velocity potential is somewhat analogous to regions of prescribed heating (mass sinks) and cooling (mass sources) in simple models of the jet. Figure 4.14 shows the velocity potential for the three stages shown in Figure 4.7. During June (Figure 4.14c) the velocity potential is quite similar to the sources and sinks prescribed in the simple models of the SJ. Zonally elongated regions of convergence and divergence can be observed at 15-20° north and south of the equator respectively. This agreement gives some confidence that the velocity potential is a reasonable analogy to the source and sink terms prescribed in the simple models describing the jet.

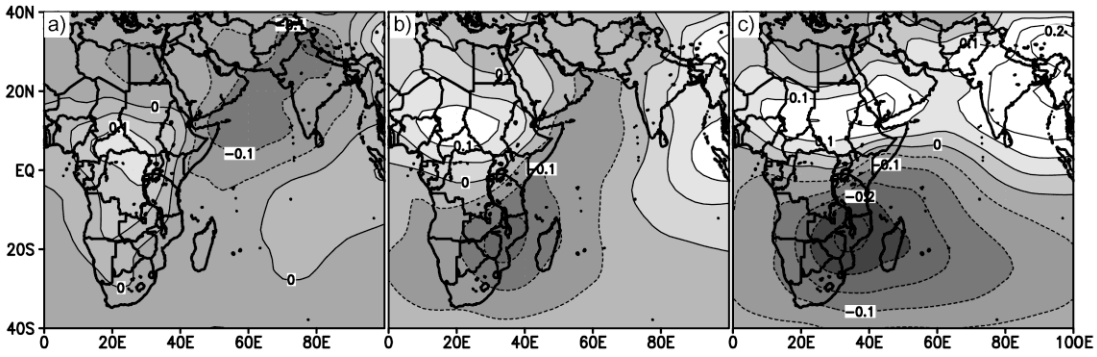

Figure 4.14 Velocity potential at 850 hPa for (a) March, (b) April/May and (c) June based on the ERA-40 reanalsysis.

Applying this analogy to the period of the nascent jet (April/May), we can see some distinct contrasts between the nascent jet, and periods before and after. In March (pre-jet), convergence is centered over Africa and divergence is centered over the Arabian Sea and western Indian Ocean, corresponding to a zonal source/sink dipole between the African continent and Indian Ocean. In contrast, after the nascent jet forms (April/May), the source/sink dipole is oriented in the meridional direction across the equator over the African continent. Unlike in June, regions of convergence

over Africa and southeast Asia, are separated from each other by a region of convergence over the Indian Ocean and Arabian Sea.

Using the analogy with simple one-layer models, this picture suggests that large-scale heating contrasts between the northern and southern African continent may be responsible for the development and maintenance of the nascent SJ, while an eastward extension of this dipole pattern across the Indian Ocean basin is associated with the development of the full SJ. Model simulations designed to test the sensitivity of the jet to different prescribed heating distributions could be used to examine this hypothesis.

4.8 Summary and Conclusions

The nascent Somali Jet, which crosses the equator several months before the full onset of the SJ, is a potentially important source for moisture transport into the Greater Horn of Africa [*Riddle and Cook,* 2008]. While much attention has been given to the fully-formed SJ, very little has focused on the nascent jet. This study is the first to provide detailed documentation of the diurnal, seasonal and synoptic variability of the nascent SJ, and to suggest onset mechanisms which may be useful for predicting the timing of the jet formation.

The seasonal cycle of the NSJ is examined using the ERA-40 and NCEP-2 reanalyses. The nascent jet is shown to form over land in April and spread westward across the Indian Ocean in May. Its formation in April consists of a low-level shift in equatorial wind direction from easterly to southerly in conjunction with a nearly parallel shift in the direction of the local pressure gradient. A momentum budget analysis shows that an approximate balance between friction and the pressure gradient force leads to this close relationship over the land surface, whereas a strong centrifugal force complicates the relationship over the ocean.

When put in a regional context, changes in the local pressure gradient are shown to be related to increasing heights over southern Africa, a shift in the position of the Mascarene high, and the development of a ridge along the coast of East Africa. These increased heights are associated spatially and temporally with surface temperature drops over southern Africa and along the East African coastline, though a causal relationship between the two has not been established.

Since the nascent jet may be tied to rainfall over southern Ethiopia [*Riddle and Cook,* 2008], understanding the timing of the jet formation could potentially be important for rainfall prediction. The reanalyses show that the character and timing of the jet onset vary from year to year. In some years a clear onset of the jet is apparent, while in other years winds are highly variable, flipping back and forth several times before a southerly cross-equatorial jet is clearly established. Dates associated with a final stabilization of the jet range from 15 April in 2000 to 22 May in 1987.

This paper takes a preliminary step at understanding the timing of the jet formation. Composites of days with "strong" and "weak" jets show that the jet formation is likely affected both by low frequency seasonal changes as well as by higher frequency synoptic forcings from southern hemisphere weather systems. This connection with southern hemisphere waves is reminiscent of variability in the fully-formed SJ associated with surges through the Mozambique Channel several days earlier. Further work is needed to determine if a similar mechanism is at work during the nascent jet formation and to better untangle the interaction between synoptic and seasonal forcings.

This paper is the first to examine the diurnal cycle of the nascent jet. A regional climate model simulation is able to capture the diurnal cycle of the jet better than either the NCEP-2 or ERA-40 reanalyses, as determined by comparisons to radiosonde and aircraft measurements. The NSJ is found to have a diurnal cycle, with

daytime winds approximately 30% smaller than nighttime winds, with winds strongest between midnight and 6am local time, and weakest in the afternoon. The timing of this maximum corresponds roughly with a rainfall maximum over southern Ethiopia as measured by the TRMM satellite.

This paper has provided a detailed description of the nascent Somali Jet, previously missing from the literature, and provided one new piece of evidence suggesting a connection between the nascent jet and southern Ethiopian rainfall. Results from this paper also open the interesting question of whether short-term prediction of the nascent jet formation may be possible. Future work will focus on this question of predictability, both of the nascent jet formation and of associated shifts in rainfall.

4.9 Acknowledgements.

This research is to be submitted as a paper Journal of Climate, coauthored by Dr. Kerry H. Cook. This research was supported by the NASA Earth Systems Science Fellowship program, NSF grant ATM-0415481 and the American Association for University Women (AAUW) American Dissertation Fellowship. Acknowledgment is made to the National Center for Atmospheric Research, which is sponsored by the National Science Foundation, for the computing time used in this research. ERA-40 reanalysis data and radiosonde reports were obtained from the Research Data Archive (http://dss.ucar.edu/) datasets number ds366.0, ds127.0, ds127.1 and ds118.0. The RDA is provided by the Computational and Information Systems Laboratory at the National Center for Atmospheric Research that is supported by the National Science Foundation. We extend our gratitude to Edward Vizy for his valuable assistance with

the model simulations and analysis and to Daniel Wilks and Natalie Mahowald for editorial comments.

REFERENCES

Anderson, D.L.T. 1976, The low-level jet as a western boundary current, *Monthly Weather Review,* 104 (7), 907-921.

Annamalai, H., J.M. Slingo, K.R. Sperber, 1999, The mean evolution and variability of the Asian summer monsoon: Comparison of ECMWF and NCEP-NCAR reanalyses, *Monthly Weather Review,* 126(6), 1157-1186.

Ardanuy, P., 1979, Observed diurnal oscillation of the Somali jet, *Monthly Weather Review,* 107 (12). 1694-1700.

Bannon, P.R., 1979, On the dynamics of the East African Jet. I: Simulation of mean conditions for July, *Journal of the Atmospheric Sciences,* 2139-215.

Bannon, P.R., 1979, On the dynamics of the East African Jet 2. Jet transients, *Journal of the Atmospheric Sciences,* 36 (11), 2153-2168.

Bannon, P.R., 1982, On the dynamics if the East African Jet 3. Arabian sea branch, *Journal of the Atmospheric Sciences,* 39 (10), 2267-2278.

Boos, W. R., and K. A. Emmanuel, 2009, Annual intensification of the Somali Jet in a quasi-equilibrium framework: Observational composites, *Q. J. R. Meteorol. Soc*. **135**: 319-335.

Cadet, D., and M. Desbois, 1981: A case study of a fluctuation of the Somali jet during the Indian Summer Monsoon. Mon. Wea. Rev., 109, 182-187.

Chakraborty, A., Nanjundia, R. S., Srinivasan J., Impact of African orography and the Indian summer monsoon over the low-level Somali Jet, *Int. J. Climatol.* **29:** 983-992.

Dudhia, J., 1989, Numerical study of convection observed during the winter monsoon experiment using a mesoscale two-dimensional model. *J. Atmos. Sci.*, 46, 3077-3107.

Fasullo, J. and P.J. Webster, A hydrological definition of the Indian Monsoon Onset and Withdrawal, 2003, J. Clim., 16: 3200-3211.

Findlater, 1966, Cross-equatorial jet streams at low level over Kenya, *Meteorological Magazine, London,* 95, 353-364.

Findlater, 1967, Some further evidence of cross-equatorial jet streams at low level over Kenya, *Meteorological Magazine, London,* 96, 216-219.

Findlater, J., 1969: A major low-level air current near the Indian Ocean during the northern summer. *Quart. J. Roy. Meteor. Soc.*, **95**, 362-380.

Findlater, J., 1969, Interhemispheric transport of air in the lower troposphere over the western Indian Ocean, *Quart. J. Roy. Meteor. Soc.*, **95**, 400-404.

Findlater, J., 1971, Mean monthly airflow at low levels over the western Indian Ocean, *Geophysical Memoirs,* 115, 1-53.

Findlater, J, 1977, Observational aspects of the low-level cross-equatorial jet stream of the western Indain ocean, *Pure and Applied Geophysics,* 115(5-6) 1251-1262.

Hart, J.E. 1977, On the theory of the East African Low-level jet stream, *Pure and Applied Geophysics,* 115, 1263-1282.

Hart, JE, Rao GV, H Vandeboogaard, JA Young, J Findlater, 1978, Aerial observations of the east African low-level jet stream, *Monthly Weather Review,* 106(12), 1714-1724.

Higgins, R. W., Y. Yao, E. S., Yarosh, J. E. Janowiak and K. C. Mo, 1997, Influence of the Great Plains low-level jet on summertime precipitation and moisture transport over the central United States, *J. Clim*, 10: 481-507.

Hoskins, B.J., and M.J. Rodwell, 1995, A mode of the Asian Summer Monsoon, 1. The global-scale, *Journal of the Atmospheric Sciences,* 52(9), 1341-1356.

Huffman, G.J., R.F. Adler, D.T. Bolvin, G. Gu, E.J. Nelkin, K.P. Bowman, Y. Hong, E.F. Stocker, D.B. Wolff, 2007: The TRMM Multi-satellite Precipitation Analysis: Quasi-Global, Multi-Year, Combined-Sensor Precipitation Estimates at Fine Scale. J. Hydrometeor.

Janjic, Z. I., 2002: Nonsingular Implementation of the Mellor-Yamada Level 2.5 Scheme in the NCEP Meso model. NCEP Office Note No. 437, 61 pp.

Joseph, PV, and S. Sijikumar, 2004, Intraseasonal variability of the low-level jet stream of the Asian summer monsoon, *Journal of the Climate,* 17(7), 1449-1458.

Kain, J. S. (2004), The Kain-Fritsch Convective Parameterization: An update, *J. Appl. Meteorol., 43*, 170-181.

Kanamitsu, M., W. Ebisuzaki, J. Woollen, S. K. Yang, J. J. Hnilo, M. Fiorino, and G. L. Potter (2002), NCEP-DOE AMIP-II Reanalysis (R-2), *Bull. Amer. Meteorol. Soc.*, *83*, 1631-1643.

Kinuthia, J.H., and G. C. Asnani, 1982, A newly found jet in north Kenya (Turkana Channel), Mon. Weather Rev., 110 (11), 1722-1728.

Kinuthia J. H., 1992: Horizontal and vertical structure of the Lake Turkana jet. *J. Appl. Meteor.*, **31**, 1248–1274

Krishnamurti, T.N., V. Wong, H.L. Pan, R. Pasch, J. Moliari, P. Ardanuy, 1983, A three dimensional planetary boundary layer model of for the Somali Jet, *Journal of the Atmospheric Sciences,* 40(4), 894-908.

Krishnamurti T.N., and V. Wong, 1979, Planetary boundary layer model for the Somali Jet, *Journal of the Atmospheric Sciences,* 36(10), 1895-1907.

Krishnamurti, T. N., and H. N. Bhalme, 1976, Oscillations of a monsoon system. Part I. Observational aspects, *J. Atmos. Sci.*, **33**, 1937-1954,

Krishnamurti, T.N., Moliari J. and H.L. Pan, 1976, Numerical simulation of the Somali Jet, *Journal of the Atmospheric Sciences,* 33(12), 2350-2362.

Lin, Y.-L., R. D. Farley, and H. D. Orville, 1983, Bulk parameterization of the snow field in a cloud model. *J. Climate Appl. Meteor*., 22, 1065-1092.

Mellor, G.L. and T. Yamada, 1982, Development of a turbulence closure model for geophysical fluid problems. *Rev. Geophys. Space Phys.,* **20**, 851-875.

Mlawer, E. J., S. J. Taubman, P. D. Brown, M. J. Iacono, and S. A. Clough, 1997, Radiative transfer for inhomogeneous atmosphere: RRTM, a validated correlated-k model for the long-wave. *J. Geophys. Res.,* 102(D14), 16663-16682.

Paegle J. and J.E. Geisler, 1986, The effect of East African topography on flow driven by zonally symmetric forcing, *Journal of the Atmospheric Sciences,* 43(17), 1862-1872.

Patricola, C. M., and K. H. Cook (2007), Dynamics of the West African monsoon under mid-Holocene precessional forcing: Regional climate model simulations, *J. Clim., 20*, 694-716.

Patricola, C. M., and K. H. Cook (2010), Northern African climate at the end of the 21st century: Integrated application of regional and global climate models. *Clim. Dyn.,* DOI 10.1007/s00382-009-0623-7.

Raghavan, K, Sikka, DR, Gluar, SV, 1975, Influence of cross-equatorial flow over Kenya on rainfall over western India, *Quarterly gournal of the Royal Meteorological Society,*

Rao, G. V., and J. L. Haney, 1982: Kinematic and thermal structure of two surges of flow in the northern Mozambique channel area. *Quart. J. Roy. Meteor. Soc.,* **108,** 957–974..

Reverdin G. and G. Sommeria, 1983, The dynamical structure of the planetary boundary layer over the Ariabian Sea as deduced from constant-level balloon trajectories, *J. Atmos. Sci*,. **40**, 1435-1452.

Riddle E.E and K.H. Cook (2008), Abrupt transitions in rainfall over the Greater Horn of Africa: Observations and Regional Climate simulations, *J. Geophys. Res.,* 113 (D15), D15109.

Rodwell, M.J., and B.J. Hoskins, 1995, A model of the Asian summer monsoon 2. Cross-equatorial flow and PV behavior, *Journal of the Atmospheric Sciences,* 52(9), 1341-1356.

Rodwell, M.J., 1997, Breaks in the Asian monsoon: The influence of Southern Hemsiphere weather systems, *Journal of the Atmospheric Sciences,* 54(22), 2597-2611.

Rubenstein, DM, 1981, The daytime evolution of the East African jet, *Journal of the Atmospheric Sciences,* **38**(1), 114-128.

Sepulchre, P., G. Ramstein, F. Fluteau, M. Schuster, J.-J. Tiercelin, and M. Brunet, 2006, Tectonic Uplift and Eastern Africa Aridification, *Science*, 313, 1419-1423.

Shamrock, W.C., J.B. Klemp, J. Dudhia, D.O. Gill, D. M. Barker, W. Want and J.G. Powers, 2005, A dscription of the Advanced Research WRF Version 2, NCAR Technical Note No. 468 (TN-468+STR) 88 pp.

Slingo, J., H. Spencer, B. Hoskins, P. Berrisford, E. Black, 2005, The meteorology of the Western Indian Ocean, and the influence of the east African highlands, *Philosophical Transactions of the Royal Society of London, Series A*. 363, 25-42.

Smirnova, T.G., J.M. Brown, S. G. Benjamin, and D. Kim, 2000, Parameterization of cold-season processes in the MAPS land-surface scheme, *J. Geophys. Res.*, 104, D3 4077-4086.

Taniguchi, K., and T. Koike, 2006, Comparison of definitions of the Indian summer monsoon onset: representation of rapid transitions of atmospheric conditions, *Geophysical Research Letters,* **33**(2), L02709.

Uppala SM, Kållberg PW, Simmons AJ, Andrae U, Bechtold V da C, Florino M, Gibson JK, Haseler J, Hernandez A, Kelly GA, Li X, Onogi K, Saarinen S, Sokka N, Allan RP, Andersson E, Arpe K, Balmaseda MA, Beljaars ACM, van de Berg L, Bidlot J, Bormann N, Caires S, Chevallier F, Dethof A, Dragosavac M, Fisher M, Fuentes M, Hagemann S, Hólm E, Hoskins BJ, Isaksen L, Janssen PAEM, Jenne R, McNally AP, Mahfouf J-F, Morcrette J-J, Rayner NA, Saunders RW, Simon P, Sterl A, Trenberth KE, Untch A, Vasiljevic D, Viterbo P, Woolen J., 2005. The ERA-40 re-analysis. *Q. J. R. Meteorol. Soc.* **131**: 2961-3012.

Van de Boogaard, H. M. E., and G. V. Rao, 1984, Mesoscale structure of the low-level flow near the equatorial East African coast, *Mon. Weath. Rev.* 112, 91-107.

Vizy, E. K., and K. H. Cook (2002), Development and application of a mesoscale climate model for the tropics: Influence of sea surface temperature anomalies on the West African monsoon, *J. Geophys. Res., 107*(D3), 4023, doi:10.1029/2001JD000686

Wu, MLC, S. Schubert, and N.E. Huang, 2001, the development of the South Asian summer monsoon and the intraseasonal oscillation, *Journal of the Climate,* 12 (7), 2054-2075.

CHAPTER 5

SUMMARY, CONCLUSIONS AND FUTURE DIRECTIONS

5.1 Summary

The populations of countries across eastern Africa, from Tanzania to Ethiopia, depend heavily on rain-fed agriculture. Better rainfall forecasts could help farmers, pastoralists and government agencies in better planning for seasonal anomalies in the quantity and timing of rainfall. This dissertation focuses specifically on the seasonal cycle of rainfall, one important aspect of eastern African rainfall variability. The work offers incremental improvements in our understanding of the northward progression of ITCZ rainfall, with the ultimate goal of laying a better groundwork for forecasts at seasonal and sub-seasonal timescales.

The three central chapters in this study have analyzed the eastern African rainfall cycle using three very different approaches. The first paper (Chapter 2) uses a regional climate model as well as simple plots of observational and reanalysis climatologies to characterize basic climatological features in the north/south progression of rainfall. The second paper (Chapter 3) uses a Principal Component Analysis and a Cluster Analysis to create statistical indices that describe the seasonal cycle. The indices are used to examine variations around the seasonal cycle over thirteen recent years. The third paper (Chapter 4) analyzes the dynamics of the nascent Somali Jet which has been shown in the previous chapters to be connected to the timing of southern Ethiopian rainfall.

5.2 Primary Conclusions

These papers have contributed to our scientific understanding of eastern African rainfall in several ways. The most important advancements coming out of this work are listed in the following pages:

1) Previous studies have noted abrupt latitude transitions in ITCZ rainfall over the Indian Ocean, the western Pacific, South America, and during the onset of the West Africa and East Asian monsoons. This study finds that abrupt transitions or "jumps" also occur over eastern Africa in March, April and May, with the primary northward jump occurring between March 24th and April 17th over the years 1998 to 2010. This rainfall jump was successfully captured using a Regional Climate Model.

2) This study finds that the latitude "jumps" can be concisely captured with time-varying statistical indices. Two indices, calculated using Principal Component Analysis and a Cluster Analysis, are found to be useful for describing inter-annual variability in the timing of rainfall jumps and for examining the dynamics associated with excursions from the seasonal cycle. The indices will hopefully also be useful in developing prediction models for the northward rainfall progression.

3) During April and May, a "nascent" Somali Jet forms along the coast of eastern Africa. While previous studies have focused on the summertime Somali Jet, this southerly jet which forms in April and May is an important feature of boreal springtime climatology. The jet is present in regional climate models, the NCEP and ECMWF reanalysis, and in radiosonde measurements.

4) All three papers provide some evidence connecting the northward rainfall progression and the Somali Jet formation. The first paper (Chapter 2) demonstrates that rainfall jumps are coincident with stages in the formation of the Somali Jet, including the nascent Somali Jet. The second paper (Chapter 3) shows that this connection holds at daily to intra-seasonal timescales, with seasonal progress in the jet formation associated with northward progress in the rainfall cycle. The third paper (Chapter 4) shows that the diurnal cycle of the Somali Jet is similar to that of rainfall over southern Ethiopia. This conclusion contrasts with a previous body of literature which has generally assumed that the Somali Jet in particular, and the southwest monsoon flow in general, do not provide a productive source of moisture over eastern Africa. While true in the boreal summer, this study finds that the conditions are different in April and May, and the "nascent" Somali jet is likely a source of moisture for southern Ethiopia.

5) Evidence is provided in the final paper (Chapter 4) linking the timing of the "nascent" Somali Jet formation to the passage of southern hemisphere weather systems. Further work is needed to conclude whether or not this connection provides any predictive skill for either the jet formation, or transitions in rainfall.

5.3 Future Research Directions

The results presented in this study pose questions and directions which should be explored in future research. Three primary directions are discussed here. The most obvious next step is to use the results to develop a prediction model for rainfall

transitions, starting with lead times of days to weeks. A preliminary analysis of archived 5-day forecasts from ECMWF suggests that the dynamical models have little skill in predicting abrupt rainfall transitions five days in advance. Further work would be needed to verify these results and examine if a statistical model could do better.

A second direction would be to follow up on results from the final paper (Chapter 4) on the nascent Somali Jet (NSJ) with a more in depth modeling study. While the study identified some important features (e.g., southern hemisphere weather systems) that are associated with the nascent jet development, it did not pinpoint which seasonal changes are most responsible for the formation of the NSJ. A follow-up study might use either a shallow water equation model or a modified global model to examine the sensitivity of the nascent jet to various distributions of diabatic heating and topographic configurations.

A final interesting direction would be to examine how a changing climate would affect the seasonal rainfall progression over eastern Africa. All of the work in this current study has focused on characterizing seasonal and intra-seasonal variability in the past 13 years. However, these patterns may have been different in the past and may be different in the future. There is currently debate in the scientific community about whether anthropogenic warming will lead to a wetter or dryer climate over eastern Africa, and the results presented here, including the connection between southern Ethiopian rainfall and the nascent Somali Jet, may offer some insight into that controversy.